Growth of III-V Semiconductor Quantum Dots by Droplet Epitaxy

ハ, ヌル

Growth of III-V Semiconductor Quantum Dots by Droplet Epitaxy

Neul Ha

Graduate School of Engineering

Kyushu University

March 2015

Contents

CHAPTER 1   Introduction

1.1   Development of semiconductor technology

Modern society is highly reliant on the information technologies such as information processing, information storage, and communication. Semiconductor devices are indispensable components that support such technologies. Semiconductor electronic devices, optical devices, and optoelectronic devices have all been commercialized, and we can find these devices everywhere around us.

The first transistor using germanium was developed by J. Bardeen et al. [1] and replaced vacuum tubes. The replacement of vacuum tubes with semiconductor transistors played an important role in the miniaturization and weight reduction of electronic devices. The results were the beginning of the strong development of the semiconductor industry. After that, the change from germanium to silicon and the development of Integrated Circuit (IC) brought great changes to the semiconductor industry [2]. The use of Si-based IC technology has enabled the creation of Central Processing Units (CPUs) and Random-Access Memory/Read-Only Memory (RAM/ROM). Ultra-high integrated microprocessors and memory chips have been applied in various home electrical appliances.
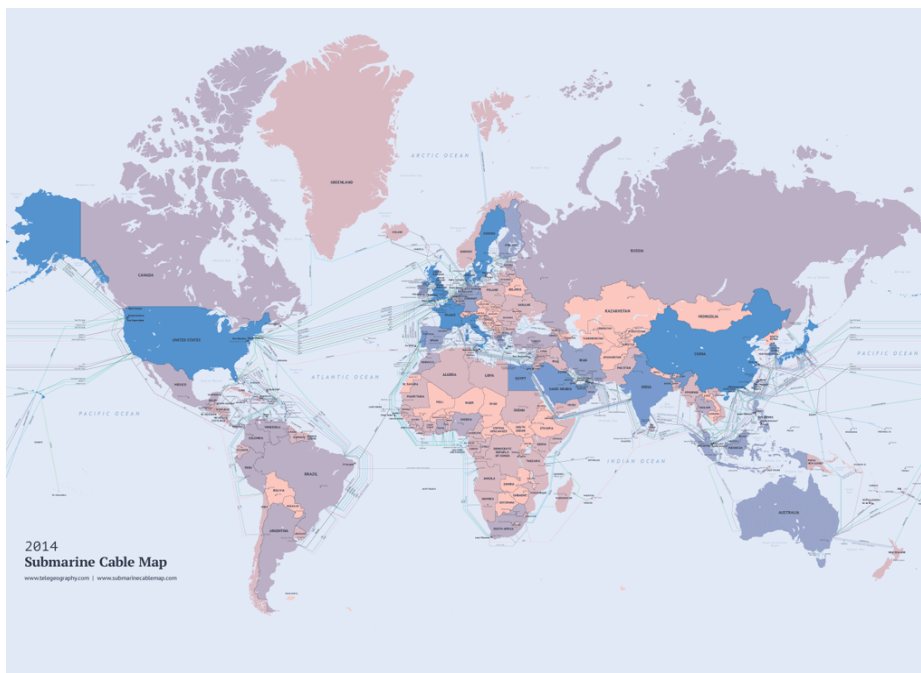

Fig. 1.1   Submarine optical fiber links used around the world.

Since the efficient light emission cannot be expected in silicon or germanium (indirect bandgap materials), compound semiconductors (III-V) have been used for the optical devices. GaAs- and InP-related heterostructures have enabled light emission from visible (yellow) to infrared wavelength region. Depending on the applications, appropriate wavelengths are selected. For the optical recording devices, such as Compact Disks (CDs) and Digital Video Disks (DVDs), yellow-red laser diodes (LDs) are used. For the optical communication, 1.3 or 1.55 μm LDs are used in an optical fiber communication, and $0.8 - 0.9$ μm LDs are used in remote controllers. In modern communication systems, the majority of Internet data is transmitted though the optical fibers because of very high-speed and low-loss transmission over much longer distance in comparison to electric copper wires. As shown Fig. 1.1, submarine optical fibers connect all the continents.

Meanwhile, the development of GaN based heterostructure facilitated to create purple, blue and green LED, which cannot be realized by using GaAs or InP-related materials. The emergence of blue LED has changed the lighting for saving electricity in all over the world. Also, GaN-related materials are now used in Blu-ray disk recorder, high power electric devices, etc.

The development of semiconductor optical devices was accelerated with the invention of LD. The first LD was invented by R. N. Hall et al., in 1962 [3], which were based on a simple GaAs p-n junction. After that, the LD efficiency was drastically improved by an introduction of double heterostructure concept. As a results, LD operating at room temperature was achieved in 1970 [4]. Due to this achievement, Prof. Zh. I. Alferov received Nobel Prize. The use of heterostructure has led to a highly efficient LD, furthermore, it facilitated the development of an advanced concept LD such as quantum well (QW) LD [5]-[7], vertical cavity surface emitting laser (VCSEL) [8], [9], and quantum cascade laser (QCL) [10]. In QW-LD and QCL, owing to the formation of one-dimensionally quantum-confined structures, high performance and/or novel functionalities have been achieved. Note that the one-dimensionally confined two-dimensional systems also highly contributed to electronic devices. By using a high mobility in the modulation-doped two-dimensional systems, quantum Hall effect was discovered. After that, the researches on further low-dimensional structures such as quantum wires (QWRs) and quantum dots (QDs) have been begun.

In 1982, Y. Arakawa and H. Sakaki first proposed the concept of QD structures for implementation in LD in which insensitivity against temperature can be expected [11]. This concept was theoretically confirmed by M. Asada et al [12] in 1986, which showed higher gain and lower threshold current compared to QW and QWR devices. In QD, we can suppress thermal broadening of optical emission due to the sharp density of state (DOS). Thus, we can realize the devices insensitive threshold current on temperature.

In contrast to the attractive concept of the QD-LD, the formation of semiconductor QDs was a challenging issue. In 1985, the self-assembled QDs were experimentally demonstrated by L. Goldstein [13]. They found that three-dimensional structures were naturally formed by Stranski-Krastanow (S-K) mode when InAs were grown on GaAs. After that, many groups have studied the self-assembled formation of QDs not only by the S-K mode but also the other methods such as droplet epitaxy method [14]. In addition,

2

lithographic techniques, top-down approach has also been studied intensively [15]-[17]. Besides, atom-like properties of QDs stimulate great interests in addition to the LD. With reducing QDs size, quantum phenomena related to the three-dimensional quantum confinement have been observed, where a single object can be in two place at once (superposition) [18]-[20] and where two objects in remote locations can be instantaneously connected (entanglement) [21]-[24]. The result suggests that QDs can be use as single photon source for quantum information processing, as well as communication. By using the photon sources, we can possibly realize new concept of communication technology for quantum cryptography, in which perfect security can be guaranteed. For these reasons, QDs have been become one of the most important subject in the study on low-dimensional semiconductor physics and application.

1.2   Low-dimensional semiconductors

The unique properties of low-dimensional semiconductors rely on the carrier quantum confined effect. The effect is illustrated by the energy band diagram in Fig. 1.2(a). The well material is sandwiched by the barrier material. Due to the carrier quantum confinement, the bound states of low dimensional semiconductors appear at higher levels than those of bulk semiconductors in both conduction and valence band. The quantization energies depend on the effective mass, the thickness of the well material, and the barrier height [25]. Figure 1.2(b) shows the density of states (DOS). The DOS of a bulk material is continuous and proportional to $E^{1/2}$. In QWs, carriers are confined in a direction normal to the layer, but free to move in the directions parallel to the layer. Therefore, its DOS exhibits step-like subbands. In QWRs, carriers are confined in two-dimensions, and free to move along only one direction. The DOS is proportional to $E^{-1/2}$. In QDs, carriers are confined in all three-dimensions. Thus, perfectly discrete energy levels can be realized. The energy of confined states can be tuned by the selection of material combination and the size of QDs.

The optical properties of QDs can be characterized by the absorption and emission spectra. If a QD is excited, a hole is produced in the valence band, and an electron is produced in the conduction band. Consequently, an electron-hole pair forms an exciton. Recombination of electron-hole pairs induces photon emission.

Using a QD, we can control the number of excitons one by one. The first and the second excitons fill the lowest energy state (like the s-shell of an atom) and the third exciton fills the second energy state (like the p-shell of an atom) according to Pauli's exclusion principle [26], [27]. Thus, QDs are also called as artificial atoms.

1.3   Application of quantum dots

Semiconductor QDs offer a great potential to realize advanced optoelectronic devices. The major research has focused on the development of light sources. Owing to the discrete DOS (Fig. 1.2(b)), thermal broadening in emission spectra can be suppressed [28], [29]. Thus, we can expect QD lasers [12], [30]-[33] and LED [34]-[36] that indicate low threshold current and high temperature stability. In addition, the emission energy is adjustable by size tuning. We can also realize efficient QD solar cells and detectors. Some of the QD advantages such as temperature-insensitive laser have been already confirmed [12]. The optical properties of QDs depend mostly on the QD morphology; lateral and vertical size, density, and size distribution.
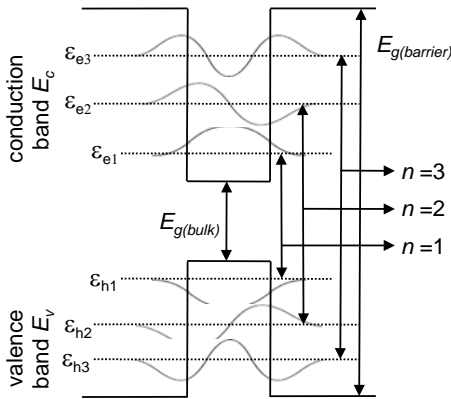
Another attractive application is single [37]-[39], and entangled photon sources [21], [23], [24], [26], [40]-[44], which are key devices for quantum key distribution [45]-[47] and quantum computing [48], [49]. In classic light sources, the photon number state cannot be realized. In QDs, we can realize single or entangled photon emission due to the atom-like electric structure.

Figure 1.3(a) shows the schematic of biexciton cascade in QD. Illumination by an excitaion laser induces two electrons and two holes (biexcitons), which decay by a radiative cascade [26], [50]. One of the electrons recombines with one of the holes with generating the first photon. A remnant electron-hole pair subsequently recombines and generates the second photon. The biexciton and exciton have different energies (Fig 1.4(a)) [51]-[53]. The exciton state of the QD has a lifetime due to radiative decay. Thus, if the lifetime is much longer than the duration of the exciting laser pulse, only one photon can be emitted [39], [54].

Figure 1.3(b) shows the schematic of biexciton cascade in a QD with zero polarization splitting S. The transition has two paths due to spinor nature of excitons [55]. When these two paths are degenerate and energetically indistinguishable, two photons emitted along the cascade become entangled on a polarization basis (Fig. 1.4(b)).

Recently, the emission of entangled photons was demonstrated in QD with zero polarization splitting (or fine structure splitting, FSS) [23], [56]. The FFS is caused by non-ideal properties of QDs such as in-plane asymmetry [50], [57], [58]. Thus, in order to realize entangled photon source, laterally symmetric QDs are required.

(a) Quantum confinement

conduction band E_c

ε_{e3}
ε_{e2}
ε_{e1}

$E_{g(barrier)}$

$E_{g(bulk)}$

$n = 3$
$n = 2$
$n = 1$

valence band E_v

ε_{h1}
ε_{h2}
ε_{h3}

(b) Density of states

Quantum wells

Barrier
Barrier

DOS

····· Bulk

$n=3$
$n=2$
$n=1$

$E_{g(bulk)}$ E

Quantum wires

Barrier

DOS
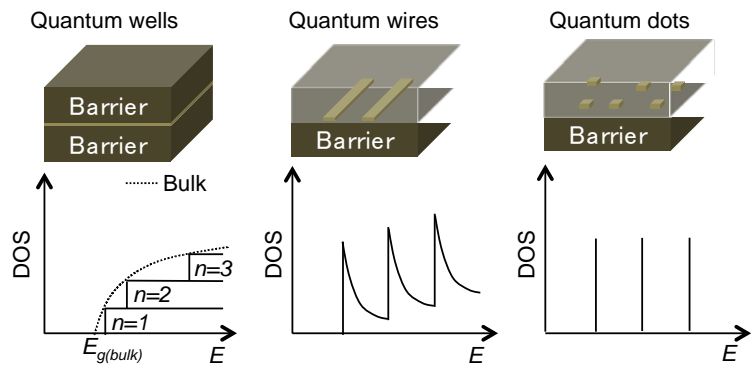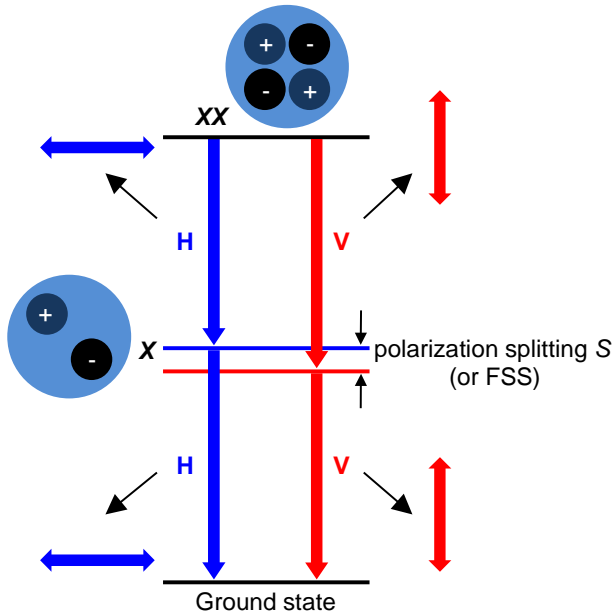
E

Quantum dots

Barrier

DOS

E

Fig. 1.2   (a) Quantum confinement effect and (b) the density of states of quantum wells, quantum wires, and quantum dots.

(a) Typical quantum dot

XX

H   V

X   polarization splitting S (or FSS)

H   V

Ground state

(b) Quantum dots with zero splitting S

XX

R   L

$S = 0$ X

L   R

Ground state

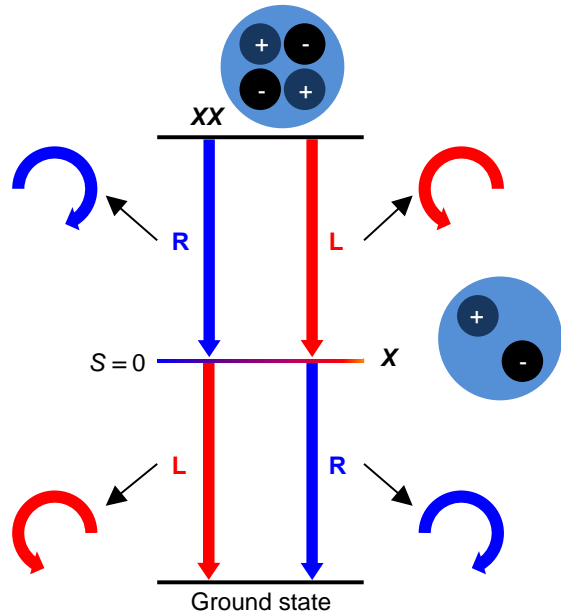**Fig. 1.3   Schematic of biexciton cascade in (a) a QD with a finite polarization splitting S and (b) a QD with zero polarization splitting.**

Many QD manufacturing technologies have been intensively studied. QDs can be formed using epitaxial growth techniques which include molecular beam epitaxy (MBE) and metal-organic chemistry vapor deposition (MOCVD).

Figure 1.4(a) shows the structure of a growth chamber in a MBE machine. The chamber consists of effusion cells, beam shutters, RHEED (reflection high energy electron diffraction) gun and screen, sample holders. In the growth, we can select target materials by opening or closing the beam shutter of effusion cells, and control the growth rate by the temperature of effusion cells. We can analyze the surface structure by RHEED.

Figure 1.4(b) shows the growth mechanism of a GaAs layer on AlGaAs in a growth chamber [59]. Firstly, we create an arsenic atmosphere by closing gallium cell shutter. Then, we supply gallium molecular beam. At this time, gallium molecules drop down to the surface. The dropped gallium molecules react with arsenic on the surface, and they are crystallized. By these techniques, we can precisely control the thickness of epitaxial layer with atomic level, not only grow high quality layers. Based on the epitaxial growth, QD growth techniques are mainly classified into two approaches, top-down and bottom-up approaches.
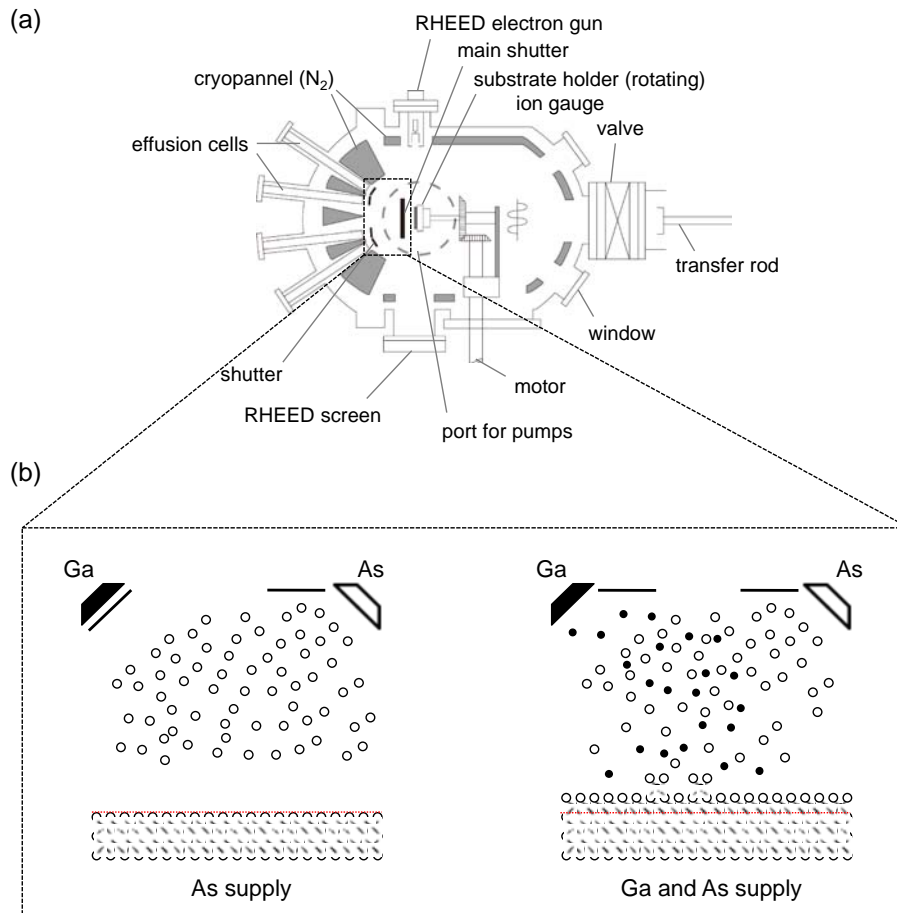

Fig. 1.4   (a) Schematic of the structure of growth chamber in MBE machine. (b) Schematic of the growth mechanism of a GaAs layer on AlGaAs surface in MBE growth chamber.

1.4.1 Top-down approaches

Lithographic techniques: Top-down approach such as lithographic pattering and etching is the most straightforward way of QD fabrication. Figure 1.5 shows schematic of a typical lithographic technique for (a) the etching [17], [60]-[63] and (b) the selective area growth [64]-[69]. For the etching technique (Fig. 1.5(a)), four major steps are needed in process. The sample is first coated by a resist, then exposed and developed. In the case of positive process, the surface of the future QD is open and the rest of the surface is covered by the resist. Next, thin layer of a metal is evaporated on the surface, and resist is removed. The metal layer is deposited directly on the sample surface, which defines the QD for dry etching. For selective area growth (Fig. 1.5(b)), the patterning was firstly performed, then QDs were grown on the substrate by MOCVD normally.

The lithographic techniques have several advantages. The lateral shape, size and arrangement of QDs can be controlled. There are various processing techniques, which can be adjusted for each purpose. It is generally compatible with modern LSI (large scale integrated) semiconductor technology. However, intrinsically, complicated processes are required for high density of QDs. Lithographic processes sometimes induce damaged surface such as defects or impurity contamination. Such damaged surface causes nonradiative recombination. In addition, it is difficult to apply lithographic QD to certain application owing to limited mask size. Many types of QD applications require.

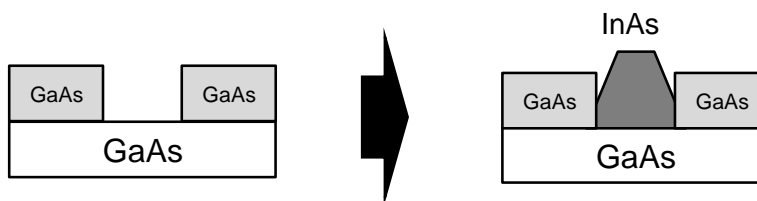### (a) Etching
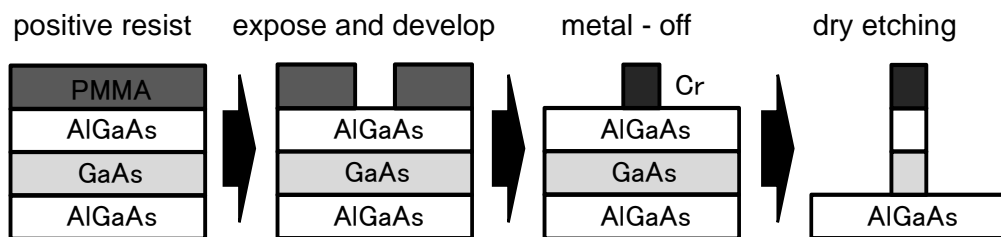
(b) Selective area growth

Fig. 1.5   Schematic of a typical lithographic technique for (a) the etching and (b) the selective area growth.

1.4.2   Bottom-up approaches: Quantum dot self-assembly

Another QD fabrication technique, bottom-up approach, is the self-assembled methods, where QDs grow from the constituent atoms or molecules. The QDs are self-assembly formed by strain energies induced by lattice-mismatch between two epitaxial layers. And also, we can use the surface energy to form QDs. Self-assembled QDs [13], [70]-[74] are defect-free and have highly structural and optical qualities. The size of self-assembled QDs is much smaller than lithographic QDs. It is possible to fabricate small QD (~10nm), with small distribution of size and shape, and high density (>10^{11}cm^{-2}) [75]. In this section, we present two techniques; Stranski-krastanow method [70] and droplet epitaxy method [14].

Stranski-Krastanow (S-K) method: S-K method is the most widely used in the fabrication of QDs. Stranski and Krastanow proposed the possibility of island formation on an initially flat heteroepitaxial surface in 1937. This island growth is therefore called the S-K mode. In the following years the term 'S-K method' was used in heteroepitaxy for formation of islands on an initially two-dimensional layer.

S-K method describes the characteristics of three-dimensional island growth with a thin two-dimensional layer beneath, when a layer of material with larger lattice constant is epitaxially grown on top of a material with smaller lattice constant. The important parameter of the S-K method is the lattice mismatch between the two epitaxial layers. For instance, the common combination of InAs/GaAs system has a lattice mismatch 7%.
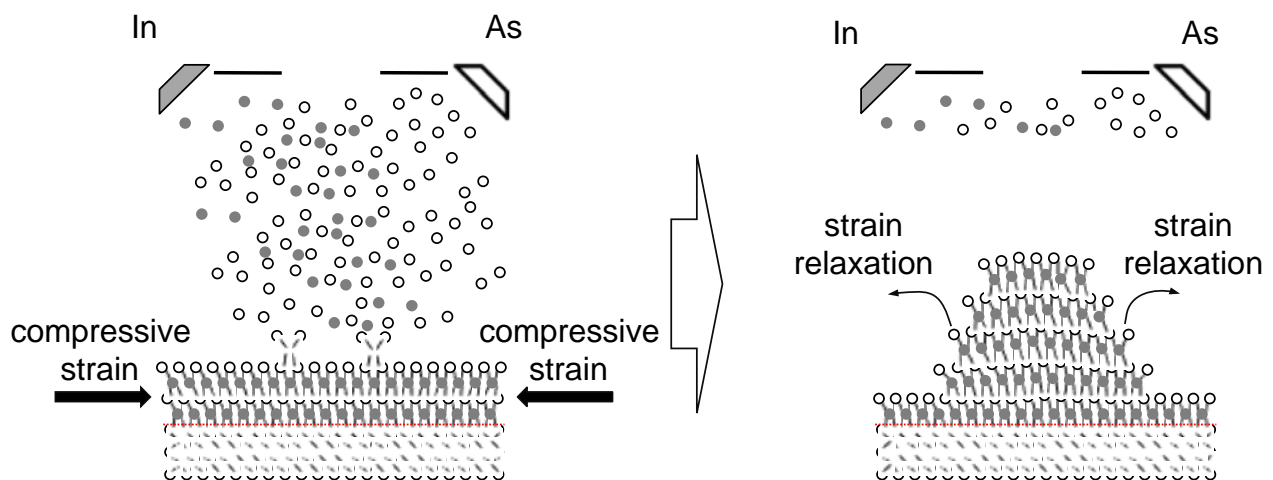

Fig. 1.6   Schematic of InAs QD formation on GaAs in the S-K method using MBE.

Figure 1.6 shows a schematic of InAs QD formation on GaAs in the S-K method using MBE. First, indium and arsenic molecular beam is supplied to GaAs substrate for the formation of a strained two-dimensional layer, which is called a wetting layer. When the strain that accumulates in the wetting layer reaches a certain amount (in the case of InAs/GaAs system, the critical thickness is ~ 3 ML), transition from two-dimensional layer-by-layer growth to three-dimensional islands occurs to reduce strain energy. Naturally, the critical thickness is determined by the degree of lattice-mismatch for selected materials. The properties of S-K QDs such as size, shape, composition and density can be tuned by changing the growth parameters [28], [70], [76]-[79]. However, size fluctuations and randomly distributed nucleation sites are unavoidable. S-K QDs are intrinsically grown only in lattice-mismatched system. Besides, the orientation of growth direction is limited. For instance, S-K QDs cannot be formed on (111) surface, because strain relaxation occurs in the initial stages of growth by introducing threading dislocation [80].

Droplet epitaxy method: The S-K method is prohibited in a lattice-matched system. For QD growth in the lattice-matched system, droplet epitaxy was developed by N. Koguchi et al. [14], which is a non-conventional and emerging growth technique for QD self-assembly [72], [75], [81]-[89]. It enables uniform size distribution in both lattice-matched and lattice-mismatched systems.

Figure 1.7 shows schematic of droplet epitaxy for typical GaAs QDs. The process of droplet epitaxy is performed in an MBE chamber. Before supplying gallium molecular beam to the surface, the substrate is cooled down, and arsenic molecules are almost depleted in the growth chamber. The substrate temperature of 200 – 300 °C is required to limit the migration length of gallium atoms on the surface, and the vacuum level is as low as 1×10^{-9} Torr. After setting such growth condition, gallium molecular beam is supplied to the surface for formation of liquid gallium droplet. Due to the surface energy, gallium forms droplets. When the molecules have a larger surface energy than that of substrate, droplet formation occurs. Note that the wetting angle of droplets depends on surface energy at interface. If the growth procedure is opposite, droplet cannot be formed. By adjusting the substrate temperature, the droplets size can be controlled.
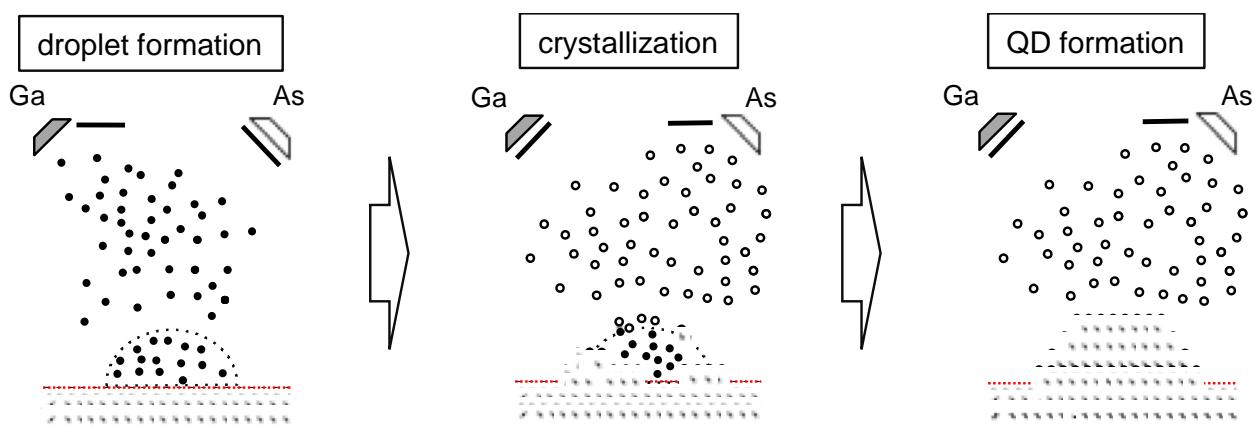

Fig. 1.7 Schematic of droplet epitaxy method for a typical GaAs QDs.

Next, arsenic molecular beam is supplied to the droplets for crystallization. When arsenic molecular beam reach the surface of droplet, arsenic molecules and gallium molecules react to GaAs molecules and the molecules go down to the edge of droplet along the droplet surface. The reached molecules at the edge are crystallized into GaAs QD. In this stage, we can control the morphology of QDs by controlling arsenic intensity and the substrate temperature. For instance, ring or double ring morphology can be formed [90].

For the droplet epitaxy method, an annealing step is essentially required. The QD growth is performed at low temperature compared with normal growth temperature of 580 – 600 °C. Thus, the defect density can be higher and indicate poor optical properties. To reduce the number of defects, annealing is performed. The droplet epitaxy growth is not strain-driven, thereby it allows us to use a variety of material combinations (which include GaAs QDs on Si [87] and Ge [91]) and substrate orientations (which include GaAs (100) [73], [89], [92], (311)A [75], and (111)A [93].

1.5 Current status of droplet epitaxial quantum dots

Since the droplet epitaxy method was developed, QD research on lattice-matched GaAs/AlGaAs system has been actively investigated. In particular, QDs attract much interest due to their potential application in single or entangled photon emitters. For the single photon sources, the investigation of the QD properties related with the structure and optical property is essential. To date, using GaAs QDs via droplet epitaxy, remarkable phenomena such as ultra-narrow emission with small QDs [89], and the optical transition of quantum ring [83], [90], [94] have been demonstrated. For the ideal QD, the spectral emission of a single QD should be sharp. However, the sharp emission has been observed only with small QDs. Spectral line broadening is one of the issues for single photon applications. Thus, a symmetrical study of a single QD and its optical properties is highly desirable.

For the entangled photons, highly symmetric QDs are required. However, in conventional QDs grown on a cubic semiconductor along a [100] crystal axis, QD structure anisotropy occurs due to the C_{2v} symmetry of the surface. As a result, anisotropic electric structure causes, which induces fine structure splitting (FSS) [58] (see Fig. 1.4). This FSS makes radiative transition paths distinguishable, and thus strongly degrading or even prohibiting entanglement for the emitted photons. Recently, laterally high-symmetry QDs have been successfully formed on (111) surface [93]. The (111) surface has C_{3v} symmetry, and due to the C_{3v} rotational symmetry of the growth plane, highly symmetric QDs can form. Therefore, to circumvent the symmetry breaking, QDs forming along the [111] crystal axis with C_{3v} symmetry is promising avenue for the development of practical applications.

Figure 1.8(a) shows an AFM image of highly symmetric GaAs QDs grown on GaAs(111)A via droplet epitaxy. Well-defined QDs are observed as possessing a disk-like shape in AFM image. The cross-sectional

profiles investigated in AFM are identical along two orthogonal directions for most QDs (Fig.1.8(b)). The use of the (111) surface as a growth plane allows us to form laterally symmetrical QDs.

Figure 1.9(a) shows a typical PL spectrum of a single GaAs QD measured at 6 K. It is observed sharp and intense PL emission from QD. Figure 1.9(b) presents a comparison between the absolute value of the FSS in GaAs(111)A QDs and that in (100) QDs as function of the corresponding X emission energy. The magnitude of FSS in (111)A was much smaller than that of (100). This is the direct consequence of the improved symmetry of QDs grown on (111)A with respect to the (100) case.

Figure 1.10 shows coincidence histogram. A positive correlation appears for parallel polarizations (*HH,VV*), while it disappears for perpendicular polarizations (*HV,VH*).This independence of polarization basis is a key to establish quantum entanglement. On (111)A surface, highly symmetric QDs were successfully formed, their QDs exhibit much smaller FSS than that in (100) surface. Furthermore, the QDs shows high entanglement fidelity as 0.86, which is much larger than the classical limit of 0.5, and rates among the best reported in previous studies on dot-based photon sources. These results suggest that (111) substrate is promising to form the highly symmetric QDs.
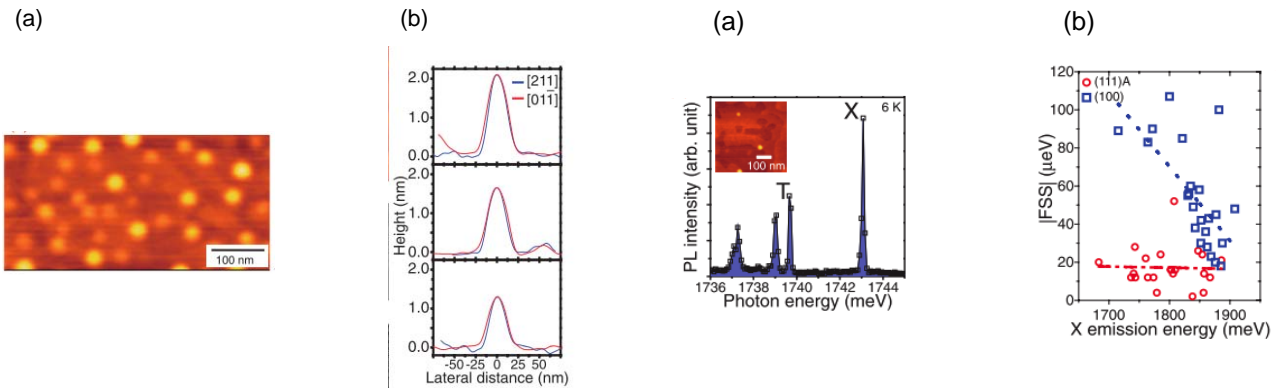
(a)

(b)

(a)

(b)

Fig. 1.8 (a)AFM image and (b) cross-sectional profiles of GaAs QDs on AlGaAs/GaAs(111)A.

Fig. 1.9 (a)Typical PL spectrum of a single GaAs QD at 6 K. (b) Summary of the FSS of QDs grown on (100) (squares in blue) and on (111)A (circle in red).
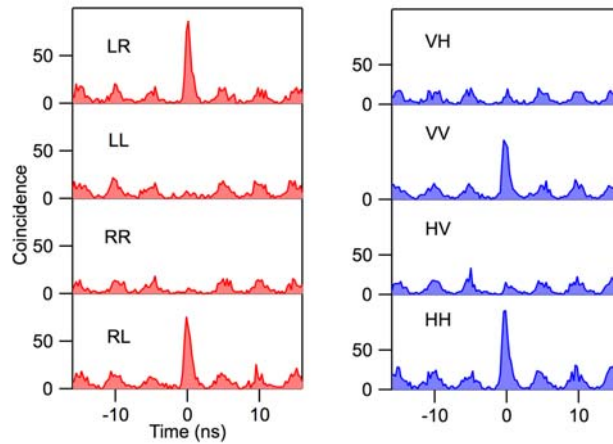

Fig. 1.10 Coincidence histograms between the *XX* and *X* photons for different polarization combination.

For applying the single or entangled photon into optical fiber communications, extension of emitted wavelength to 1.3 or 1.55 μm is essentially required. In optical communication, the three principal windows of operation, such propagation through an optical fiber, are indicated. The windows correspond to the wavelength regions that have low attenuation, and are matched to the ability of transmitters to generate light efficiently and receivers to carry out detection. We can send information efficiently by using these windows. Hence, the QD lasers used in optical communications are required to emit at around 850 nm (first window), 1310 nm (second window), and 1550 nm (third and fourth windows). In particular, the 1.3 μm or 1.55 μm emission wavelength are essential for long-distance communication, due to them being in the lowest attenuation regions.

For QDs emitting at telecommunication wavelength, progress in the development of telecom-band QDs has been made using InP substrates [95]-[99]. However, the widely used S-K growth method cannot be applied to form QDs on (111) substrate. Compared with InP-based approach, it is challenging to fabricate high-quality telecom QDs based on GaAs. An essential difficulty in the use of GaAs substrates comes with large lattice mismatching between InAs and GaAs.

Figure 1.12 shows schematics of effect of strain on the bands of a semiconductor. The epitaxial layer has a lager lattice constant (Fig.1.12(a)), is unstrained (Fig.1.12(b)) to show usual band structure, and has a smaller lattice constant (Fig.1.12(c)). Compressive strain leads its bandgap to be larger, tensile strain is opposite. Thus, strong compressive strain in InAs QDs/GaAs leads their emission wavelength to be shorter than ~1.0 μm, which is far from telecom windows. The introduction of strain-reduced layers, which embed or cap QDs, allows to achieve 1.3 μm [28], [100]. Further wavelength extension to 1.55 μm requires high indium concentration in the matrix or QDs, while their growth on GaAs easily suffers from dislocations. A promising approach to restrain dislocations is the use of a metamorphic buffer layer as a virtual substrate for the succeeding epitaxial growth [101], but its repeatability is a serious issue.
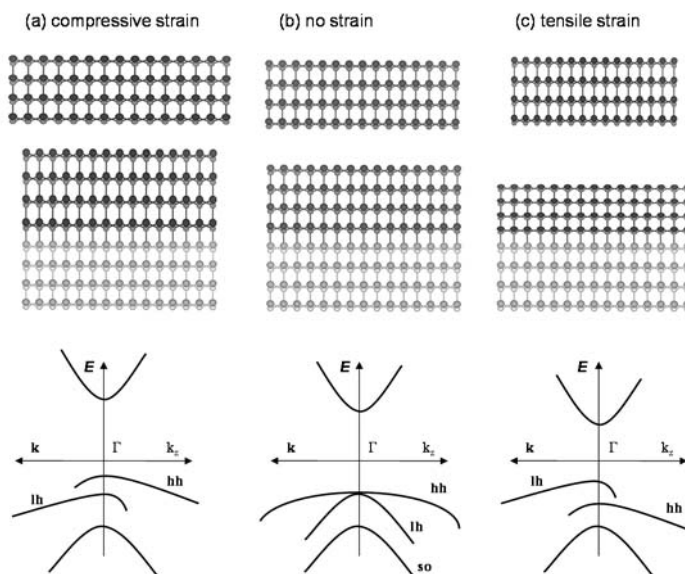

Fig. 1.11 Effect of strain on the bands of a semiconductor. The epitaxial layer has a lager lattice constant in (a), is unstrained in (b) to show usual band structure, and has a smaller lattice constant in (c).

1.6 Scope of this thesis

This thesis is concerned with the growth of self-assembled GaAs and InAs QDs via the droplet epitaxy method. Depending on the QD morphology, their optical properties were mainly studied.

Controlling the QD morphology is essential for practical applications, and an analysis of the relationship between the QD structure and their optical properties is essential requirement to this end. For an AlGaAs-GaAs system, it is the best-developed and currently dominant physics experiment, due to it having almost the same lattice constant. It is relatively easy to grow a good interface of AlGaAs on the top of GaAs, as the microscopic structure of each material is not distorted in a heterostructure. However, in lattice-matched system, the S-K mode cannot be used because the transition from two-dimensional layer to three-dimensional islands occurs due to strain energy. This limitation of self-assembled growth based on the S-K mode is overcome through the droplet epitaxy method.

The highly symmetric QDs on the (111) surface are a promising candidate for entangled photon emission. The InAs/InP system is suitable for emission at telecommunication wavelengths. However, S-K growth is prohibited on the {111} surface. We demonstrate highly symmetric InAs QDs on InP(111)A grown by droplet epitaxy. Compared with the InP-based approach, it is challenging to fabricate high-quality telecom QDs based on GaAs. An essential difficulty in the use of GaAs substrates comes with large lattice mismatching between InAs and GaAs. Therefore, we developed a new growth technique for lattice relaxation and grew InAs QDs on InAlAs/GaAs(111)A emitting at telecommunication wavelength.

Chapter 2 describes the structural and optical properties of GaAs QDs grown on GaAs (100). We demonstrate that the height of GaAs QDs is controlled by droplet epitaxy, and study the optical properties depending on the height of a single QD.

Chapter 3 presents the growth of highly symmetric InAs QDs on InAl(Ga)As/InP(111)A. The growth mechanism of InAs QDs on InAlAs/InP(111)A is identified, and the optical properties of ensemble and single QD are studied.

In chapter 4, we propose a new growth technique for the formation of InAs QDs on the GaAs substrate. A technique for strain-relaxation between InAlAs and GaAs is discussed. The growth of InAs QDs on InAlAs/InAs/GaAs (111)A are demonstrated, and also their optical properties are confirmed.

In chapter 5, we summarize the findings and conclusions, discussing the implications and future works.

CHAPTER 2

Droplet epitaxy of GaAs quantum dots

2.1 Motivation

The size and the shape control of QDs is a central issue in QD engineering. One of the advantages of strain-free GaAs/AlGaAs QDs is that we can avoid changing QD morphology and composition when QDs are capped by a barrier layer. However, QD growth using S-K method is prohibited in lattice-matched systems. In this chapter, we propose the fabrication of height-controlled GaAs QDs on AlGaAs/GaAs(100) by droplet epitaxy. In addition, we discuss spectral broadening of single QDs depending on the height.

2.2 Experimental details

The schematic of sample structure is shown in Fig. 2.1. We carried out the following growth sequence:

0. Installation of semi-insulating GaAs(100) as a substrate

1. Growth of a 300 nm GaAs buffer layer at 580 °C

2. Growth of a 100 nm $Al_{0.3}Ga_{0.7}As$ barrier layer at 580 °C

3. Cool down the substrate to 200 °C

4. Supply of gallium with 1.5, 2, 3, 5, 7.5, and 10 ML at 0.5 ML/s (without As_4 flux). This step enables the formation of gallium droplets.

5. Supply of an As_4 flux with 2.5×10^{-4} Torr at 200 °C. This step enables the crystallization of gallium droplets to GaAs QDs.

6. Annealing at 400 °C for 10 min under As_4 supply

7. Partial capping with a 20 nm $Al_{0.3}Ga_{0.7}As$ layer at 400 °C

8. Annealing at 580 °C for 5 min

9. Capping with a 30 nm $Al_{0.3}Ga_{0.7}As$ layer followed by 10 nm GaAs layer at 580 °C

In the above sequence we could prepare GaAs quantum dots embedded in an AlGaAs. For the investigation of QD morphology, we also grew GaAs QDs on the top:
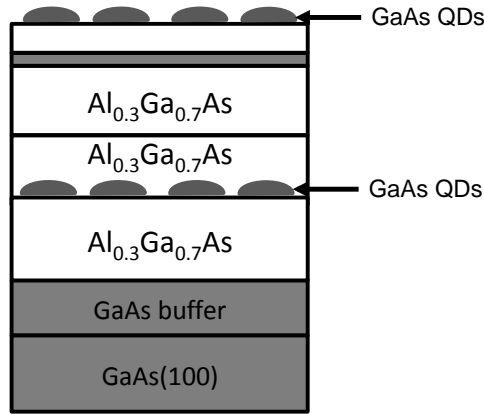
Fig. 2.1   Sample structure of GaAs QDs in Al$_{0.3}$Ga$_{0.7}$As on GaAs(100).

10. Growth of a 2 ML Al$_{0.3}$Ga$_{0.7}$As at 580 °C

11. Growth of GaAs QDs following the same procedure

12. Rapid thermal annealing at 800 °C for 4 min under N$_2$ atmosphere. This step is to improve crystal quality.

Atomic force microscopy (AFM) was used to characterize the surface morphology. Cross-sectional scanning tunneling microscopy (STM) was used to study the structural properties of capped QDs.

2.3   Morphology analysis

Figure 2.2 shows the AFM image of GaAs QDs grown by droplet epitaxy with different amount of gallium supply; 1.5, 2, 3, 5, 7.5, and 10 ML. Well-defined QDs with density of 1.1×10^{10}/cm^2 are formed in all samples. Thus, the amount of gallium does not strongly affect on the density, but on the volume of dots. The results suggest that an increase in gallium supply does not enhance nucleation, but leads only to volume expansion.

Figure 2.3 shows the cross-sectional profile along [110] direction for a typical QD in each sample. They exhibit a truncated pyramidal shape [102]-[104]. We observed that with increasing the amount of gallium, QD height increased by a factor of 10, but the lateral size increased by a factor of less than 2.

The distribution of QD height is presented in Fig. 2.4. For the 1.5-ML QDs, the mean height is 2.3 (σ: 0.5) nm, where σ is standard distribution. By increasing the amount of gallium, both the mean height and the distribution steadily increase. Thus, small QDs are uniformly formed.

Figure 2.5 shows the dependence of the average height of GaAs QDs on the amount of gallium. the average height of QDs increases from 2.3 to 23.6 nm with increasing the amount of gallium from 1.5 to 10 ML.
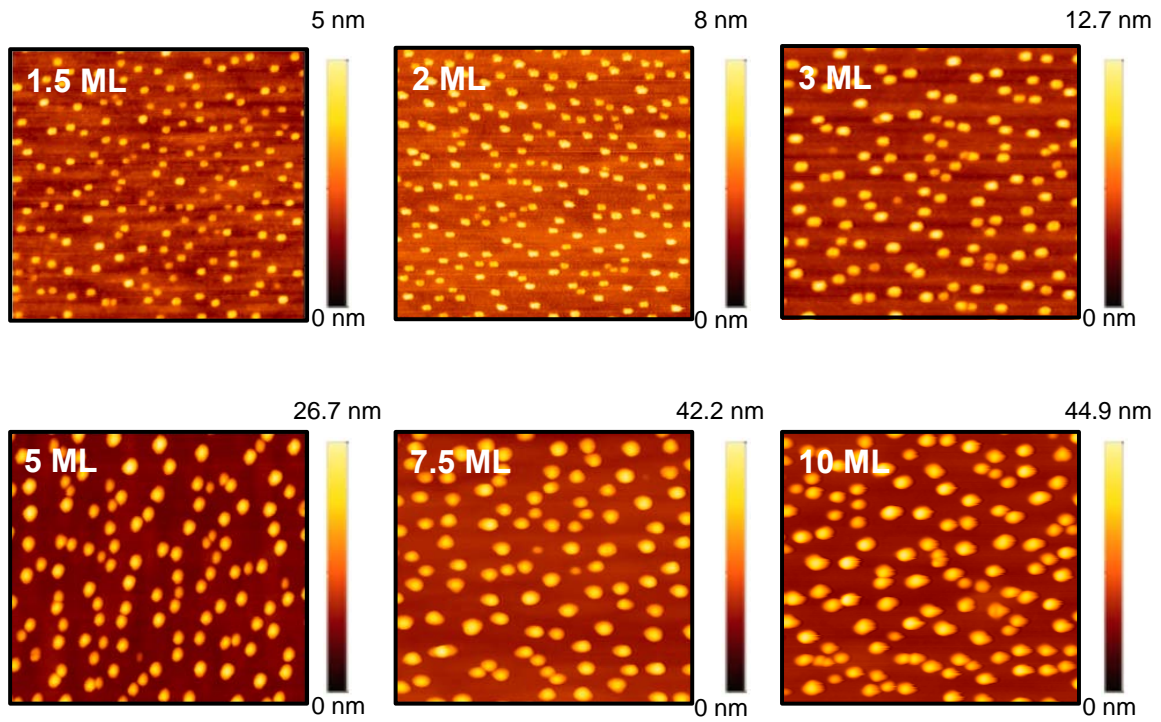
Fig. 2.2 AFM images of GaAs QDs grown by droplet epitaxy with different amount of gallium supply; 1.5, 2, 3, 5, 7.5, and 10 ML.
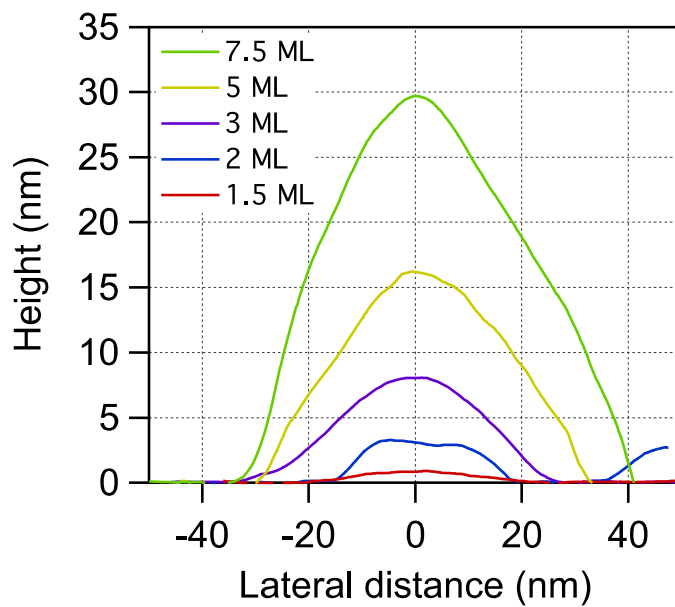

Fig. 2.3 Cross-sectional profiles of typical GaAs QDs with different gallium deposition.
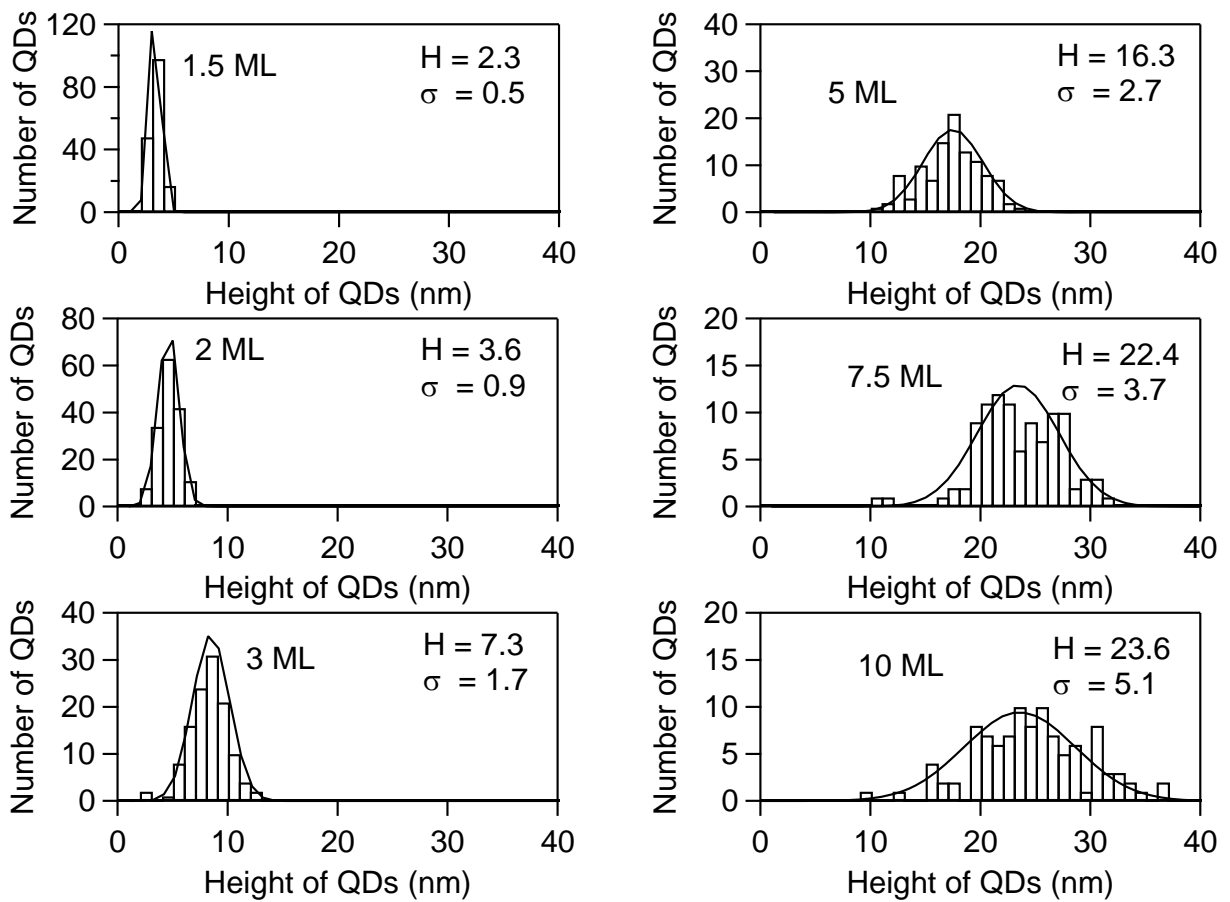
Fig. 2.4 The bars show the height statistics of GaAs QDs. The solid lines show normal distributions fitted to the data. The mean height (H) and standard distribution (σ) are also indicated.
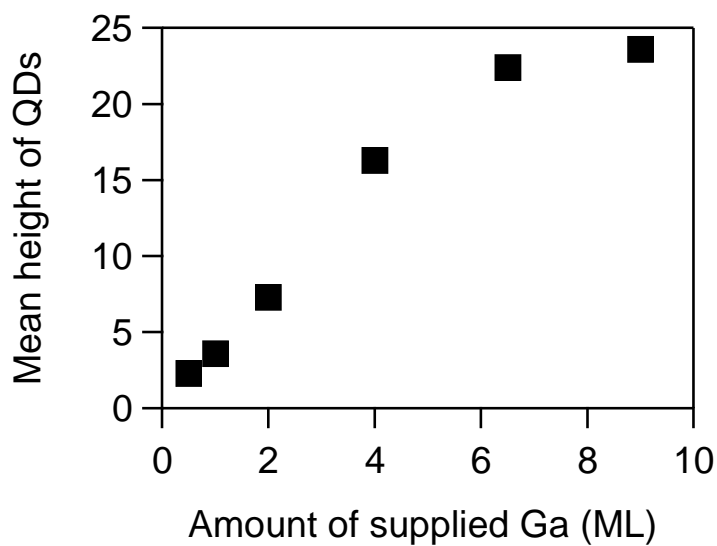

Fig. 2.5 Dependence of the average height of GaAs QDs on the amount of gallium.

Figure 2.6 shows the cross sectional STM image of QDs capped by AlGaAs. The QD image exhibits a truncated pyramidal shape, and is nearly the same with the AFM image of uncapped QDs. Thus, GaAs QDs are capped by AlGaAs with maintaining their original shape. The small diffusion length of Al atoms allows the QD shape unchanged.

Figure 2.7 shows the schematic drawing of a possible growth mechanism in this system. The crystallization from gallium droplet to GaAs starts to occur at the edge of droplets. Then, shallow side facets form, and become steeper. Finally, the most stable (111) facets appear. This is why large droplets become tall QDs.
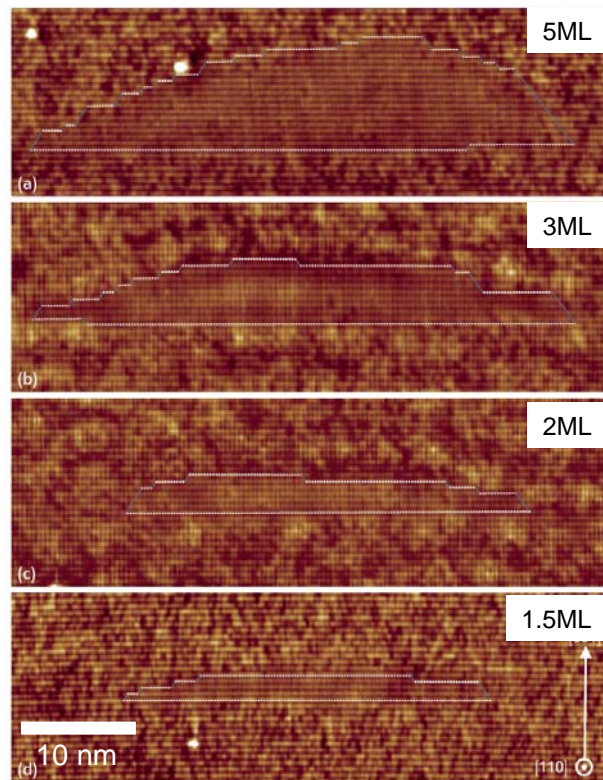
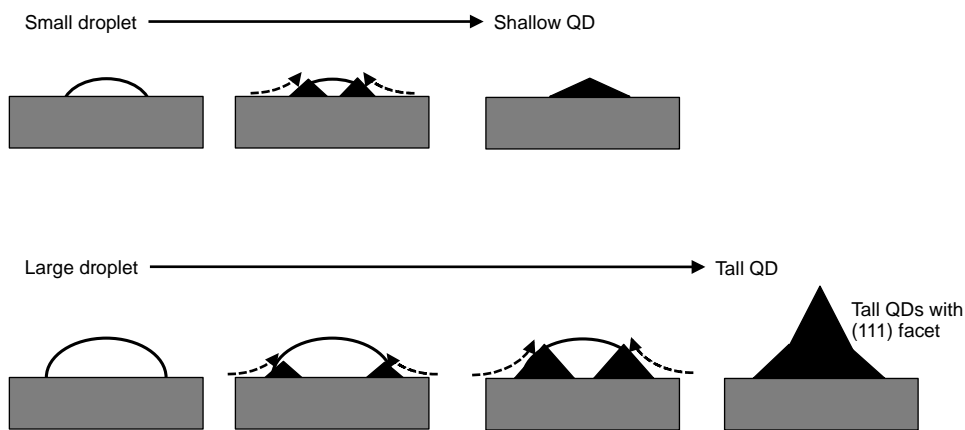**Fig. 2.6   Cross-sectional STM images of GaAs QDs capped by Al$_{0.3}$Ga$_{0.7}$As.**

Fig. 2.7   Schematic drawing of a possible growth mechanism of GaAs QDs by droplet epitaxy.

2.4 Optical properties

Measurement setup: Optical properties were analyzed by low-temperature photoluminescence (PL) measurement on both ensemble and single QDs. A 532 nm wavelength laser was used for excitation. The collected PL signal was dispersed by a monochromater with a spectral resolution of 200 μeV (0.07 nm) in full width at half maximum (FWHM).

We measured micro PL for the analysis of individual QDs. Figure 2.8 shows the schematic of the micro PL set-up. The excitation beam was focused by a micro objective lens with a numerical aperture of 0.55 and a focusing length of 4 mm, and the PL emission was collected by the same lens. Notable is that a solid immersion lens was used to reduce a spot size. Thus, emission from a single QD can be observed even in the high-density samples. In this set up, the spot diameter is around 0.5 μm. Thus, we expect that 25 dots are detected.
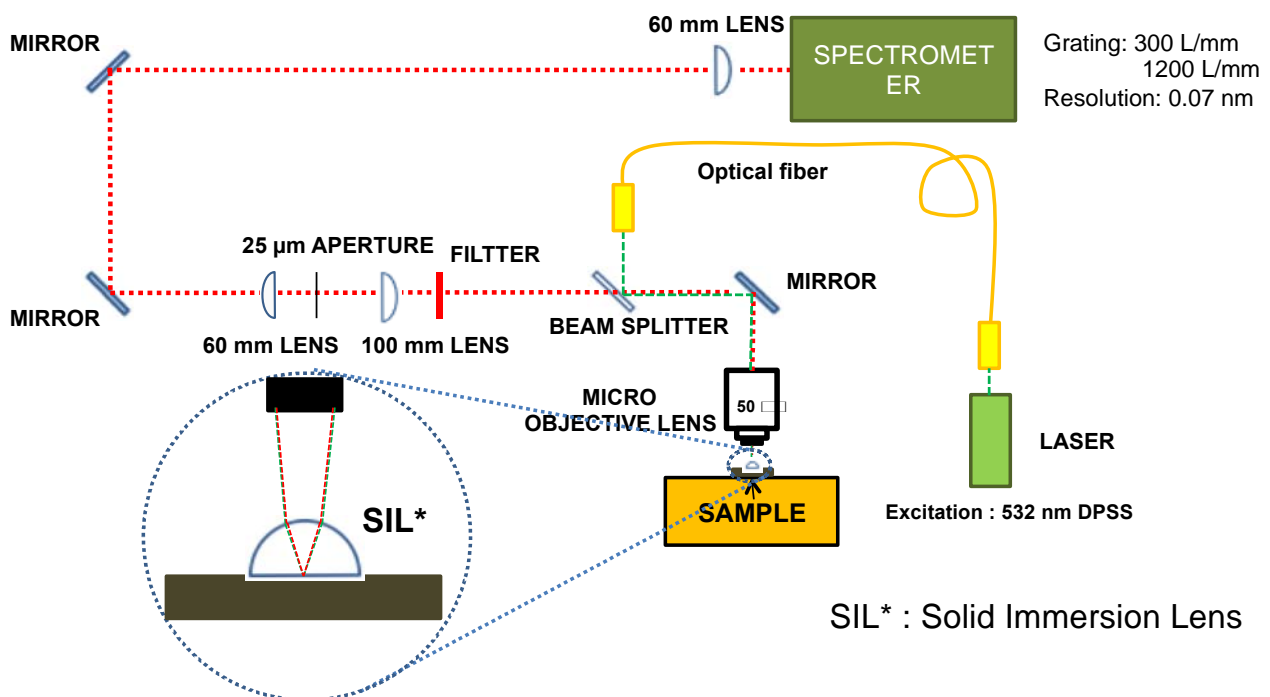

Fig. 2.8   Schematic of the micro PL set-up.

Ensemble measurements: Figure 2.9 shows the PL spectra of capped QD ensembles at 9 K. Two peaks at around 1.5 eV are observed for the most samples. They originate from the GaAs substrate.

The PL spectrum of 1.5 ML GaAs QDs is observed at around 1.85 eV (670nm). The PL spectrum of 2 ML QDs is observed at 1.8 eV (690 nm), and that of 5 ML QDs at 1.67eV (745 nm). Thus, the emission peak is shifted to low energy side with increasing QD size. This is because the energy of large QDs is lower than that of small QDs.

Simultaneously, the line width of the spectra increases from 74 meV (1.5 ML) to 128 meV (2 ML) and 170 meV (5 ML). Thus, the distributions of QD size increases with increasing the QD height. This result agrees with the AFM result, where the height of 2.3 ± 0.5, 3.6 ± 0.9, and 16.3 ± 2.7 nm was observed in the 1.5, 2, and 5 ML sample, respectively.

Different behaviors appear for relatively large dots: The PL spectra of 7.5 and 10 ML QDs show emission bands whose width are 27, and 26 meV, respectively. Thus, the line width is almost unchanged. This result contradicts the AFM result where higher size distribution was observed for larger QDs. This is due to the weak size dependence of the quantization energy for such large dots. Since the PL energy is close to the bulk band gap of GaAs, it depends only weakly on the size.
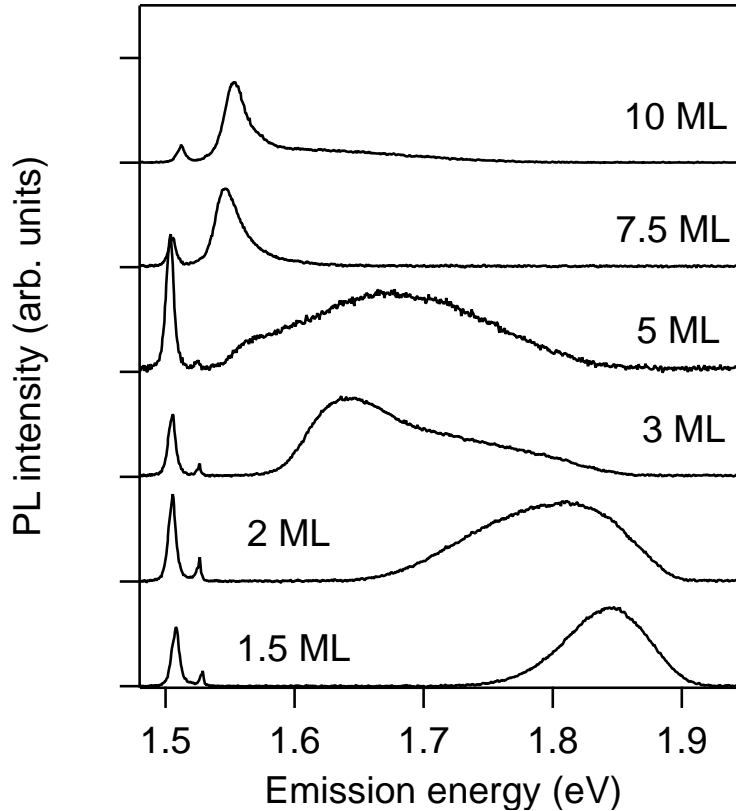

Fig. 2.9   PL spectra of the ensemble of GaAs QDs at 9 K.

Single quantum dot measurements: Figure 2.10 shows the typical micro PL spectra of (a) 1.5 ML, (b) 5 ML, and (c) 10 ML QDs. The PL signal of 1.5 ML QDs consists of very sharp lines whose line widths are less than the resolution of our spectrometer (200 μeV in FWHM) (Fig. 2.10(a)). The PL signal of 5 ML QDs shows significant broadening (Fig. 2.10(b)). The PL signal of 10 ML QDs shows large broadening (Fig. 2.10(c)).
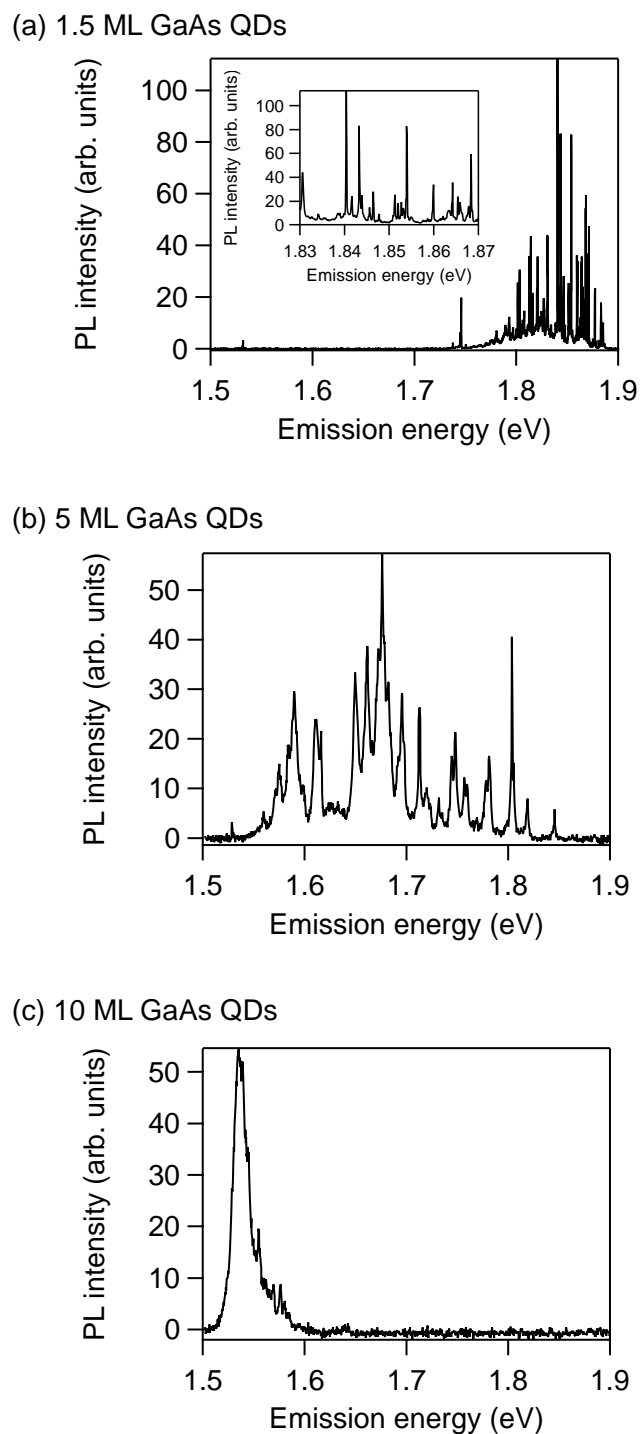
(a) 1.5 ML GaAs QDs

(b) 5 ML GaAs QDs

(c) 10 ML GaAs QDs

Fig. 2.10   Typical micro PL spectra of (a) 1.5, (b) 5, and (c) 10 ML GaAs QDs.

Figure 2.11 shows a comparison between the PL spectra of (a) a large ensemble of QDs and (b) small numbers of QDs measured using a micro objective. We found that spectral bands in the ensemble spectra consisted of large numbers of spectral lines, each of which arose from isolated QDs. The number of spectral lines in the micro PL samples for 1.5 ML samples is around 70, which is consistent with the number of QDs inside a focusing spot.

Figure 2.12 shows the dependence of line width on the PL energy. The line width increases with decreasing emission energy, i. e., with increasing QD height. The size dependence is independent of the choice of samples, thus it is universal behavior found in all samples.
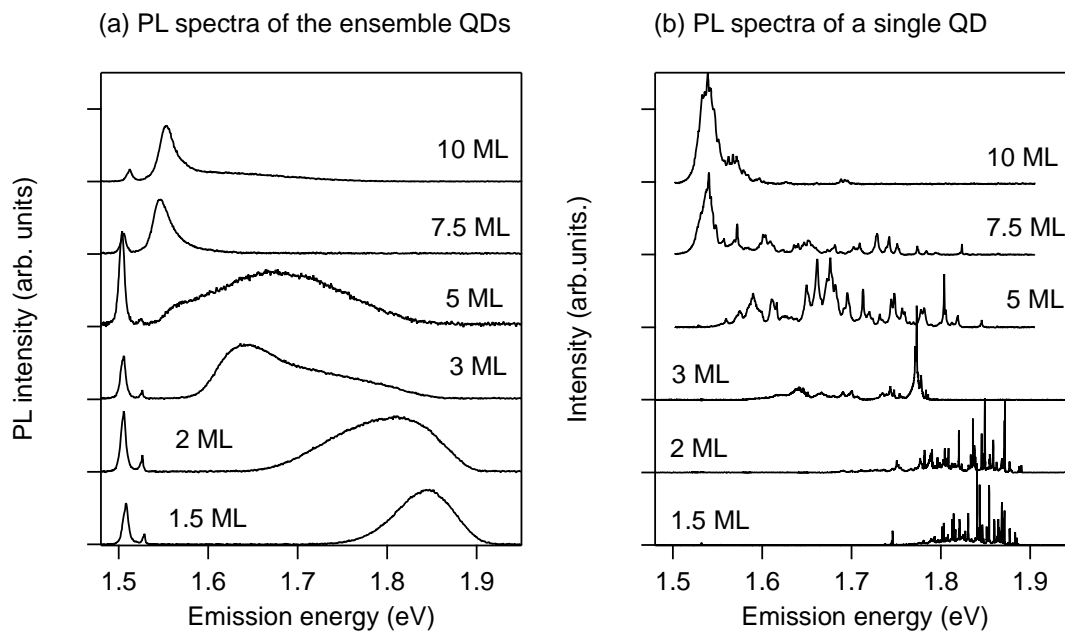

Fig. 2. 11   Comparison between the PL spectra of (a) an ensemble of QDs and (b) single QDs measured using a micro objective.
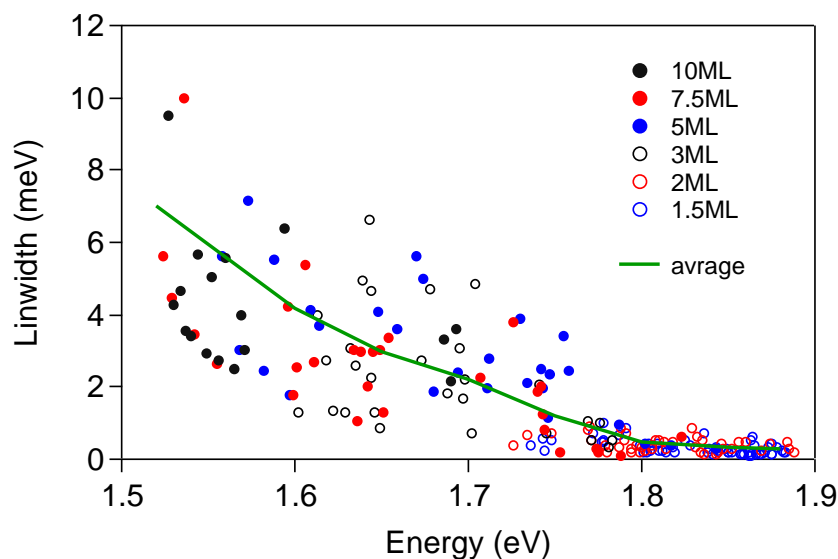

Fig. 2.12   Dependence of line width on the PL energy.

Spectral broadening induced by Stark effect: We consider that spectral broadening is due to the random motion of external charges, which lead to the fluctuation of an electric field. Figure 2.13 is the schematic of how the band diagrams changes depending on an electric field. Figure 2.13(a) shows the band diagram when an electric field is absent. In this case, the PL spectrum becomes delta function-like. Figure 2.13(b) shows the diagram when an electric field is applied to QDs. In this case, the PL spectrum shifts with the field strength, the phenomenon of which is called the quantum confined Stark effect [105], [106]. In the presence of external charges, which fluctuate in time, the electric field also changes, causing spectral broadening after time integration.
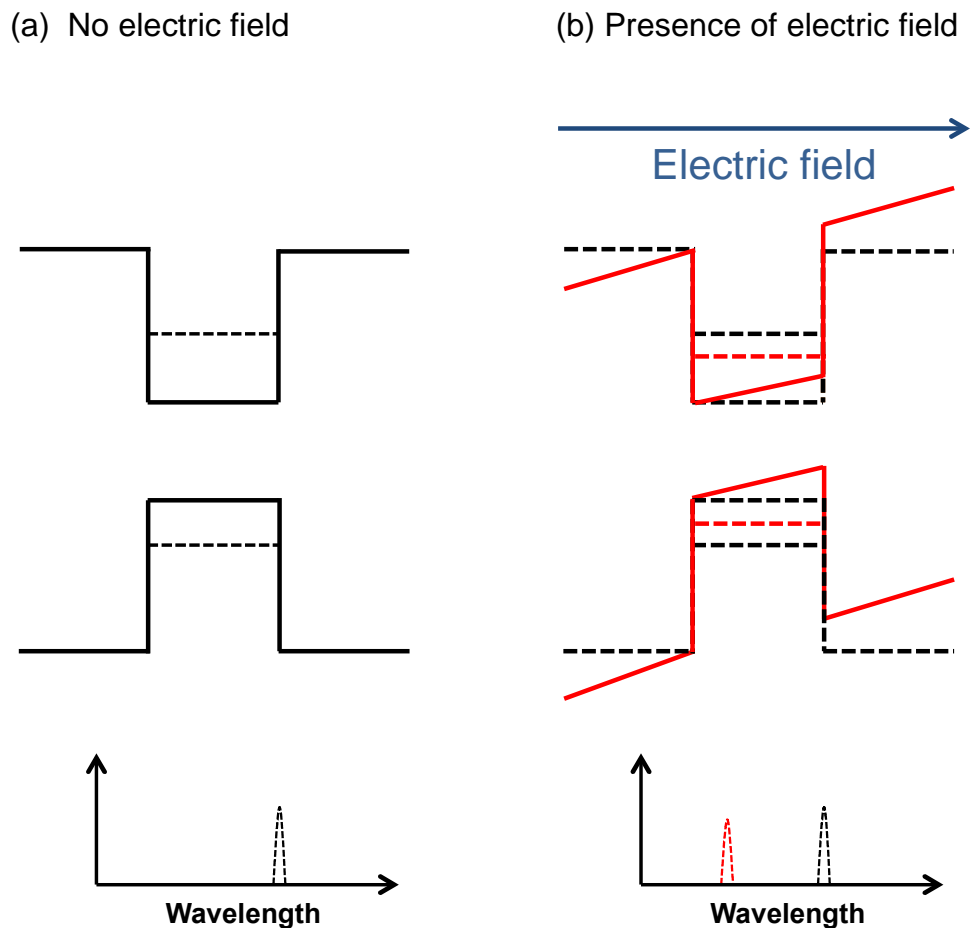
(a) No electric field

(b) Presence of electric field

Electric field

Wavelength

Wavelength

Fig. 2.13 (a) The energy diagram of QDs in the absence of an electric field, and (b) that in the presence of an electric field.

Theory of size dependent line broadening: We will present qualitative analysis on line broadening in the PL spectra of a single QD. First, we will derive an analysis form of a Stark coefficient as a function of QD size. Second, we will evaluate an electric field induced by random surface charges, and its fluctuation width. Finally, we will compare calculated line width and experimental data.

Size dependence of Stark coefficient: We derive an analytic form of Stark shift in a quantum box surrounded by an infinite barrier. The wave function and its eigen energy in the absence of an electric field are given by

$$\psi(x,y,z) = \sqrt{\frac{8}{L_x L_y L_z}} \sin\left(\frac{n_x \pi}{L_x} x\right) \sin\left(\frac{n_y \pi}{L_y} y\right) \sin\left(\frac{n_z \pi}{L_z} z\right), \tag{2.1}$$

$$E_{n_x n_y n_z} = \frac{\pi^2 h^2}{2m}\left\{\left(\frac{n_x}{L_x}\right)^2 + \left(\frac{n_y}{L_y}\right)^2 + \left(\frac{n_y}{L_z}\right)^2\right\}, \tag{2.2}$$

Where each quantum number n_x, n_y, and n_z starts from 1. We discuss the influence of an electric field F parallel to z on the ground state level $(n_x n_y n_z) = (111)$, whose unperturbed energy is

$$E_1 = E_1^{XY} + \frac{\pi^2 h^2}{2m}\frac{1}{L^2}, \tag{2.3}$$

where E_1^{XY} is the lateral confinement energy and will be treated as a constant. Note that $\pi^2 h^2 / 2m = 376.13$ meV $\cdot$ nm^2. Stark shift E_s is described by the second-order perturbation of the interaction Hamiltonian, i.e.,

$$E_s = \sum_{n\geq 2} \frac{|\langle\psi_1|eFz|\psi_n\rangle|^2}{E_1 - E_n} = (eF)^2 \sum_{n\geq 2} \frac{Z_{1n}^2}{E_1 - E_n}, \tag{2.4}$$

where $Z_{1n} = \langle\psi_1|z|\psi_n\rangle$ is a dipole moment, and expressed by

$$Z_{1n} = \begin{cases} \dfrac{-4n(1+\cos(n\pi))}{(n-1)^2 \pi^2} & n = 2, 4, 6, \dots \\ 0 & otherwise. \end{cases} \tag{2.5}$$

We consider the energy shift of the ground state due to its mixing the second-lowest state. The dipole moment and the energy denominator in this case are

$$Z_{12} = -\frac{16}{9\pi^2} L \approx -0.180L \ (nm), \tag{2.6}$$

$$E_1 - E_2 = -\frac{\pi^2 h^2}{2m}\frac{3}{L^2} \approx \frac{-1128}{m^* L^2}\left(\frac{\text{meV·nm}^2}{\text{nm}^2}\right), \tag{2.7}$$

where m^* is the dimension-less ratio of an effective mass. Then, we obtain,

$$E_s = (eF)^2 \frac{z_{12}^2}{E_1-E_2} \approx -2.87 \times 10^{-7}m^*(eF)^2L^4,$$

(2.8)

where we use the unit system such that ΔE in meV, eF in keV/cm (= 0.1 meV / nm), and L in nm. We find that ΔE is proportional to the square of a field strength and the fourth power of QD size along a built-in field. The optical transition energy is the summation of the energy shift of an electron and that of a hole. Figure 2.14 shows the spectral shift of a 15 nm high GaAs QD with $m_e^* = 0.067$ and $m_h^* = 0.5$ as a function of a field. It reveals squared dependence on the applied field. Note that the above calculation shows excellent agreement with the results of more accurate treatment based on the 4 band $\mathbf{k} \cdot \mathbf{p}$ calculation for finite barrier quantum dots [107].

Substitution of Eq. 2.3 to Eq. 2.8 provides the relation between the Stark shift and the energy of confinement along $z, E_1^z = E_1 - E_1^{XY}$

$$E_s \approx -4.06(eF)^2 \left(\frac{1}{m_e^*} + \frac{1}{m_h^*}\right)\left(\frac{1}{E_1^z}\right)^2.$$

(2.9)

Thus, the energy shift is inversely proportional to the square of the confinement along the field direction.

Evaluation of a fluctuating electric field: A variety of microscopic origins can induce a local electric field in the vicinity of dots. First, charged particles trapped to impurities serve as a field source. Charging and discharging in these charged centers would lead to field fluctuation, and broadening in spectral lines through time integration. We expect, field strength associated with impurities is too low to realize the observed broadening, in view of the fact that MBE growth achieves a high-quality layer with a sufficiently low impurity level. Despite the impurity effect, we propose the effect of surface-trapped charges on spectral broadening.
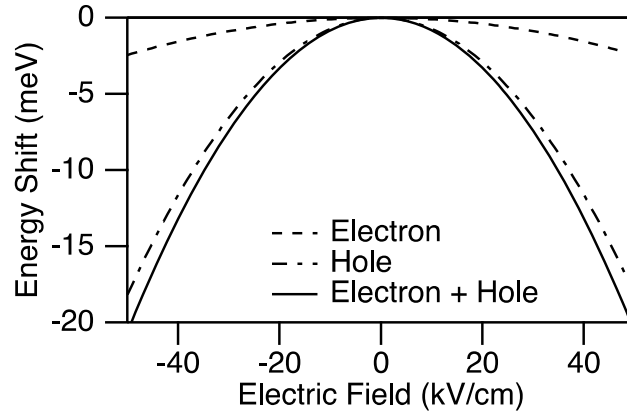

Fig. 2.14 **Calculated Stark shift for a 15 nm high GaAs QD surrounded by an infinite barrier for** $m_e^* = 0.067$ **and** $m_h^* = 0.5$ **as a function of a vertical electric field.**

The formation of surface states is linked to the presence of dangling bonds at the vacuum-semiconductor interface. It is known that their density becomes as high as ~ 10^{12} cm^{-2}, and their polarity is material dependent (they are donor-like states for GaAs, and acceptor-like for InP). When the sample is shined by light, some of photo-injected charges are trapped by surface states, which produce a local electric field. The effect also serves as band bending, or Fermi-level pinning in doped semiconductors. Random change in the microscopic arrangement of surface charges gives rise to a fluctuation in on electric field, which is normal to surface on average.

We evaluate the magnitude of a fluctuating electric field by Monte Carlo simulation. In this simulation, we have calculated an electric field at a point of x_0, which is induced by 1000 electrons that are randomly positioned at x_i ($i = 1, 2, \ldots, 1000$) in a layer, i.e.,

$$F_z(X_0) = \frac{1}{4\pi\epsilon\epsilon_0}\Sigma_{i(\leq 1000)}\frac{\cos\theta_i}{|X_0 - X_i|^2}.$$
(2.10)

Figure 2.15 shows a field strength along z direction at a point 50 nm away from a surface. This condition reproduces the geometry of our QDs. We take dielectric constant $\epsilon = 13$ and the charge density $\sigma = 1 \times 10^{12}$cm^{-2}. It is found that the field strength randomly charges for different charge arrangement. The histogram shows a normal distribution with a mean value of 70 ($\pm$9) keV/cm. Note that the mean value agrees with the value expected with an analytic from for an infinite sheet with uniform charges, i.e.,

$$F_z = \frac{\sigma}{2\pi\epsilon\epsilon_0} \approx 69.68 \text{ kV/cm}.$$
(2.11)

Thus, we expect that the field strength is proportional to the charge density, and its fluctuation width is proportional to the square root of the density, and the inverse of the dot-surface distance.
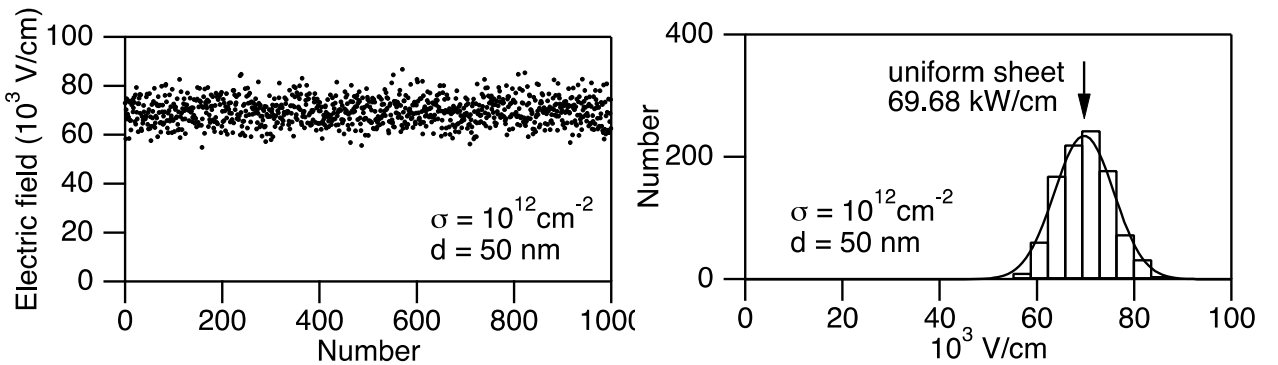

Fig. 2.15   Monte Carlo simulation for electric fields induced by randomly positioned surface charges with a density of 1×10^{12}cm^{-2} at a point 50 nm away from the surface layer.

Comparison between theory and experiment: When an electric field is fluctuated around F_0 with $\pm\Delta F_0$, Stark shift $E_s(F) \propto F^2$ is fluctuated so that

$$\Delta E_s \approx \Delta F_0 \frac{\partial E_s(F)}{\partial F}\bigg|_{F=F_0} = 2E_s(F_0)\left|\frac{\Delta F_0}{F_0}\right|. \qquad (2.12)$$

The above equation and Eq. 2.9 provides the dependence of line broadening on QD energy. Figure 2.16 shows calculated line width for different density of surface charges, 10^{11}, 10^{12}, and 10^{13}cm^{-2}. Fair agreement with experimental data is found when σ is on the order of 10^{12}cm^{-2}.

Spectral broadening in the PL signal of a single QD is an interesting phenomenon which bridges microscopic random dynamics and macroscopic optical response, but is unfavorable for practical applications of QDs to photon emitting devices. The present results suggest several possibilities to engineer spectral broadening. First, we expect to suppress line broadening by preparing QDs with a small height, and low aspect ratio. We have observed very sharp resonance for disk-liked QDs, as expected. Second, the line width is expected to be smaller when QDs are embedded more deeply in the barrier, where the effect of surface charges would be smoothed out.
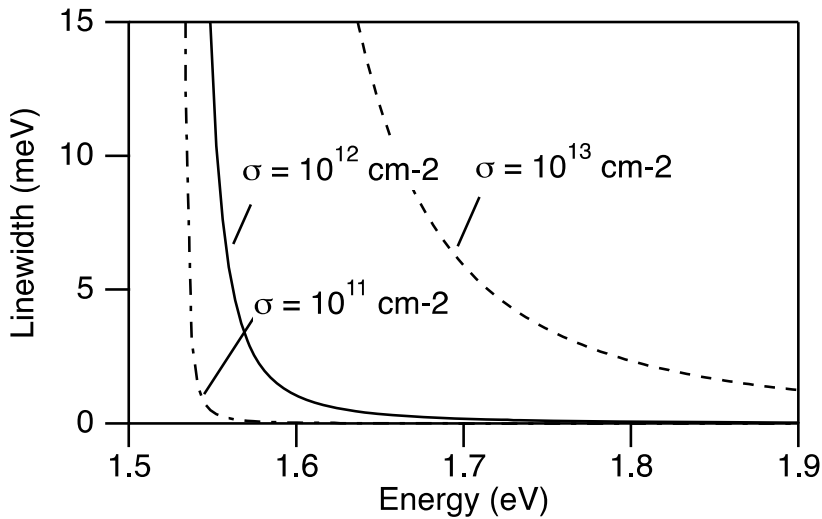

Fig. 2.16   Line broadening due to surface charges with different densities.

2.5　Summary of chapter 2

We fabricated GaAs QDs on AlGaAs/GaAs(100) substrates by droplet epitaxy. We controlled the height of QDs by increasing the amount of gallium supply.

We observed high-yield PL emission, which showed a narrow line width of ensemble spectra. The line width was as narrow as 75 meV for the case of 1.5 ML sample, indicating the uniform QD height. The emission wavelength was red shifted with increasing QD height.

In the single QD emission, the PL signal of small QDs showed a very sharp line. The line width increased with increasing QD height. We consider that the line broadening is caused by the quantum confined Stark effect.

Droplet epitaxy enabled us to adjust QD height without using strain. In S-K QDs, defects can be easily formed for large dots due to strain induced by lattice-mismatch. Thus, we believe that droplet epitaxy is promising for fundamental study of QDs properties.

CHAPTER 3

Droplet epitaxy of InAs quantum dots on InP(111)A

3.1 Motivation

Highly symmetric QDs on (111) surfaces stimulate interests due to their potential application to entangled photon emitters. Since QDs cannot form on (111) surfaces using widely studied S-K growth methods, various alternative methods such as pyramidal site control [41], nanowire technique [67], and droplet epitaxy have been proposed. Especially, highly symmetric GaAs QDs on GaAs(111)A substrates have recently been demonstrated by our group [93].

For optical communication, QDs emitting at a wavelength of 1.3 and 1.5 μm are highly desired. To achieve wavelength extension, InAs QDs on InP substrates are an ideal system [95], [98], [99], [109]. In this chapter, we investigate the droplet epitaxy of InAs QDs on InAlAs/InP (111)A.

3.2 Experimental details

The schematic of sample structure is shown in Fig. 3.1. We carried out the following growth sequence:

0. Installation of semi-insulating (Fe-doped) InP(111)A as a substrate

1. Growth of a 100 nm $In_{0.52}Al_{0.48}As$ layer (lattice-matched to InP) at 470 °C

2. Cool down the substrate to 270 °C

3. Supply of indium with 0.4, 0.8, and 1.6 ML at 0.2 ML/s (without As_4 flux). This step enables the formation of indium droplets.

4. Supply of an As_4 flux with 3×10^{-5} Torr at 270 °C. This step enables the crystallization of indium droplets to InAs QDs.

5. Annealing at 370 °C for 5 min under As_4 supply

6. Capping with a 75 nm $In_{0.52}Al_{0.48}As$ layer at 370 °C

7. Annealing at 470 °C for 5 min

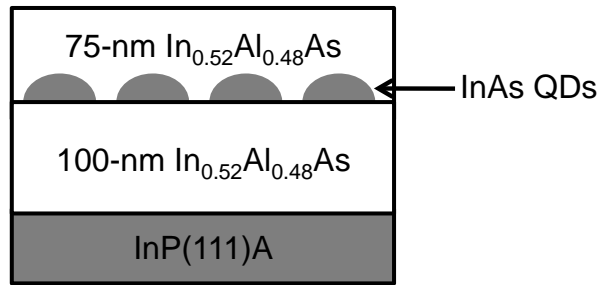**Fig. 3.1 Sample structure of InAs QDs in In$_{0.52}$Al$_{0.48}$As on InP (111)A.**

Reflection high-energy electron diffraction (RHEED) was measured during growth. Atomic force microscopy (AFM) was used to characterize the surface morphologies of uncapped QDs. Dark-field cross-sectional transmission electron microscopy (TEM) was used to study the structural properties of capped QDs.

Surface analysis during growth: Figure 3.2 shows the RHEED pattern during the growth of the 0.4 and 0.8 ML indium samples. After the growth of an InAlAs layer, a streak pattern is observed in the orthogonal [1-10] and [11-2] azimuths. This indicates the formation of a flat surface with (2×2) reconstruction on (111)A [110], [111]. After the supply of indium without As$_4$ flux, the streak pattern changes to the halo pattern. This indicates the formation of liquid indium droplets. After the supply of As$_4$, the halo pattern changes to spotty. This indicates the crystallization of indium droplets into InAs QDs.

The RHEED pattern of the 0.4 ML sample becomes different from that of the 0.8 ML sample after annealing at 370 °C for 5 min under As$_4$ supply. For the 0.4 ML indium sample (Fig. 3.2(a)), the streak pattern appears after annealing. This result suggests that a flat surface emerges, and QDs disappear. For the 0.8 ML indium samples (Fig. 3.2(b)), the spotty pattern is completely maintained. The RHEED patterns of the 1.6 ML sample are the same with those of the 0.8 ML sample.
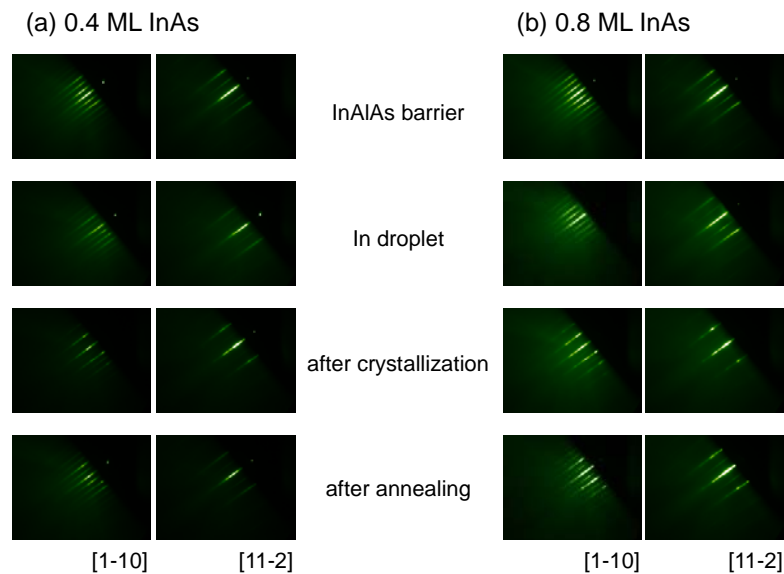

Fig. 3.2 RHEED pattern during the growth of (a) 0.4 ML and (b) 0.8 ML indium samples.

3.3 Morphology analysis

Dependence on the supply of indium: Figure 3.3 shows the AFM image of the sample grown with the indium supply of (a) 0.4, (b) 0.8, and (c) 1.6 ML after crystallization at 270 °C. The images reveal well-defined QDs with the density of (a) 6.6×10^{10}, (b) 1.1×10^{11}, and (c) 5.4×10^{10} cm^{-2}, and the average diameter (height) of (a) 17 (0.7), (b) 18 (0.8), and (c) 30 (1.6) nm.

Notably, QDs were formed even when the indium supply was less than 1 ML, suggesting that droplet nucleation occurred immediately after supplying indium on the surface (without a forming two-dimensional layer). The immediate nucleation of droplets is likely facilitated by the absence of excess arsenic atoms on the (111)A-(2×2) surface, as has been reported for GaAs surfaces [95].

We plotted the dependence of the density and the diameter of QDs on the amount of indium in Fig. 3.4. With increasing the amount of indium from 0.4 to 0.8 ML, the density increases from 6.6×10^{10} to 1.1×10^{11} cm^{-2}, but the diameter increases only slightly from 17 to 18 nm. By a further increase in the amount of indium to 1.6 ML, the density strongly decreases, and the diameter increases. These suggest that, with supplying indium, the nucleation of droplets starts and continues till the indium amount reaches 0.8 ML, and the coalescence and/or ripening of small droplets occurs afterwards.
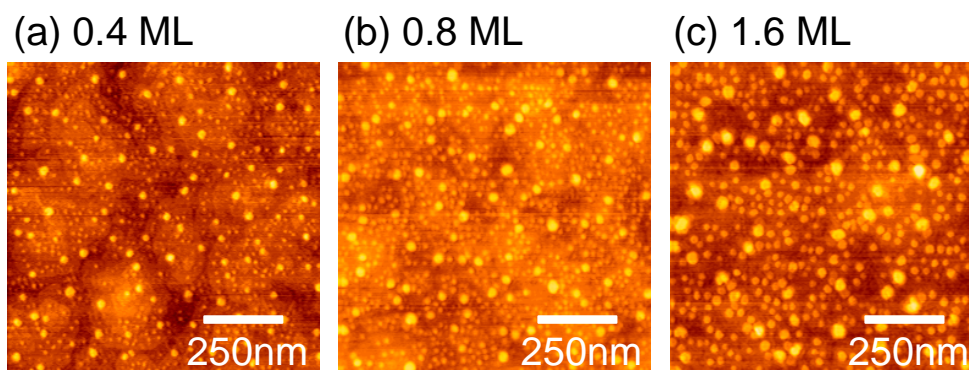

Fig. 3.3   AFM image of the sample grown with the indium supply of (a) 0.4, (b) 0.8, and (c) 1.6 ML after crystallization at 270 °C.
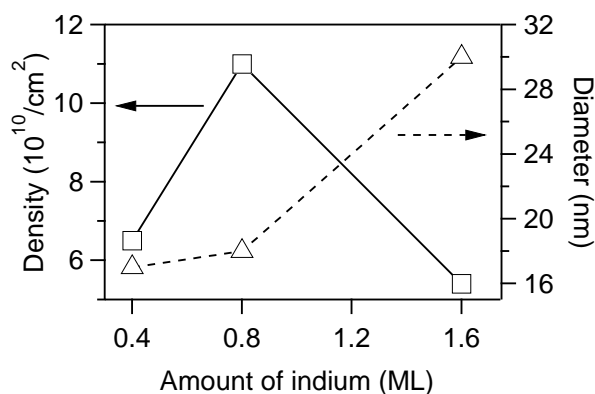

Fig. 3.4   Dependence of the density and the diameter of QDs on the amount of indium.

Impact of annealing: Figures 3.5(a, b, and c) show the evolution of surfaces with annealing at 370 °C for 5 min for samples with 0.4, 0.8, and 1.6 ML indium, respectively. For the 0.4 ML indium sample, the most of QDs disappear after annealing. The result is consistent with the RHEED observation in Fig. 3.2. On the other hand, for the 0.8 and 1.6 ML indium samples, QDs are visible even after annealing. For the 0.8 ML indium sample, the QD density decreases from 1.1×10^{11} to 8.8×10^{9} cm^{-2}. In contrast, for the 1.6 ML indium sample, the density is almost unchanged.
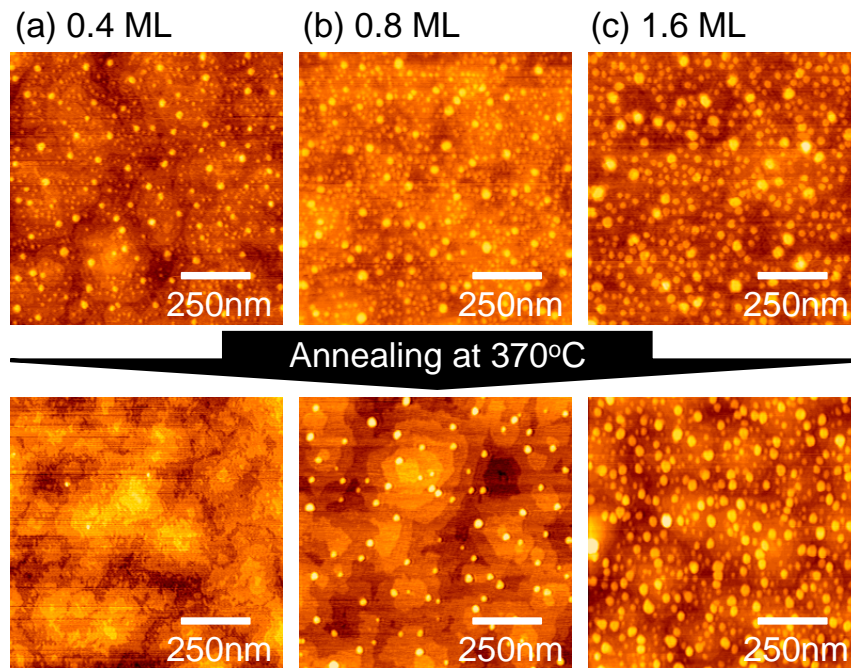
Fig. 3.5 Comparison between the samples before annealing and those after annealing at 370 °C for 5 min for samples with 0.4, 0.8 and 1.6 ML.
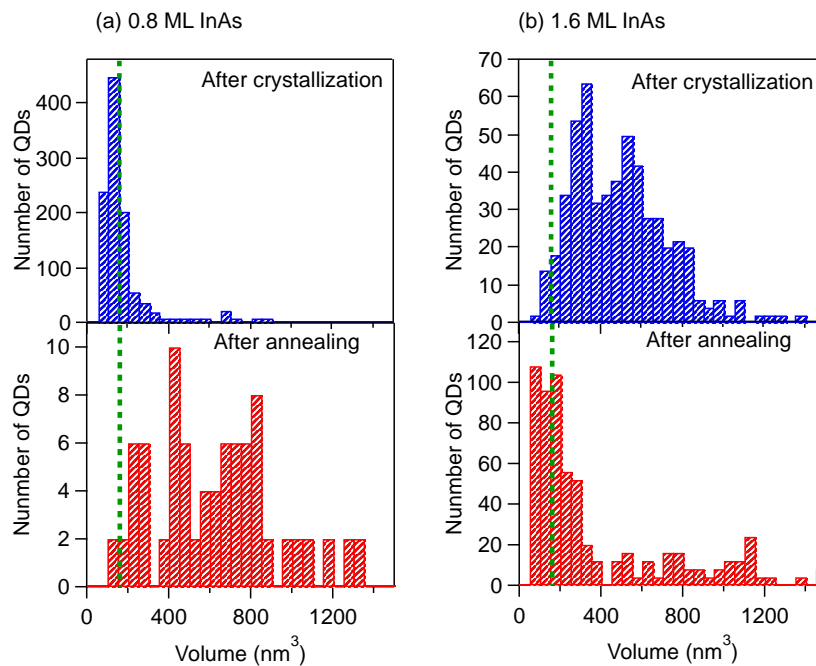
Fig. 3.6 Statistics of size distribution after crystallization (before annealing) and after annealing at 370 °C for (a) 0.8 ML and (b) 1.6 ML sample.

The impact of annealing on the surface morphology is further depicted in the size distribution of QDs in Fig. 3.6. Here, we analyzed the QD volume with the assumption that each QD had a hemispherical shape for simplicity. For the 0.8 ML indium sample (upper panel in Fig. 3.6(a)), more than 80% of QDs exhibit a volume lower 150 nm^3 (indicated by the broken line) after crystallization (before annealing). However, such small QDs mostly disappear in the sample after annealing, which leads to the observation of a decrease in the QD density (lower panel in Fig. 3.6(a)). In contrast, for the 1.6 ML indium sample (upper panel in Fig. 3.6(b)), the number of such small QDs is low. Thus, the QD density is almost unchanged after annealing (lower panel in Fig. 3.6(b)). The QD volume is distributed around an average value of 740 nm^3 before annealing, but it drastically decreases to 350 nm^3.

Thus, for all samples, annealing causes a significant reduction in volume. For the 0.8 ML indium sample, this volume reduction resulted in the density reduction since most of QDs already had a low volume even before annealing.

Dependence on the annealing time: Figure 3.7 shows the AFM image of the 0.8 ML indium sample after annealing at 370 °C for (a) 5 min and (b) 10 min. The QD density is 8.8×10^9 cm^{-2} in both samples. Moreover, the morphology of QDs is nearly the same. These results suggest that the diffusion of atoms from InAs QDs stops after some extent flows out. Thus, the QD morphology is independent of annealing time at the annealing temperature of 370 °C.

Dependence on the annealing temperature: Figure 3.8 shows the AFM image of the 0.8 ML indium sample after annealing at (a) 270, (b) 320, (c) 370, (d) 420, and (e) 470 °C for 5 min. It is found that the QD density significantly decreases with increasing annealing temperature. Moreover, the QDs almost disappear after annealing at 470 °C. Note that indium re-evaporation can hardly occur at these temperatures.
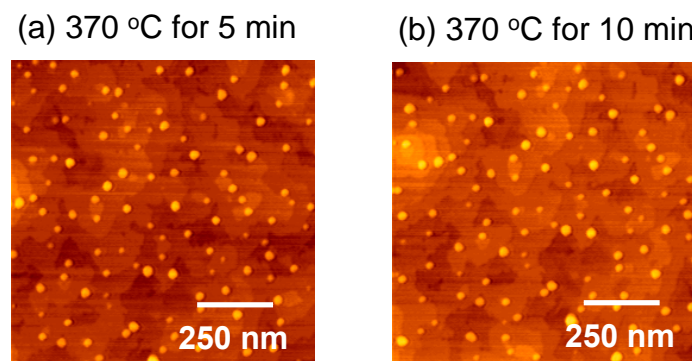
(a) 370 °C for 5 min   (b) 370 °C for 10 min

Fig. 3.7   AFM images of a surface on the 0.8 ML indium sample after annealing at 370 °C for (a) 5 min and (b) 10 min.

Dependence on the dot size: We study the dependence of the annealing effect on the QD size. We prepared for this purpose two samples with different sizes by controlling temperature when we supplied indium that formed droplets.

Figure 3.9 shows the AFM image of samples with the droplet formation temperature of (a) 270, and (b) 320 °C. For both samples, we supplied 0.4 ML of indium. Note that the QDs of Fig. 3.9(a) are the same with those of Fig. 3.3 (a) and 3.5 (a).

We found that, before annealing (top panels), the QD size of Fig. 3.9(b) was significantly larger than that of Fig. 3.9(a). After annealing (bottom panels), the most QDs disappear in Fig. 3.9(a), as was described previously. On the other hand, significant numbers of QDs remain in Fig. 3.9(b), though the size becomes smaller. This observation implies a limited atomic flow from QDs to a two-dimensional layer.
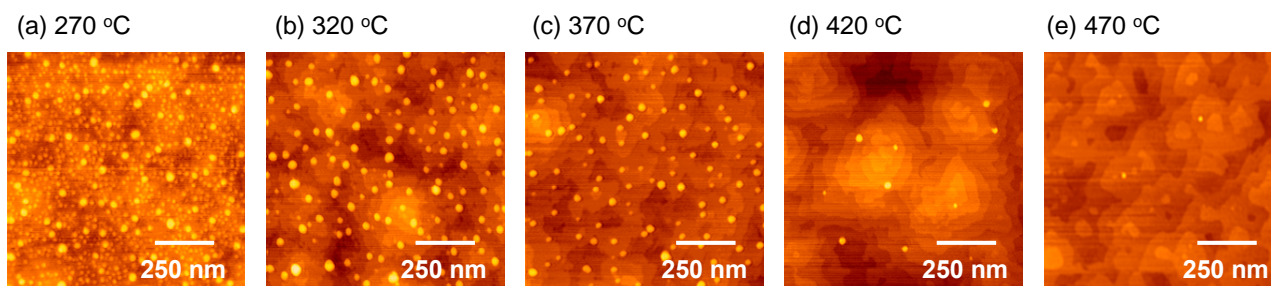

(a) 270 °C   (b) 320 °C   (c) 370 °C   (d) 420 °C   (e) 470 °C

250 nm   250 nm   250 nm   250 nm   250 nm

Fig. 3.8   AFM images of a surface on the 0.8 ML indium sample after annealing for 5 min at (a) 270, (b) 320, (c) 370, (d) 420, and (e) 470 °C.

(a) Small QD sample   (b) Large QD sample

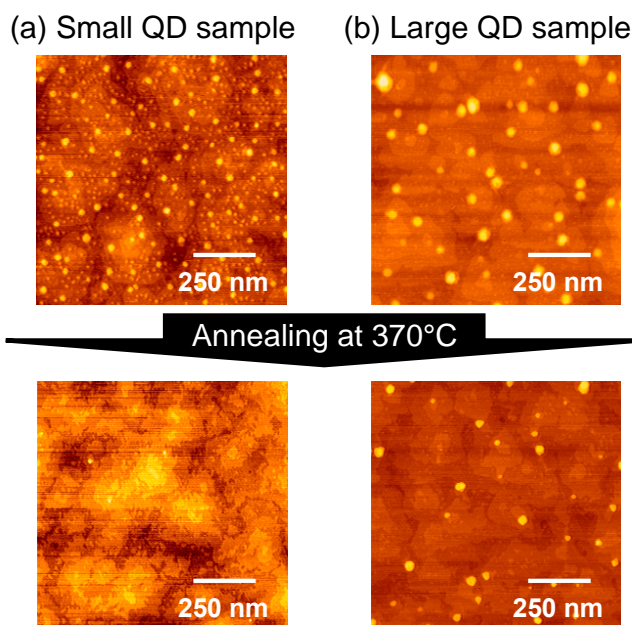250 nm   250 nm

Annealing at 370°C

250 nm   250 nm

Fig. 3.9   AFM image of samples with droplet formation temperature of (a) 270 °C, and (b) 320 °C, and with 0.4 ML of indium for both samples.

Formation of a two-dimensional layer by annealing: Figure 3.10 shows schematics for the formation mechanism of a two-dimensional layer. In the case of droplet epitaxy, QDs are grown by a kinetically limited process without forming a two-dimensional layer. At annealing step, however, some amount of InAs atoms flows out from QDs and forms a two-dimensional layer, which might reduce the local strain energy in the vicinity of QDs. As the results, small QDs turn a two-dimensional layer, and large QDs turn smaller QDs with a two-dimensional layer. The emergence of a two-dimensional layer following the QD formation is in the reverse order of S-K growth, for which a two-dimensional layer (i.e., a wetting layer) appears before QDs [51], [71], [74], [112].

TEM analysis on capped quantum dots: Figure 3.11 shows the cross-sectional TEM image of the 1.6 ML QDs embedded in the InAlAs barrier. The buried QD shows a truncated disk-like shape with an atomically smoothed surface on the top. No dislocation was found at the interface between the QD and the InAlAs barrier, indicating the high crystalline quality of the present samples. The clear contrast between the QD and the InAlAs barrier proves the formation of abrupt interface. The formation of disk-like QDs with flat-top surfaces has been also observed on droplet epitaxial GaAs QDs formed on an AlGaAs (111)A surface [93]. A two-dimensional layer with a thickness around 1 ML is clearly visible, as indicated with an arrow.
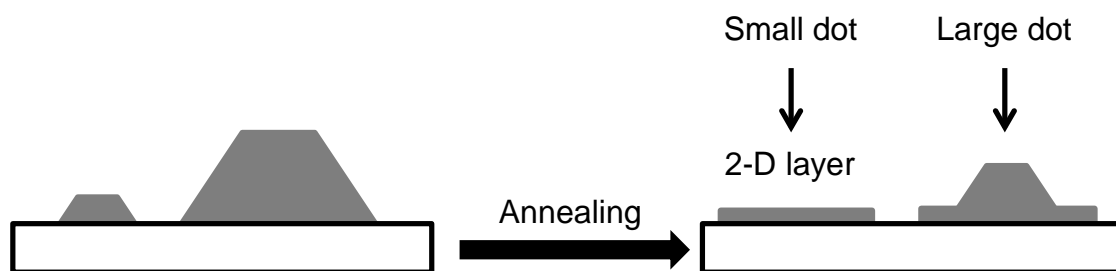

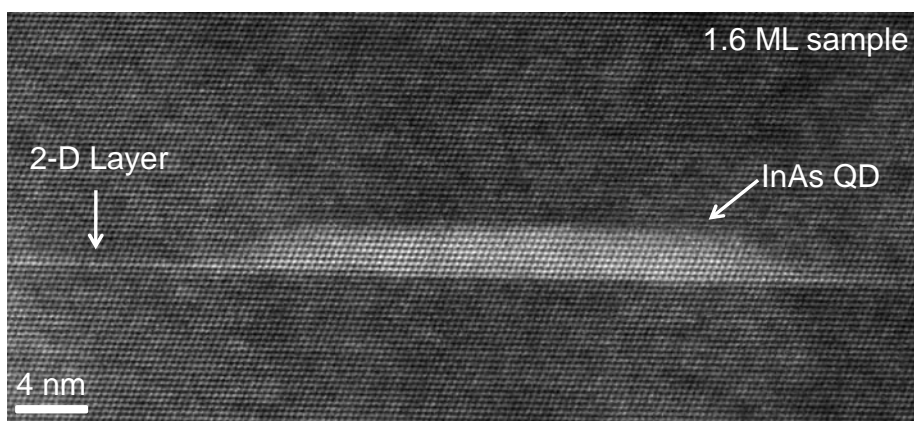**Fig. 3.10   Schematics for the formation mechanism of two-dimensional layer.**

Fig. 3.11   Cross-sectional TEM image of the 1.6 ML QDs embedded in the InAlAs barrier.

Shape distribution: Figure 3.12(a) shows the three-dimensional view of an AFM image of uncapped InAs QDs grown with 1.6 ML indium. Despite a finite spatial resolution, a flat top shape is clearly visible for relatively large QDs. Figures 3.12(b, and c) show typical cross-sectional profiles obtained along two orthogonal directions ([-211] and [01-1]) for a small QD and a large QD, respectively. For both QDs, the profiles along two directions are nearly identical. This isotropic feature is a direct consequence of the three-fold rotational symmetry of the (111)A surface, on which equivalent directions appear with respect to every 120 degree rotation. As a consequence of this symmetry, in-plane anisotropy is eliminated in QDs.

Figure 3.13 shows the statistics of the height and the diameter for 0.8 and 1.6 ML QDs. The linear dependence of the height on the lateral size indicates that the same aspect ratio (height/lateral size) in all the QDs.
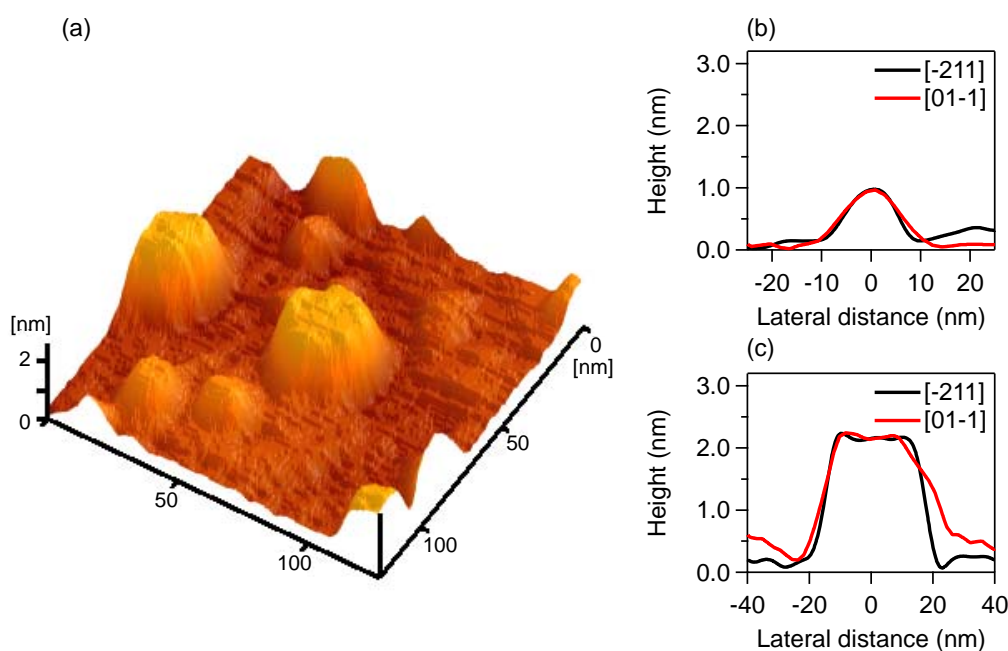

Fig. 3.12 (a) Three-dimensional view of an AFM image of uncapped InAs QDs grown with 1.6 ML indium. (b, and c) Typical cross-sectional profiles obtained along two orthogonal directions ([-211] and [01-1]) of a small and a large QD, respectively.
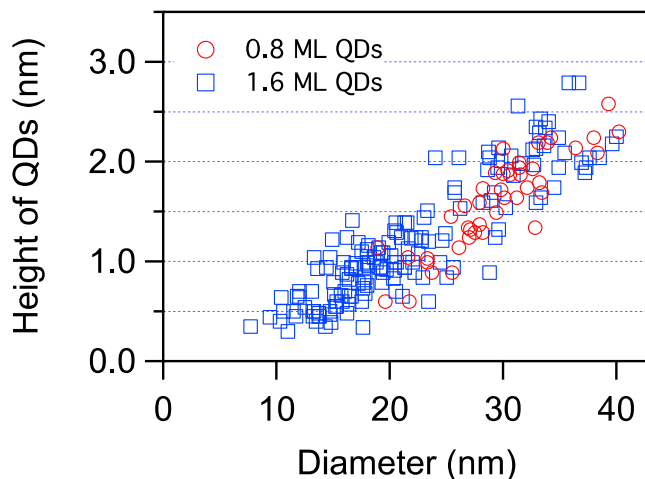

Fig. 3.13 Statistics of the height and the diameter for 0.8 and 1.6 ML QDs.

Artificial deposition of a wetting layer: We observed that InAs QDs disappear with forming a two-dimensional layer. Since the shape and density of QDs are directly related with device properties, their control techniques are important. In this section, we present the formation and control of a wetting layer before the growth of InAs QDs in order to prevent the morphology change of InAs QDs.

Growth: The schematic of sample structure is shown in Fig. 3.14. We carried out the following growth sequence:

0. Installation of semi-insulating (Fe-doped) InP(111)A as a substrate

1. Growth of a 50 nm $In_{0.52}Al_{0.48}As$ layer (lattice-matched to InP) at 470 °C

2. Growth of a 1 ML (0.35 nm) InAs wetting layer at 470 °C

3. Cool down the substrate to 270 °C

4. Supply of indium with 0.4 and 0.8 ML at 0.2 ML/s (without As_4 flux).

5. Supply of an As_4 flux with 3×10^{-5} Torr at 270 °C.

6. Annealing at 370 °C for 5 min under As_4 supply

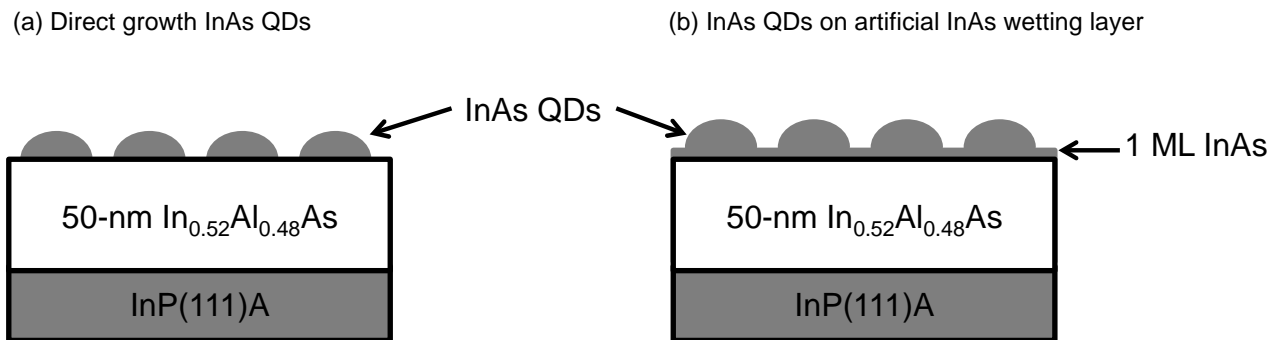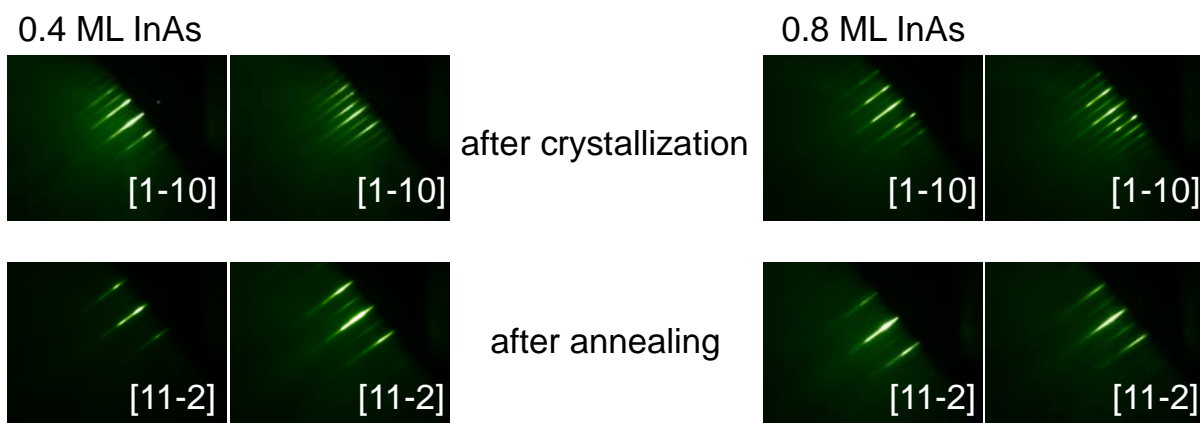(a) Direct growth InAs QDs   (b) InAs QDs on artificial InAs wetting layer

Fig. 3.14   Sample structure of (a) direct growth InAs QDs on InAlAs, and (b) InAs QDs on an artificial InAs wetting layer.

Surface analysis during growth: Figure 3.15 shows the RHEED pattern before and annealing with (a) a direct growth of 0.4 and 0.8 InAs QDs on InAlAs, and with (b) an artificial InAs wetting layer growth of 0.4 and 0.8 InAs QDs on 1-ML InAs/InAlAs, respectively. For the direct growth samples with 0.4 and 0.8 ML InAs QDs, the spotty patterns are observed, which is same with the previous results, shown in Fig. 3.2 (a). While the spotty is maintained in the 0.8 ML InAs QDs sample after annealing, the pattern changes from spotty to streak in the 0.4 ML InAs QDs sample. Also, in both samples with 1-ML InAs wetting layer, the spotty patterns are observed before annealing, resulting in the formation of QDs. After annealing, the spotty pattern is obviously maintained not only in the 0.8 ML InAs QDs sample but also in 0.4 ML InAs QDs sample. This result implies the presence of QDs.

(a) Direct growth InAs QDs

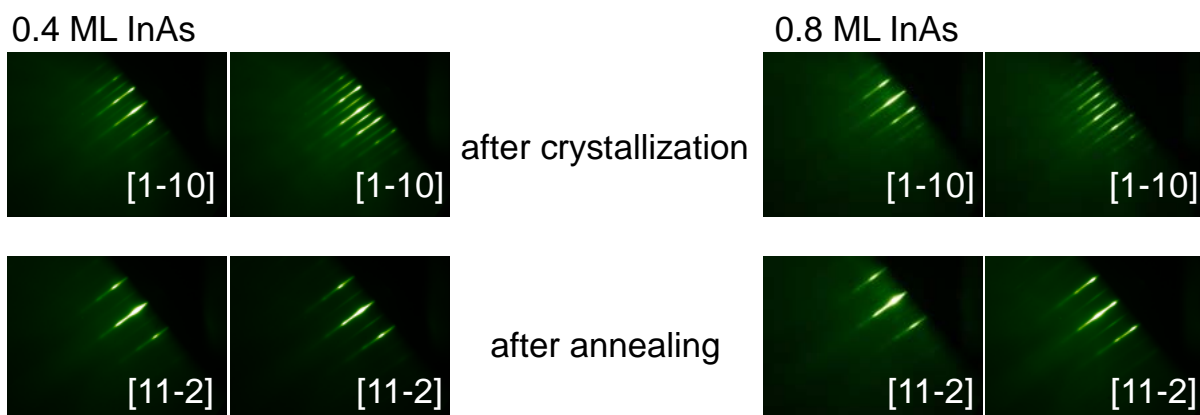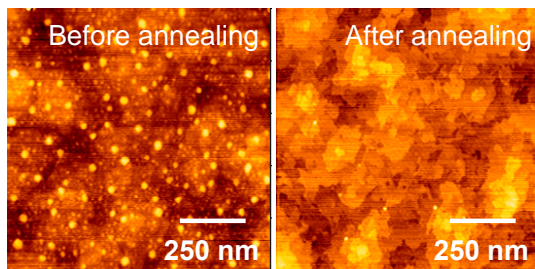## (b) InAs QDs on artificial InAs wetting layer

Fig. 3.15   RHEED pattern before and annealing with (a) a direct growth of 0.4 and 0.8 InAs QDs on InAlAs, and with (b) an artificial InAs wetting layer growth of 0.4 and 0.8 InAs QDs on 1-ML InAs/InAlAs, respectively.

Morphology analysis: Figure 3.16 shows the AFM images of the samples with 0.4 and 0.8 ML InAs QDs on (a) InAlAs (direct growth), and on (b) an artificial 1-ML InAs/InAlAs. Before annealing, for the direct growth samples, well-produced QDs are observed. The density and the average lateral size (height) are 3.6×10^{10} and 4.4×10^{10} cm^{-2} and 28 (1.2) and 24 (0.9) nm, respectively. For the growth of InAs QDs samples with 1-ML InAs layer, the images also indicate well-defined QDs with density of 1.7×10^{10} and 3.6×10^{10} cm^{-2}, and the average lateral size (height) is 35 (1.3) and 30 (1.3) nm, respectively. In comparison with morphology of the direct growth and the growth with 1-ML InAs wetting layer, the QD density is lower on 1-ML InAs than of the direct growth, Thus, the average size is slightly bigger. We consider that the indium droplets have a different mobility on InAlAs and InAs. Therefore, when indium is supplied to the InAs surface, coalescence and/or ripening of the indium droplets easily occurs than that for InAlAs. As a result, the lower density and the bigger QDs are observed in the samples with 1-ML InAs layer.

After annealing at 370 °C for 5 min, for the direct growth sample, the annealing-induced in the morphology changes almost correspond with previous results. In the case of the growth with 1-ML InAs wetting layer, a different change in morphology are observed by annealing. For the 0.8 ML InAs QDs sample, the most of small QDs disappear after annealing, however, the QDs size seems to be larger than that for before annealing with decreasing QD density to 1.2×10^{10} cm^{-2}. Besides, for the 0.4 ML InAs QDs sample, a drastic changes of the QD density does not occur, in which reducing to 8.3×10^{9} cm^{-2}.
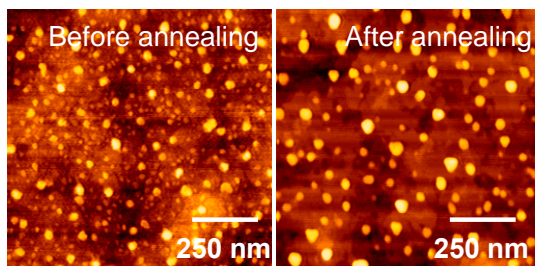
(a) Direct growth InAs QDs

0.4 ML InAs

0.8 ML InAs
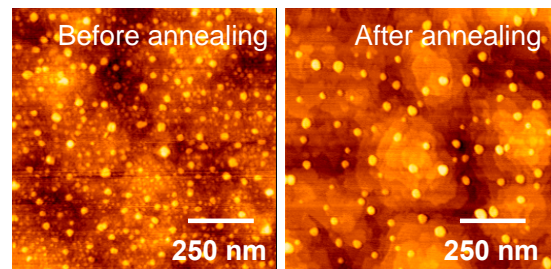
(b) InAs QDs on artificial InAs wetting layer
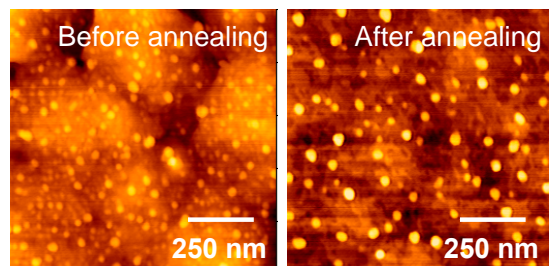
0.4 ML InAs

0.8 ML InAs

Fig. 3.16   AFM images of the samples with 0.4 and 0.8 ML InAs QDs on (a) InAlAs (direct growth), and on (b) an artificial 1 ML InAs/InAlAs, respectively.

Figure 3.17 shows the histogram for size distribution of 0.4 and 0.8 ML InAs QDs on (a) InAlAs and (b) 1-ML InAs wetting layer before and after annealing. While the small QDs disappear after annealing as shown in Fig. 3.17(a), in the case of the present QDs (Fig. 3.17(b)), the QD size becomes bigger than that before annealing. The density is slightly reduced, but is not significant. Form this result, we consider that the annealing might not be induce to the formation of two-dimensional layer form the InAs QDs on 1-ML InAs wetting layer. It might reveal that the small QDs migrate to neighbor QDs. The impotence is that the QDs remain after annealing, it implies that the morphology of QDs can be controlled by droplet epitaxy even in the lattice-mismatched systems.
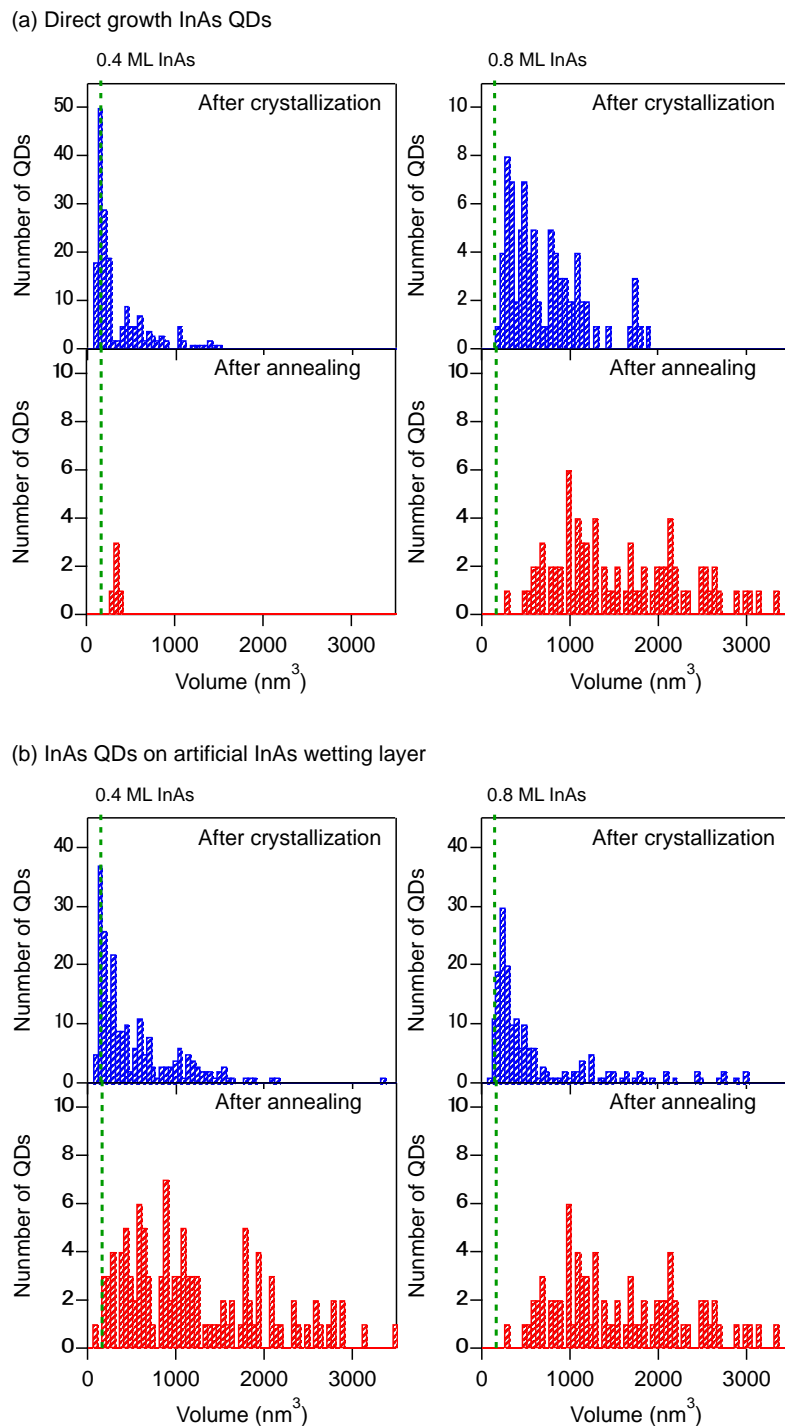

Fig. 3.17   Histogram for size distribution of 0.4 and 0.8 ML InAs QDs on (a) InAlAs and (b) 1-ML InAs wetting layer before and after annealing.

3.4   Optical properties

Ensemble measurement: Photoluminescence (PL) spectra were taken at 9 K, using the 532 nm line of a frequency doubled Nd:YAG laser. The PL signals were dispersed by a polychromator and detected by a cooled InGaAs photodiode array for wavelengths from 900 nm to 1.6 μm or a Si charge-coupled device camera for visible wavelengths from 500 to 950 nm. Signals at further long wavelengths are detected by a PbS detector that has a response < 2.5 μm.

Figure 3.18 shows the PL spectra of ensembles of QDs depending on excitation laser power measured at 9 K. Strong QD emissions were observed in both samples at a wide spectral range of 950-1600 nm, which covers the O (λ ~ 1310 nm), C (λ ~ 1550 nm), and L (λ ~ 1600 nm) telecommunication bands. This broad-band emission is consistent with a large size distribution of QDs observed by AFM. The PL spectrum consists of multiple peaks, rather than a broad single peak. The relative intensity between the multiple peaks was independent of excitation power. Thus, the observed spectral multiplet is ascribed to different families of QDs whose height vary by a monolayer step (0.350 nm). The split multiple peaks indicate that the QDs have a truncated shape with a flat top.
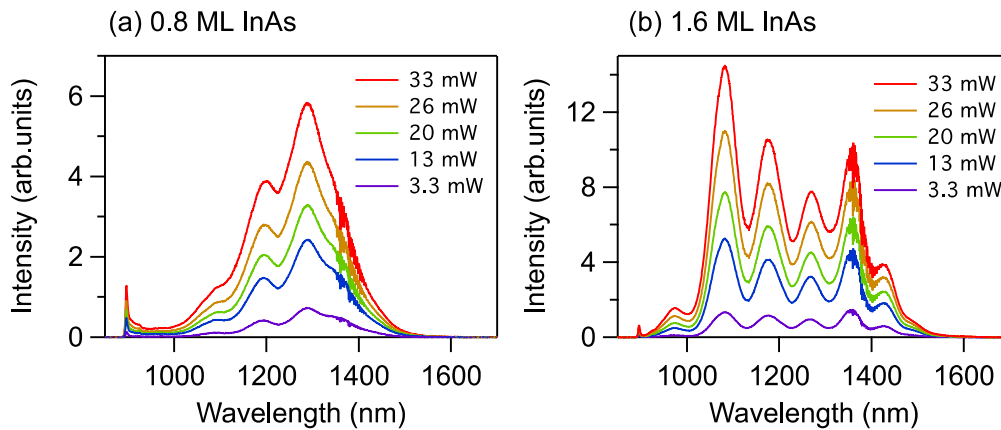

Fig. 3.18   PL spectra of QDs prepared with (a) 0.8, and (b) 1.6 ML indium at 9K. They are detected by a cooled InGaAs photodiode array whose wavelength response spans between 900 nm and 1.6 μm.
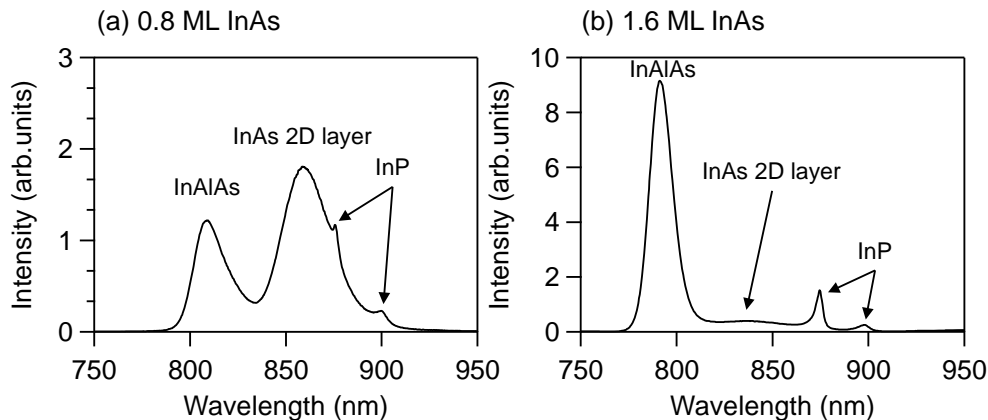

Fig. 3.19   PL spectra of QDs prepared with (a) 0.8 and (b) 1.6 ML indium at 9K. They are detected by a Si charge coupled device camera whose wavelength response spans between 500 and 950 nm.

Figure 3.19 shows the PL spectra of QDs prepared with 0.8 and 1.6 ML indium for a visible wavelength range between 750 and 950 nm. Emission from the two-dimensional layer was observed around 840 nm, together with emissions from the InP substrate at 875 and 900 nm and the InAlAs barrier at ~ 800nm. The two-dimensional layer signal is relatively higher for the 0.8 ML sample than for the 1.6 ML sample due to a difference in the QD density, as shown in Fig 3.3.

Energy level calculation: We have calculated the transition energies of InAs QDs embedded in an $In_{0.52}Al_{0.48}As$ barrier in the framework of the effective mass model [78]. In this calculation, we introduce the following assumption:

- *QD shape:* Each QD has a shape of a truncated cone with an underlying disk with a thickness of 1 ML (0.350 nm). Figure 3.20 shows a model shape that is parameterized by a diameter (D) and a height (h). We assume that QDs have a fixed aspect ratio independent of size, and h/D = 0.14, which is determined by the AFM statistics (Fig. 3.13). The QD height is discretized with a step of a monolayer along [111], which is 0.350 nm for $In_{0.52}Al_{0.48}As$. Note that the lattice constant of $In_{0.52}Al_{0.48}As$ is the same with that of InP.

- *Effect of strain:* The effect of strain on the QD energy is taken into account by an energy shift in the fundamental band gap of QD interior from 0.41 eV (unstrained InAs) 0.48 eV (biaxially compressed InAs with a train of 3.4%) [113]. The band gap of the $In_{0.52}Al_{0.48}As$ barrier is set to 1.51 eV [114].

- *Band offset:* There is no existing work which measures the conduction (valence) band offset (ΔEc (ΔEv)) between InAs and $In_{0.52}Al_{0.48}As$ at the {111} interface. Thus, we have varied the band offset ratio, ΔEc:ΔEv = 4:6 (ΔEc = 0.416 and ΔEv = 0.624 eV), 5:5 (ΔEc = 0.52 and ΔEv = 0.52 eV), 6:4 (ΔEc = 0.624 and ΔEv = 0.416 eV), 7:3(ΔEc = 0.728 and ΔEv = 0.312 eV), until we reach agreement between calculated energies and measured spectra. The best agreement is found when ΔEc:ΔEv = 7:3 (ΔEc = 0.728 and ΔEv = 0.312 eV).
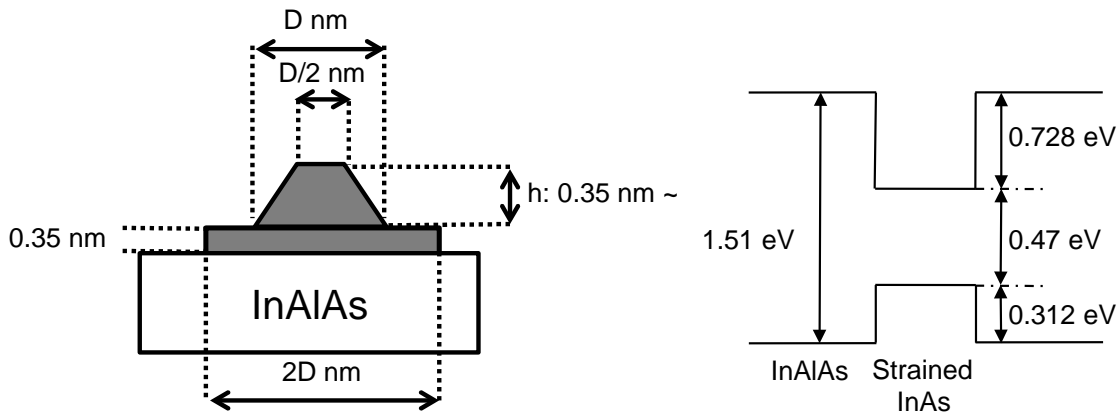

Fig. 3.20   Parameter for calculation of QD transition energy.

- *Effective mass:* In order to take into account the conduction-valence band mixing due to strong quantum confinement, we have treated the electron effective mass (m_e) as a free parameter that changes between the bulk InAs value of 0.0265 m_0 and the bulk $In_{0.52}Al_{0.48}As$ value of 0.0839 m_0, where m_0 is the free electron mass. The best agreement is found when m_e = 0.0397 m_0. The heavy hole effective mass is fixed to the bulk value of 0.35 m_0, since its influence on the transition energy is small.

We numerically solved Schödinger equation using COMSOL, a commercial software for three dimensional finite-element calculation.

Figure 3.21 shows a comparison between calculated transition energies and PL spectra in the 1.6 ML sample. Each vertical line shows the lowest confinement level of QDs with a different monolayer height. We find that this model perfectly reproduces the spectral multiplets. The highest peak is attributed to emission from QDs with 4 ML height, and 1.3 and 1.55 μm wavelength emission is from QDs with 6-ML and 9-ML height, respectively.

Yo-Nian Wu and Shun-Jen Cheng in the National Chiao Tung University, Taiwan, have performed more precise simulation based on the 4 band **k.p** model without any adjustable parameters [118]. Their result also predicts that the highest peak in PL spectra originates from QDs with a height of 4 ML, which is consistent with our analysis.
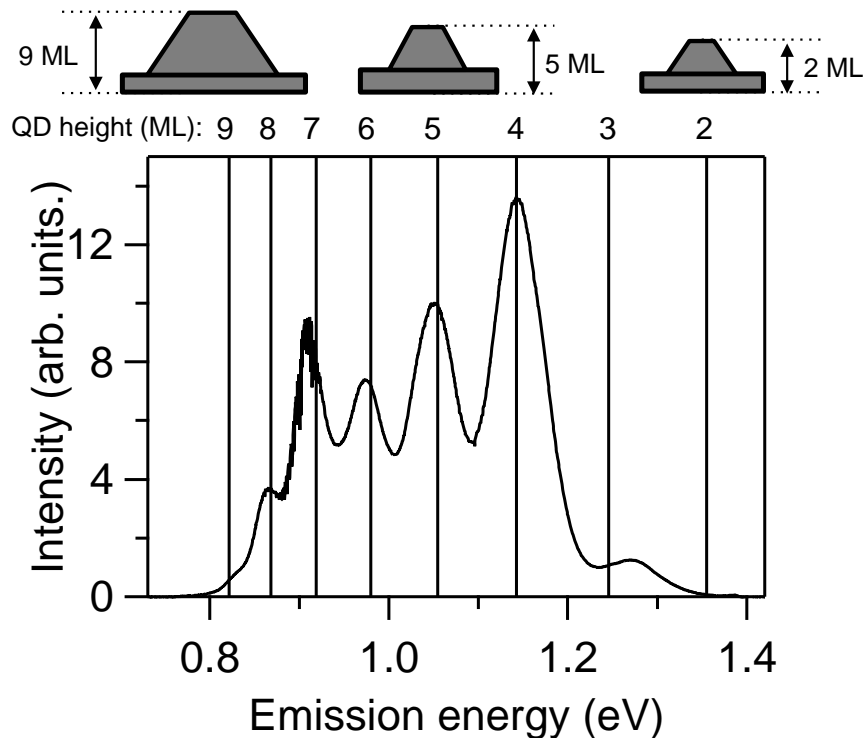

Fig. 3.21 Comparison between calculated transition energies and the PL spectra of 1.6 ML sample. Each vertical line shows the lowest confinement level of QDs with a different monolayer height.

Temperature dependence: Figure 3.22 shows the PL spectra of QDs as a function of temperature. With increasing temperature, the multiple peaks shift to longer wavelengths in unison. At the same time, the intensity decreases, although the signal remains even at 300 K. The intensity at 300 K is 1/10 of that observed at 9 K.

We will analyze three peaks denoted by P1, P2, and P3 in Fig. 3.22(b). They originate from QDs with a height of 4, 5, and 7 ML, respectively. We perform Gaussian fitting to each peak to evaluate the intensity for different temperatures. Figure 3.23 shows PL intensities as a function of inverse temperature. The solid lines are results from the best fit to the experimental data by the Arrhenius-type equation [109], [115].

$$I(T) = \frac{I_0}{1 + A_1 exp\left(-\frac{E_1}{kT}\right) + A_2 exp\left(-\frac{E_2}{kT}\right)}, \tag{3.1}$$

where I_0 is the integrated PL intensity at 0 K, E_1 and E_2 are the two thermal activation energies, A_1 and A_2 are the corresponding dimensionless coefficients, k is the Boltzmann constant, and T is the sample temperature.
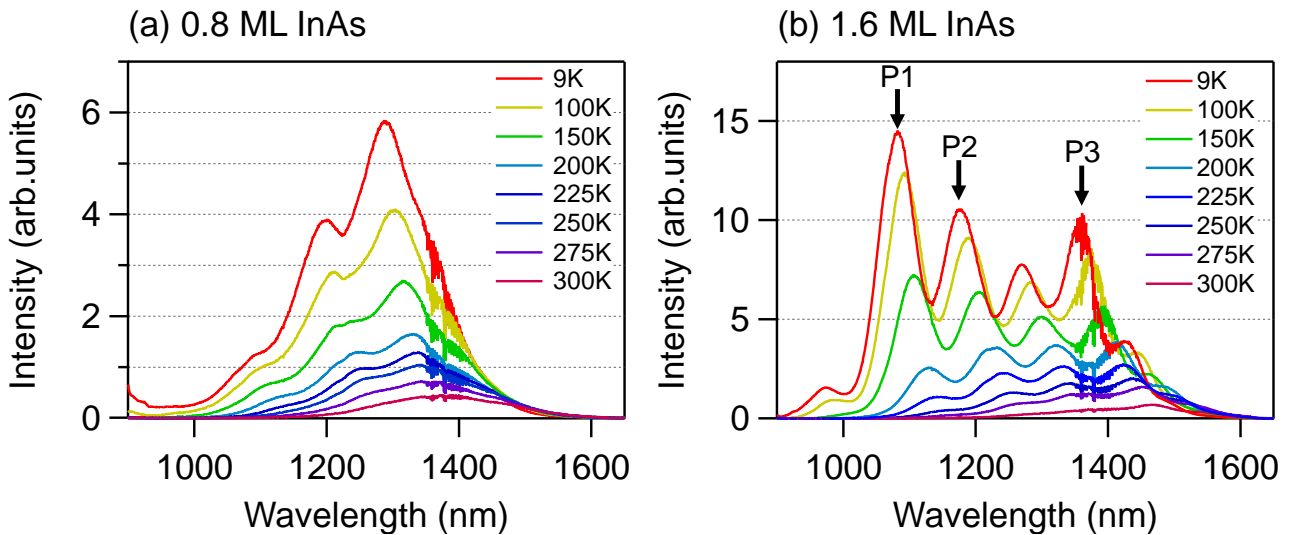

Fig. 3.22   PL spectra of ensembles of QDs as a function of temperature.

TABLE 3.1 Activation energies and fitting coefficients.

	$E_1 (meV)$	$E_2 (meV)$	A_1	A_2
P1	161	37	3.1×10^4	1.3×10^1
P2	321	37	2.0×10^7	1.2×10^1
P3	478	35	3.9×10^8	1.6×10^1

Table 3.1 summarizes activation energies and fitting coefficients. The fitting coefficients A_1 and A_2 are defined simply as the ratio of carrier capture time and carrier escape time of QDs by respective nonradiative process [115], [116]. For all experimental results, the values of A_1 are significantly larger than those of A_2. Thus, A_1 contributes to preponderant role in thermally activated charge carrier escape process, while A_2 plays a minor role. The activation energy E_1 and E_2 are related to the carrier escape from the QDs and nonradiative scattering in the barrier respectively. The value of E_1 depends on the sample with different QD size, but E_2 is independent of QD size.

Thus, we can infer that the value of E_1 increases with QD size. The results suggest that carriers in smaller QDs more easily escape from QD than those in larger QDs. In addition to this, for the larger QDs, carriers are survived. This result suggests that the carriers are strongly confined in this QD system.
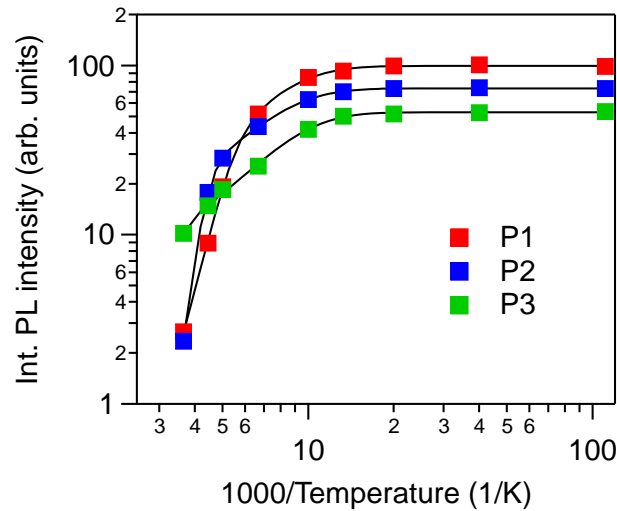

Fig. 3.23 Integrated PL intensities of QDs indicated by the arrows in Fig 3.18(b) as function of inverse temperature. The fit curves (black solid lines) were plotted by Eq. (3.1).

Single quantum dot measurement: In this section, we studied optical properties of single QDs. We used the 0.4 ML indium sample with the QD density of 2.6×10^9 cm^{-2}. The surface morphology of this sample is shown in Fig 3.9(b).

For the PL measurement we used a continuous wave laser emitting at a wavelength of 705 nm for excitation above the barrier band gap. The laser light was focused on the sample using a near-infrared microscope objective with a numerical aperture of 0.65. To reduce the spot size, a hemispherical solid immersion lens with a refractive index of two was positioned on the sample. In this setup, approximately 20 QDs are in the excitation spot (diameter ~ 0.9 μm). Nevertheless, we can isolate a single QD in spectral domain from a QD ensemble with broad size distribution. Spontaneously emitted photons were collected with the same objective, and then fed into a 50-cm focal length polychromator equipped with an InGaAs array detector. The spectrometer had a resolution of 55 μeV (0.08 nm) with a full width at half maximum (FWHM) at a wavelength of 1.3 μm. The linearly polarized PL spectra were recorded as a function of the polarization angle. With a Gaussian fit to the emission lines, we were able to determine the spectral peak shift with a resolution as high as 4 μeV. All the experiments were performed at 10 K.

Figure 3.24 shows typical PL spectra of single QDs emitting at 1.3 and 1.55 μm. Bright emission from the single QD is observed. Furthermore, four emission lines are clearly visible, and assigned, from the short-wavelength side, as X, X^+, XX, and X^-, where X, XX, and $X^{+(-)}$ refers to exciton, biexciton, and positively (negatively) charged excitons, respectively.
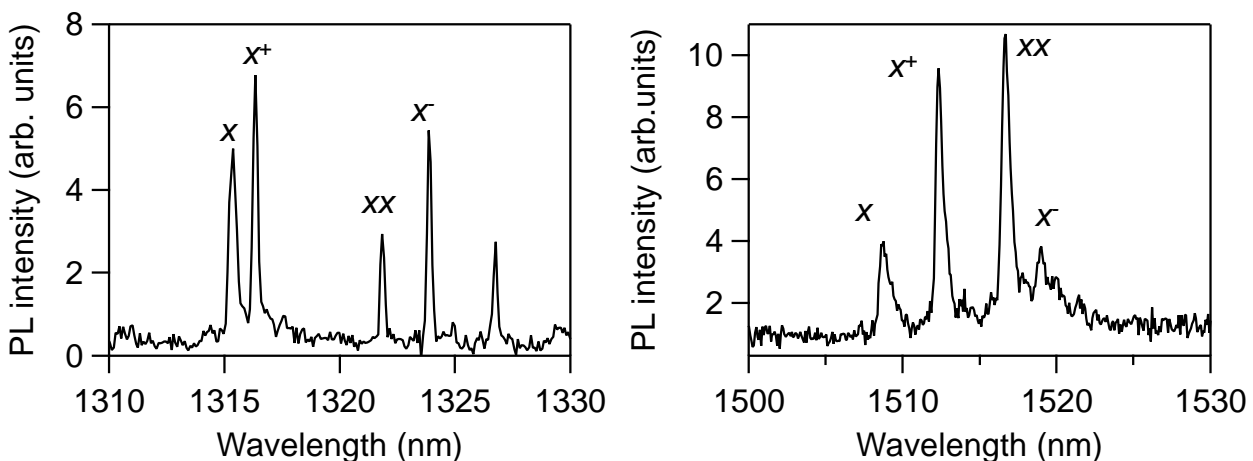

Fig. 3.24   Typical PL spectra of single QDs emitting at 1.3 and 1.55 μm.

Spectral assignment: The *X* and *XX* assignments are based on the measurement of the excitation power dependence of the emission line (Fig. 3.25). For the *X* line, the emission intensity linearly increases with increasing the excitation power. For the *XX* emission line, the emission intensity increases quadratically with increasing the power.

The assignment of X^+ and X^- is further supported by an optical orientation measurement [55]. We analyzed the degree of circular polarization after polarized pumping (Fig. 3.26). In the case of cocircular polarization, where left-handed circular for excitation and left-handed circular for emission (or right-handed circular for excitation and emission), we found that X^+ exhibits a significant positive degree of polarization. In contrast, X^- shows opposite cocircular polarization. These results are due to the carrier relaxation by the electron-hole spin exchanges [117], [118]. The detailed assignment has been discussed in Ref [58]. The observed excitonic features are of importance for application of our QD system to single-photon and entangled photon-pair source.
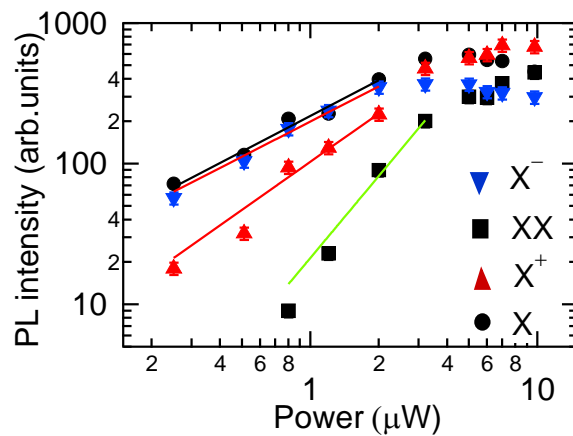

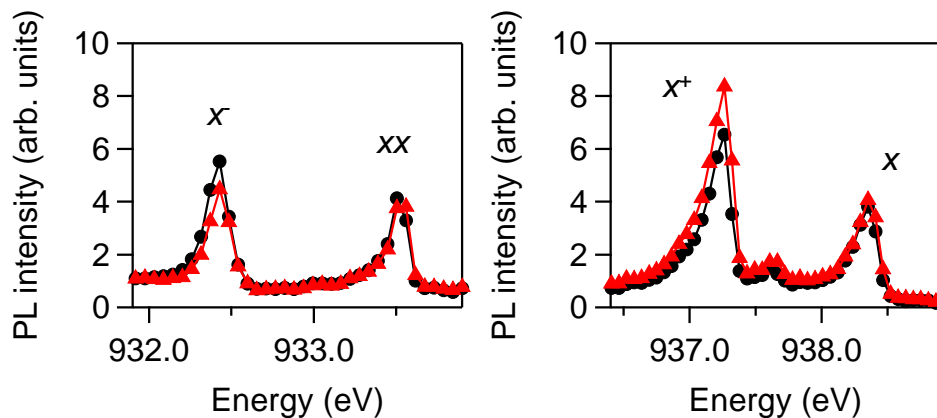**Fig. 3.25   PL intensity as function of excitation power for each exciton complex.**

Fig. 3.26   Circularly polarized PL spectra for $X^{+(-)}$ after circularly polarized excitation.

Figure 3.27 shows a series of PL spectra for QDs with different emission energies (different size of QD). The spectrum is aligned to the X energy, which increases from the top to the bottom panels. Every exciton complex energy implicitly shifts with X emission. Especially, the X^+ line observed at lower energy side of X for large QD appears at the opposite side of X for small QD.

Figure 3.28 shows the binding energy of each exciton complex as a function of X energy. Here the binding energy is defined as the energy difference between X and the exciton complex. It displays that the binding energy of X^- increases with increasing X energy. On the other hand, the binding energy of X^+ decreases. The binding energy of XX has intermediate values between X^- and X^+. Note that the spectral profile of exciton complexes is known to show a sensitive dependence on dot structure [119]. Therefore, the observation of a clear and less dispersive evolution in the binding energy suggests that the shape and other microscopic parameters of dots with a given size are almost identical. This is likely to be due to the kinetically limited formation of dots for droplet epitaxy. Consequently, dots on (111) substrates become rather symmetric as microscopic randomness is effectively suppressed.
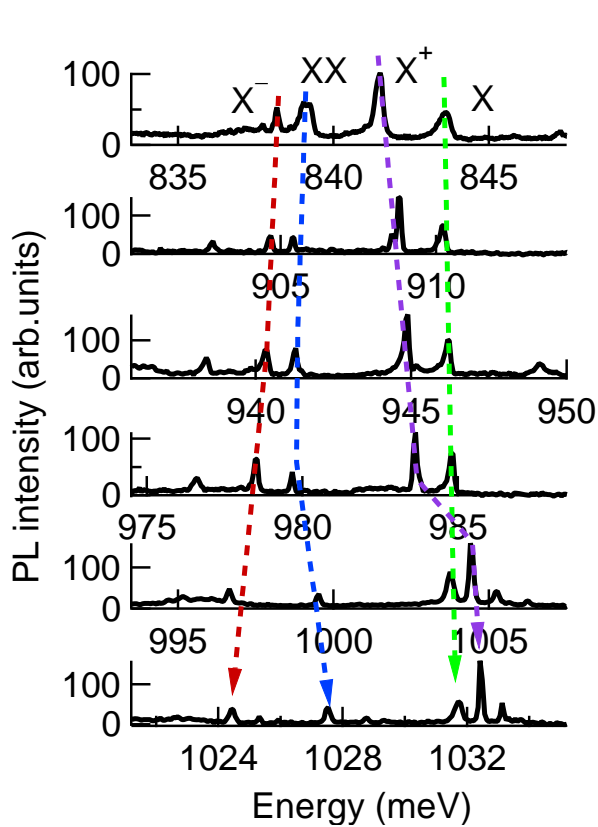

Fig. 3.27   A series of PL spectra for QDs with different emission energies (different size of QD).
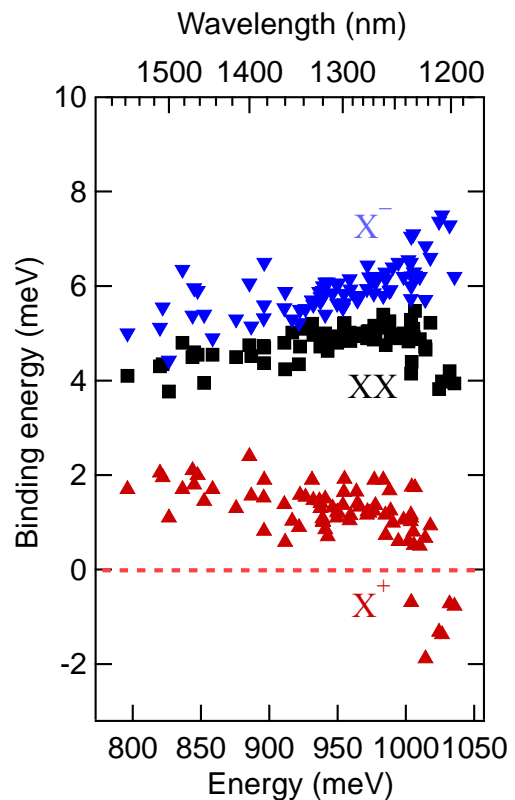

Fig. 3.28   binding energy of each exciton complex as a function of X energy.

Fine-structure analysis: Figures 3.29 shows the evolution of the *X* peak energy when the linear polarization axis is rotated for two dots. The precise quantification of FSS is based on sinusoidal fitting to these evolutions. The magnitude of FSS is described by the amplitude of sine curves, and the polarization axis is defined as the first maximum phase. Thus, the angle of φ corresponds to the polarization axis of the high-energy *X* line among two split lines with orthogonal polarization.

Figure 3.30 shows that the statistical results for FSS over ～50 dots are summarized in Fig. 3.9(b). The FSS magnitude is plotted as a function of *X* energy. The FSS average value is 25 μeV, which is considerably smaller than those of SK QDs in the telecom band [98], [120]. Note that two families of QDs with different monolayer heights are present in Fig. 3.9(b), as shown by the two peaks in the ensemble spectrum (broken line). In the each family divided by the QD height, the FSS decreases with increasing the energy, which results in a smaller in-plane size and higher lateral symmetry. The impact of the lateral-size reduction on FSS minimization was also confirmed in a previous study on FSS control by high-temperature annealing [50].
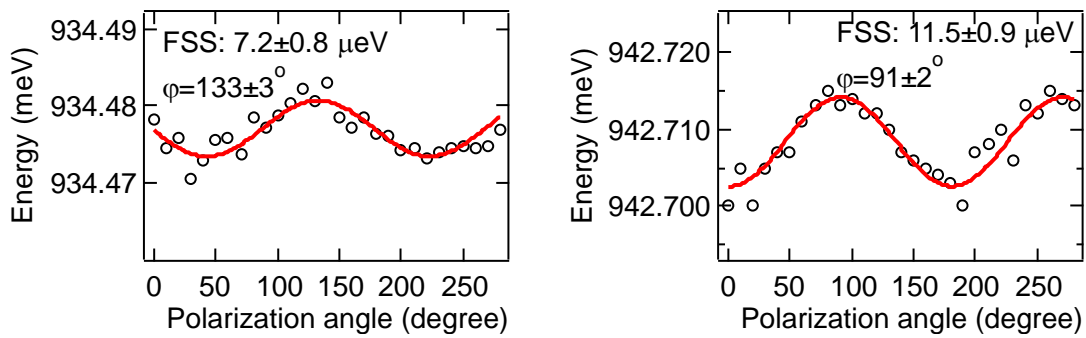

Fig. 3.29   Evolution of the *X* peak energy when the linear polarization axis is rotated for two dots.
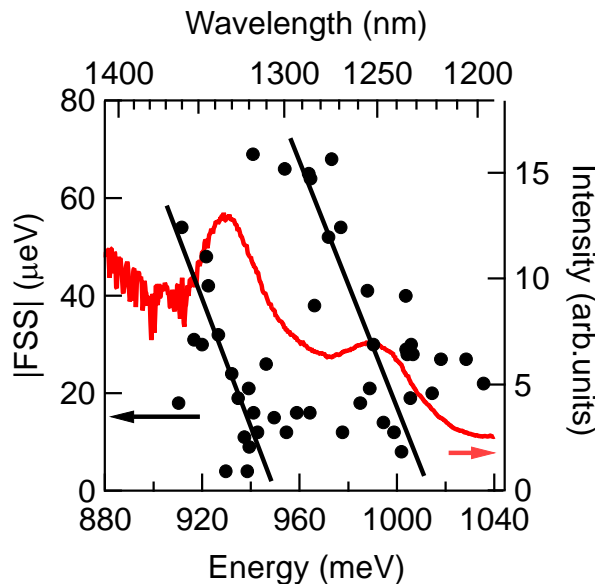

Fig. 3.30   Summarized statistical results for FSS over ~ 50 dots.

Figure 3.31 shows the direction of the polarization axis with respect to the *X* energy. They are randomly distributed, without showing significant correlations with the in-plane crystallographic axes. The absence of a preferential direction in the (111) plane suggests a high probability of finding QDs with negligible FSS over a broad spectral range.

The presence of dots with effectively zero FSS can be confirmed by measuring circularly polarized emission signals. In the presence of a finite FSS value, the polarization state of the emission light is expected to oscillate temporally between the left- and right-handed circular polarizations, where the oscillation period is determined by the inverse of the FSS. Therefore, in time-integrated experiments we cannot observe a high degree of circular polarization. By contrast, in the absence of FSS, circular polarization remains in time-integrated signals. Thus, the observation of circular polarization provides a sufficient condition for exciton degeneracy. The measurement principle is analogous to the well-known Hanle measurement, and was used to monitor FSS cancellation by an electric field [121]. Note that we use the 1.76-eV excitation light, which is predominantly absorbed by the unstrained InAlAs barrier with a direct band gap at 1.52 eV. Thus, the circularly polarized light induces spin-polarized electron injection from the heavy- and light-hole bands, but not from the split-off band. The maximum degree of spin polarization is therefore limited by 0.5 based on the assumption of fast hole relaxation. To avoid the effect of dynamic nuclear polarization, we set the excitation power at a sufficiently low level, where the average exciton population in the dot was ～0.5.
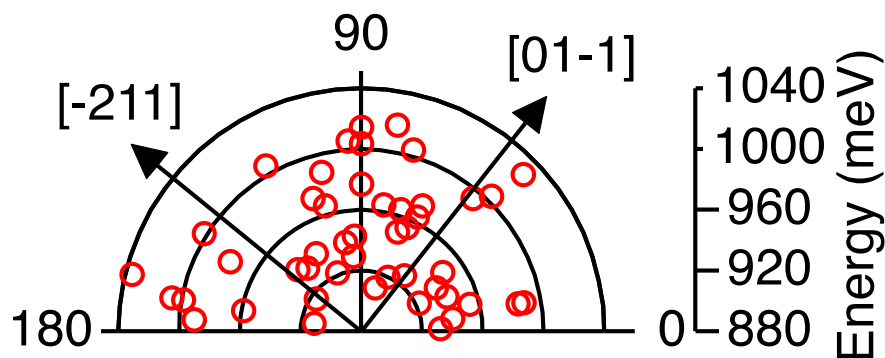

Fig. 3. 31　Direction of the polarization axis with respect to the *X* energy.

Optical orientation: Figure 3.32 shows optical orientation results for a selected dot without a detectable FSS (<4 μeV, QD1) and for a dot with a significant FSS (~ 45 μeV, QD2), respectively. The upper panels show unpolarized spectra, $I_\sigma + I_{\sigma^*}$, where I_σ (cocircular) is left-handed circular for excitation and left-handed circular for emission (or right-handed circular for excitation and emission), I_{σ^*} (cross circular) is left-handed circular for excitation and right-handed circular for emission (or opposite order). The lower panels show the differential spectra $I_\sigma - I_{\sigma^*}$, where a pronounced positive peak appears for the X line of QD1, but disappears for that of QD2. The positive degree of polarization for the X line of QD1 (+4.2%) is evidence of the degenerate exciton states. By contrast, the XX line does not exhibit a significant polarization in both QD1 and QD2, because the transition from comprises two routes with orthogonal polarizations. The other spectral lines follow well-known dynamics: X^+ shows a positive degree of polarization, which is due to spin-polarized electron injection. X^- shows a negative degree of polarization, which is accompanied by the spin-flip relaxation of electrons [117], [118].

Note that only a few dots exhibit circular polarization for the X line. A rough estimation of the probability of finding dots with a circularly polarized X line is ~2%, which agrees with the ratio of the natural width of our dots (0.5 μeV) divided by the distribution of FSS (25 μeV). Note that this probability is smaller than that previously observed for GaAs/AlGaAs QDs on (111)A (~5%).The small probability of telecom-wavelength dots reflects the relatively long emission lifetime as compared with that of visible-wavelength dots (560 ps for GaAs dots). Optical orientation therefore serves as an efficient way to select dots suited for entangled photon generation.
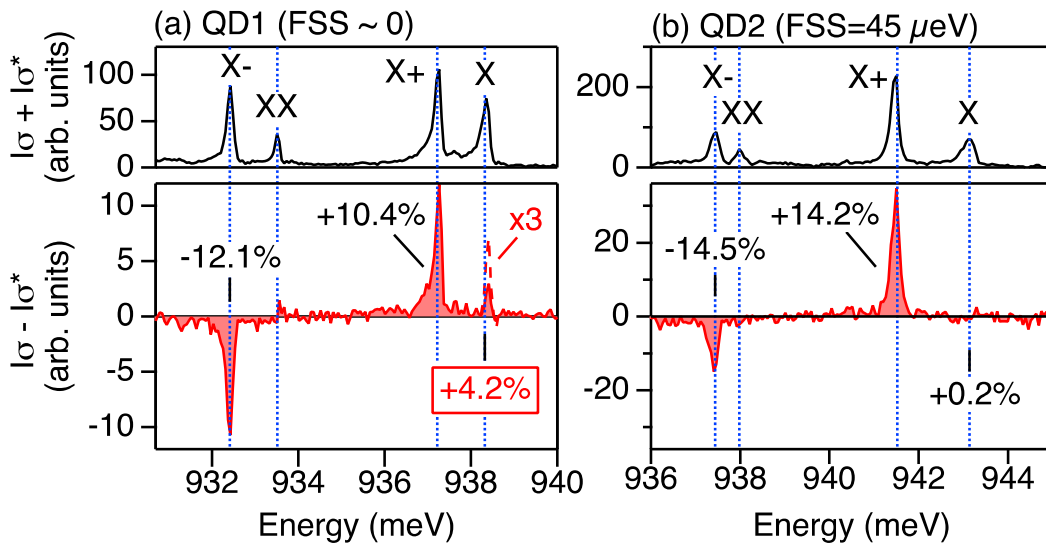

Fig. 3.32   Optical orientation results for a selected dot without a detectable FSS (<4 μeV, QD1) and for a dot with a significant FSS (~45 μeV, QD2), respectively.

3.6 Wavelength control: The use of InAl(Ga)As barriers

PL spectra in Fig. 3.18 covered the telecom wavelengths. However, their center wavelength is much shorter than 1.55 μm. In order to achieve strong emission at 1.55 μm, the use of an InAlGaAs barrier is suitable because InAlGaAs has a narrower band gap than InAlAs. In this section, we investigate InAs QDs on InAlGaAs/InP (111)A. Owing to the lower bandgap barrier, we can create small QDs emitting at longer wavelengths (Fig. 3.33).

The sequence of sample preparation is the similar with that of InAs QD on InAlAs/InP(111)A (Fig. 3.1), except the alloy composition of barrier materials ($In_{0.52}Al_{0.24}Ga_{0.24}As$, and $In_{0.52}Al_{0.12}Ga_{0.36}As$), and the temperature of indium droplet formation (320 °C). The latter is to achieve low density of QDs

Figure 3.34 shows the AFM image of the samples with (a) $In_{0.52}Al_{0.48}As$, (b) $In_{0.52}Al_{0.24}Ga_{0.24}As$, and (c) $In_{0.52}Al_{0.12}Ga_{0.36}As$. Well-defined QDs are observed with the density of (a) 3×10^9, (b) 6×10^9, and (c) 5×10^9 cm^{-2}. The density and size of QDs is slightly different. The difference may be due to the different composition of InAlGaAs growth surface or experimental errors such as a small difference in growth temperature or the amount of supplied indium.
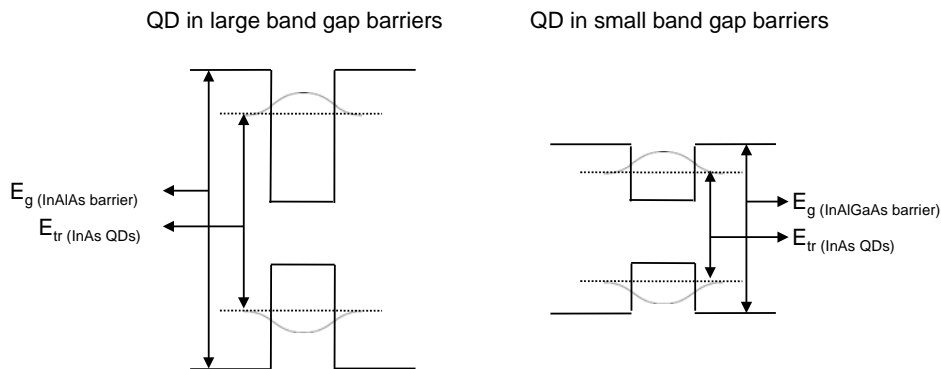

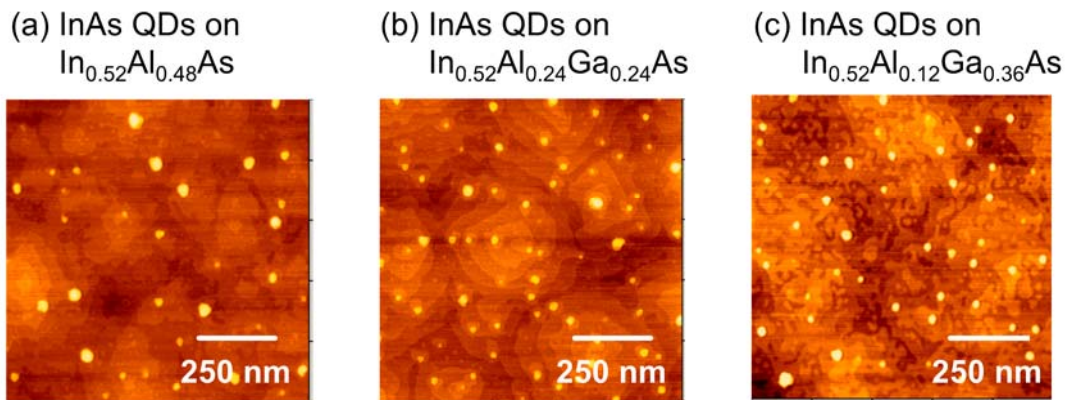Fig. 3.33   Dependence of carrier quantum confinement on barrier height.

Fig. 3.34   AFM of the samples with (a) $In_{0.52}Al_{0.48}As$, (b)$In_{0.52}Al_{0.24}Ga_{0.24}As$, and (c) $In_{0.52}Al_{0.12}Ga_{0.36}As$.

Figure 3.35 shows the PL spectra of ensembles of QDs for different excitation powers. These QDs are embedded in (a) $In_{0.52}Al_{0.48}As$ (b) $In_{0.52}Al_{0.24}Ga_{0.24}As$, and (c) $In_{0.52}Al_{0.12}Ga_{0.36}As$. For the $In_{0.52}Al_{0.48}As$ barrier sample (Fig. 3.35(a)), PL from InAs QDs was observed from 1000 to 1600 nm. The spectra consist of split peaks. The relative intensity between the multiple peaks was independent of excitation power.

For the $In_{0.52}Al_{0.24}Ga_{0.24}As$ barrier sample (Fig. 3.35(b)), PL from QDs was observed from 1200 to 1600 nm, together with a sharp peak from the barrier at 1070 nm. Thus, we can increase the emission wavelength of QDs by increasing the gallium content in the InAlGaAs alloy barrier.

For the $In_{0.52}Al_{0.12}Ga_{0.36}As$ barrier sample (Fig. 3.35(c)), PL from QDs was observed from 1350 to 1600 nm. Note that abrupt quench in the PL intensity at > 1.6 μm reflects the detection sensitivity. The barrier related peak is also observed at 1350 nm. Thus, both QD and barrier PLs shift to longer wavelengths with Ga concentration in the barrier. Note that this sample shows strong power dependence. With increasing power, the barrier related peak increases more than the QD band. Thus, we consider that this peak originates also from the excited states of QDs, where the transition energy of the QD excited states becomes close to that of the barrier.

Temperature dependence: Figure 3.36 shows dependence of PL spectra on temperature for the samples with InAs QDs embedded in (a) $In_{0.52}Al_{0.48}As$, (b) $In_{0.52}Al_{0.24}Ga_{0.24}As$, and (c) $In_{0.52}Al_{0.12}Ga_{0.36}As$. For the $In_{0.52}Al_{0.48}As$ barrier sample (Fig. 3.36(a)), the multiple peaks shift to longer wavelengths in union with temperature. Even at 300 K, the PL signal is observed.

For the $In_{0.52}Al_{0.24}Ga_{0.24}As$ barrier sample (Fig. 3.36(b)), the reduction of intensity with temperature is larger than that of $In_{0.52}Al_{0.48}As$ barrier sample. The PL signal is not observed at temperatures higher than 250 K. This behavior can be explained by the fact that carriers in the lower barrier QDs are more easily scattered to the barrier.

For $In_{0.52}Al_{0.12}Ga_{0.36}As$ barrier sample (Fig. 3.36(c)), the reduction of intensity with temperature is further large. The PL signal is only observed up to 150 K.
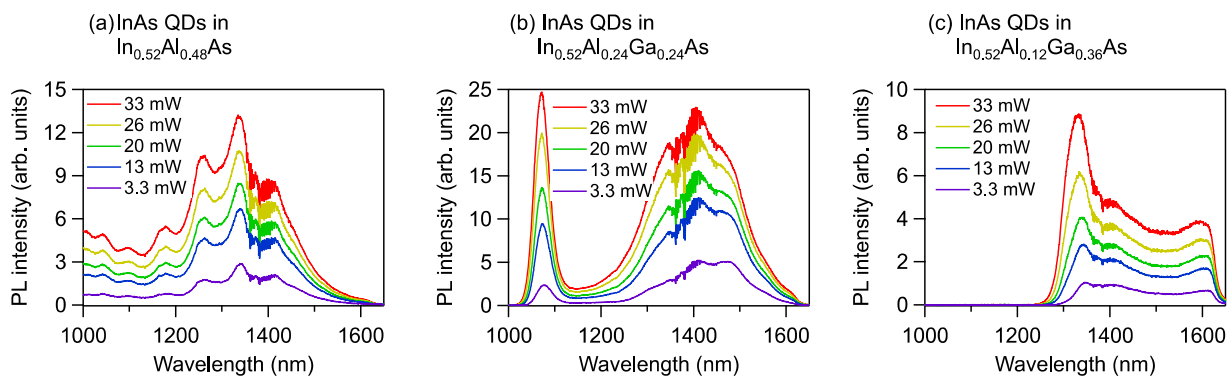

Fig. 3.35   PL spectra of ensembles of QDs depending on the excitation power with barrier composition of (a) $In_{0.52}Al_{0.48}As$ (b) $In_{0.52}Al_{0.24}Ga_{0.24}As$ and (c) $In_{0.52}Al_{0.12}Ga_{0.36}As$.

Figure 3.37 shows PL spectra of ensembles of QDs measured by PbS detector (blue line) and InGaAs photodiode (red line). For the $In_{0.52}Al_{0.48}As$ sample, the central peak was observed around at 1300 nm (Fig. 3.37(a)). For the $In_{0.52}Al_{0.24}Ga_{0.24}As$ sample, the central peak observed around at 1450 nm (Fig. 3.37(b)). For the $In_{0.52}Al_{0.12}Ga_{0.36}As$ sample, the central peak observed around at 1650 nm.

The increase in the gallium content in InAlGaAs alloy induce that the height of barrier becomes low with the increase of gallium content. Thus, the carriers in lower barrier are deeply confined than that for higher barrier.

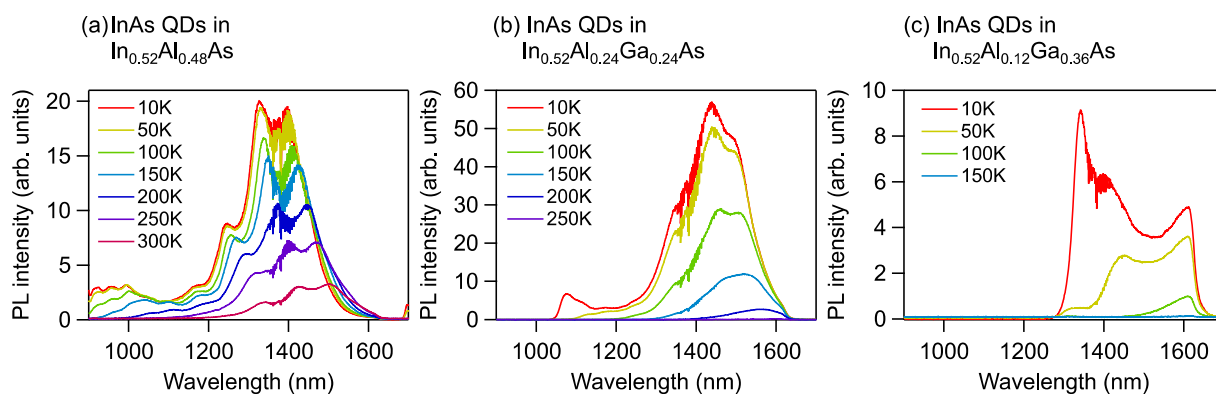**Fig. 3.36 Dependence of PL spectra on temperature for the samples with InAs QDs embedded in (a) $In_{0.52}Al_{0.48}As$, (b) $In_{0.52}Al_{0.24}Ga_{0.24}As$, and (c) $In_{0.52}Al_{0.12}Ga_{0.36}As$.**
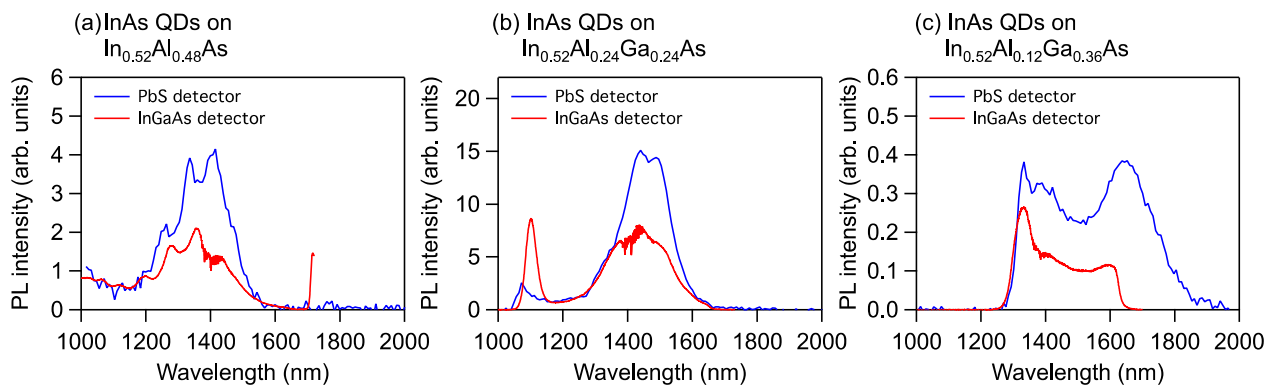

Fig. 3.37 PL spectra of ensembles of QDs measured by PbS detector and InGaAs detector.

3.7 Summary of chapter 3

We demonstrated the formation of InAs QDs on InAlAs/InP(111)A surface by droplet epitaxy. During the annealing of InAs QDs in the droplet epitaxial growth, a two-dimensional InAs layer was formed by flowing out of InAs from the QDs. By inserting an artificial InAs wetting layer, the morphology of QDs was controlled. AFM and X-TEM images revealed that symmetric QDs with flat tops were formed.

Highly-yield PL emission covered telecommunication wavelength. The PL emission was maintained up to room temperature, indicating high QD crystal quality. The emission wavelength can be easily tuned by increasing Ga content in the barrier materials (InAlGaAs), which emits even at 2 μm.

In the micro PL, bright excitonic emission from single QD was observed. Polarization-resolved PL experiments were performed to examine the FSS distribution. Resolution-limited splitting were confirmed. The random distribution of the polarization axis made it possible to find symmetric dots over a wide spectral range.

Our InAs QDs on InAl(Ga)As/InP (111)A substrates can play a crucial role in quantum information processing as an efficient entangled source that can work in telecom fiber networks

CHAPTER 4

Droplet epitaxy of InAs quantum dots on GaAs (111)A

4.1 Motivation

In the last chapter, we reported the growth of telecom InAs dots, where we used InP as the substrate. Compared with InP based approaches, GaAs based approaches have several advantages, which include lower device cost, higher thermal conductivity, and the availability of higher quality distributed Bragg reflectors. However, it is very challenging to fabricate high-quality telecom QDs on GaAs. An essential difficulty comes with large lattice mismatching between InAs and GaAs, which is ~ 7%. Strong compressive strain in InAs QDs/GaAs leads their emission wavelength to be shorter than ~1.0 μm, which is far from telecom wavelengths. Several groups have demonstrated efficient 1.3-μm QDs on GaAs. To extend emission wavelengths to 1.55 μm, various techniques, such as low-temperature growth of QDs, metamorphic AlGaAsSb buffer layer [100], antimony incorporation during QD growth [74], have been reported. A promising approach to restrain dislocations is the use of a metamorphic buffer layer as a virtual substrate for the succeeding epitaxial growth [101], but its repeatability is a serious issue.

In this chapter, we propose that droplet epitaxy on (111)A offers an approach to fabricating telecommunication-band QDs on GaAs. A key factor for constructing GaAs-based InAs heterostructure is the preparation of high-quality strain-relaxed layers, although their reproducible fabrication is very challenging owing to a large lattice mismatch. We overcome this problem by employing a (111)A surface, where strain relaxation occurs in the very initial stage of heteroepitaxial growth of InAs on GaAs(111)A [80]. Previous *in situ* measurements of strain relaxation in InAs on GaAs(111)A revealed that the in-plane lattice constant of the InAs overgrown layer starts relaxing at ~ 1 monolayer (ML) thickness, and an abrupt change in the lattice constant continues until ~5 ML [122]. On the basis of this understanding, we adopt a QD sample structure that contains three MLs of an InAs buffer layer on the GaAs(111)A substrate, prior to growing InAs QDs in InAlAs. Consequently, the InAs QDs are found to show a symmetric shape and strong emissions at telecom wavelengths.

4.2 Growth of metamorphic InAlAs layers on GaAs(111)A

In chapter 3, we observed telecom band emission from InAs QDs embedded in $In_{0.52}Al_{0.48}As$, where we chose this alloy concentration so that the InAlAs is lattice-matched to InP. In order to change a substrate from InP to GaAs with keeping the dot emission wavelength unchanged, we need to prepare metamorphic $In_{0.52}Al_{0.48}As$ layers, where the lattice constant of the InAlAs barriers is the same with its bulk value. Here we propose the growth of high-quality metamorphic layers by inserting a very thin InAs buffer layer between GaAs and InAlAs. Preceding study on the growth of InGaAs metamorphic layers is presented elsewhere.

The schematic of sample structure is shown in Fig.4.1. We carried out the following growth sequence:

0. Installation of semi-insulating (Fe-doped) GaAs(111)A as a substrate
1. Growth of a 50 nm GaAs buffer layer at 500 °C
2. Growth of a 3 ML (1.05 nm) InAs layer at 450 °C
3. Growth of a 100 nm $In_{0.52}Al_{0.48}As$ layer at 470 °C

For comparison, we prepared a sample with the direct growth of InAlAs on GaAs(111)A.

An atomic force microscope (AFM) was used to characterize the surface morphologies. Dark-field cross-sectional transmission electron microscopy (TEM) and X-ray diffraction (XRD) were analyzed to study the structural properties.
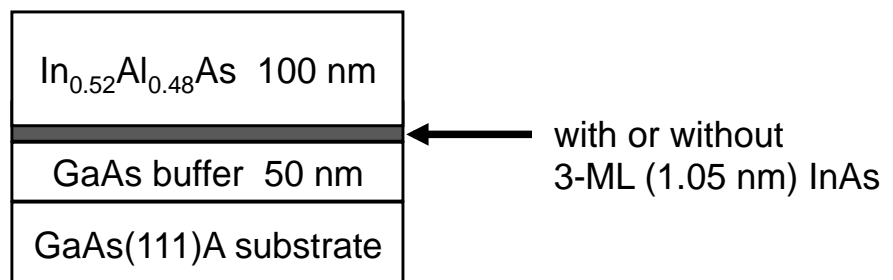

Fig. 4.1   Schematic of sample structure.

Surface analysis by AFM: Figure 4.2 shows AFM image of the InAlAs surface (a) grown directly on GaAs(111)A without inserting an InAs layer, and (b) grown with inserting a 3-ML InAs. In the both samples, a flat surface with terraces and steps is clearly visible, and no island growth occurs. However, the root-mean-square (RMS) roughness of the surface was improved from 0.53 nm in the InAlAs directly grown on GaAs(111)A sample to 0.37 in the InAlAs grown on 3-ML InAs / GaAs(111)A sample.

XRD analysis: Figure 4.3 shows a rocking curve profile of an InAlAs layer grown on GaAs (111)A, without thin InAs layer (black line) and with 3-ML InAs layer(red line). It shows two diffraction peaks, which originate from GaAs and $In_{0.52}Al_{0.48}As$. In both samples, the peak for GaAs and the peak for InAlAs was observed at around 27.3°/ 2 theta and 26.3° / 2theta, respectively. For the direct growth of InAlAs sample (black line), the InAlAs might be slightly strained due to distortion of lattice constant, indicating the broader peak. However, the peak for InAlAs seems to be shaper than that for InGaAs (Fig. 4.3), the strain-relaxation of InAlAs layer might be faster than that for InGaAs or it might be related to the composition of In(Al,Ga)As. For InAlAs with 3-ML InAs sample, the peak for InAlAs is shaper than that of the direct growth InAlAs. The shaper peak signifies that a higher crystal quality of InAlAs.

(a) Direct growth   (b) Inserted 3 ML InAs
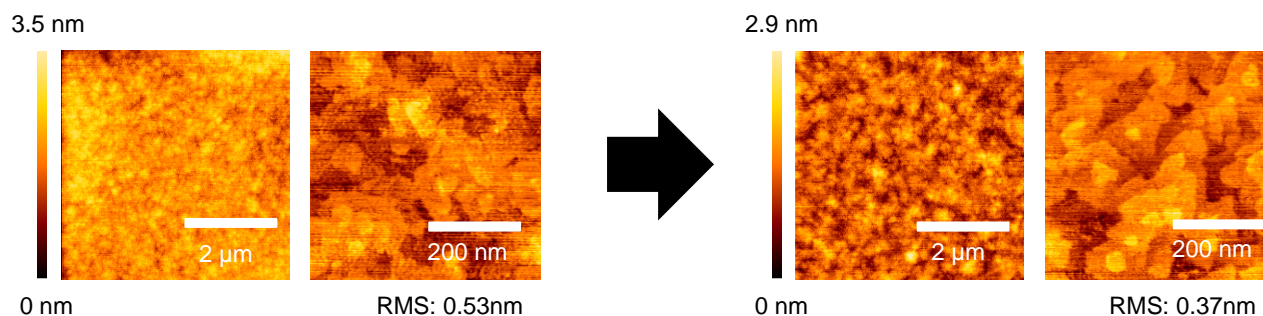

Fig. 4.2   AFM images of the InAlAs surface (a) grown directly on GaAs(111)A without inserting an InAs layer, and (b) grown with a 3-ML InAs.
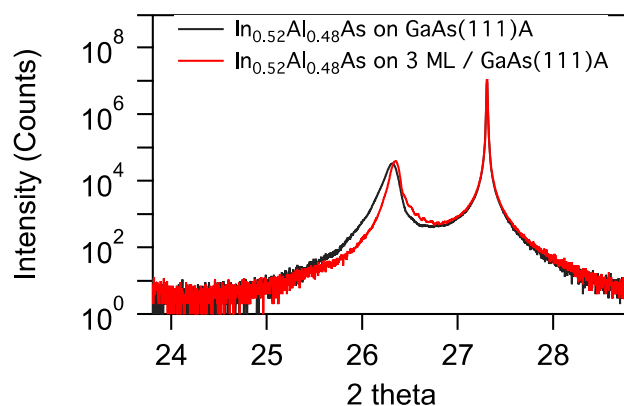

Fig. 4.3   Rocking curve profile of an InAlAs layer grown on GaAs (111)A, without thin InAs layer (black line) and with 3-ML InAs layer(red line).

Figure 4.4 shows the two-dimensional reciprocal space map for XRD 115 reflections of (a) direct growth and (b) inserted 3 ML InAs. The $In_{0.52}Al_{0.48}As$ peak is located close to the position expected for unstrained $In_{0.52}Al_{0.48}As$ in both samples. Thus, efficient strain relaxation occurs. We assume that the lattice-relaxation occurs easily in high indium content in In(Al, Ga)As. In the case of a high indium content in In(Al, Ga)As, the lattice constant is larger than that of low indium content. Thus, the threading dislocations occur more easily to reduce strain energy, which is observed on (111) surface [91,92]. by insertion 3-ML InAs, however, the InAlAs peak becomes shaper, the strain-relaxation might be enhanced. In the calculated ration of in-plane and vertical lattice spacing, the ratio of GaAs and InAlAs is 1.4156 and 1.4056, respectively. Thus, InAlAs is slightly strained, which might be tensile. In this sample, InAlAs layer was grown on 3-ML InAs layer. We assume that InAs layer might be lead to the tensile strain due to large lattice constant.

TEM analysis on capped quantum dots: Figure 4.5 shows the cross-sectional TEM image of the 3-ML InAs inserted sample. It is observed that dislocations are present at the interface between InAs and GaAs. No threading dislocations are observed in InAlAs.

It implies that lattice-relaxation occurs by introducing misfit dislocation at the interface between InAs and GaAs, and the dislocations did not extend into the InAlAs layer. Thus, 3 ML InAs might be serve as good buffer for strain relaxation.
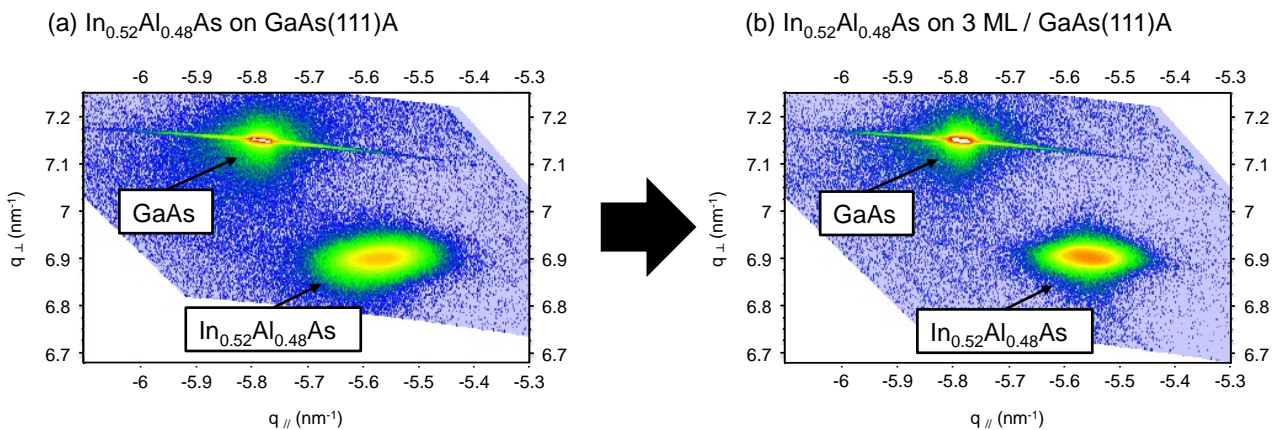

Fig. 4.4 Two-dimensional reciprocal space map for XRD 115 reflections of (a) direct growth and (b) inserted 3 ML InAs.
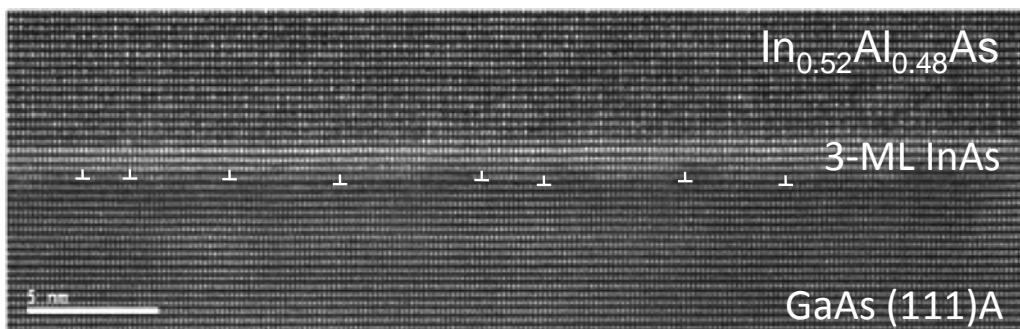

Fig. 4.5 Cross-sectional TEM image of 3-ML InAs inserted sample.

PL characterization on quantum wells: We investigated the optical properties of InGaAs multiple quantum wells on metamorphic InAlAs layer. The schematic of sample structure is shown in Fig. 4.6(a). We carried out the following growth sequence:

0. Installation of semi-insulating (Fe-doped) GaAs(111)A as a substrate

1. Growth of a 50 nm GaAs buffer layer at 500 °C

2. Growth of a 3 ML InAs layer at 450 °C

3. Growth of a 100 nm $In_{0.52}Al_{0.48}As$ layer at 470 °C

4. Growth of a 3 ML (1.05 nm) $In_{0.53}Ga_{0.47}As$ layer at 470 °C

5. Growth of a 20 nm $In_{0.52}Al_{0.48}As$ layer at 470 °C

6. Repeat 4 - 5, 3 times

7. Growth of a 20 nm $In_{0.52}Al_{0.48}As$ layer at 470 °C

8. Growth of a 1 nm $In_{0.53}Ga_{0.47}As$ layer at 470 °C

For comparison, we also prepared the sample without inserting a 3 ML InAs layer.

Figure 4.6(b) shows the PL spectrum of InGaAs/InAlAs quantum wells with and without inserting 3-ML InAs layer. For the sample with the 3-ML InAs, strong PL emission from QWs is observed at around a wavelength of 1200 nm. Its intensity is significantly higher than that of the sample without an InAs layer. The stronger PL intensity suggests a lower density of dislocations, and higher crystal quality. Thus, the insertion of a 3-ML InAs leads to the formation of a high crystal quality InAlAs layer without dislocations.
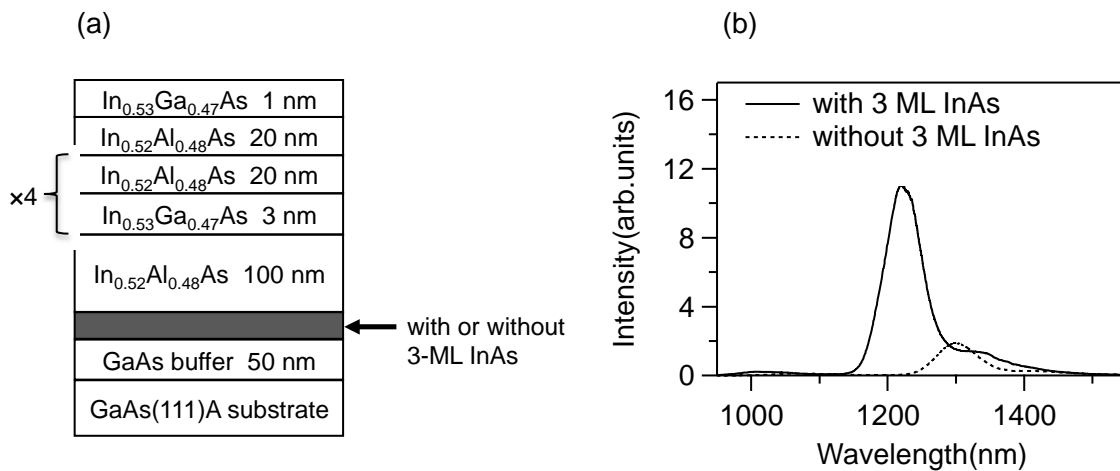

Fig. 4.6 (a) Schematic of sample structure. (b) PL spectrum of InGaAs/InAlAs quantum wells with and without the insertion of 3-ML InAs layer.

4.3 Growth of InAs quantum dots on metamorphic InAlAs

4.3.1 Experimental details

In this section, we fabricate InAs QDs on the metamorphic InAlAs that was studied in the last section.

The schematic of sample structure is show in Fig. 4.7. We carried out the following growth sequence:

0. Installation of semi-insulating (Fe-doped) GaAs(111)A as a substrate
1. Growth of a 50 nm GaAs buffer layer at 500 °C
1. Growth of a 3 ML (1.05 nm) InAs layer at 450 °C
2. Growth of a 100 nm $In_{0.52}Al_{0.48}As$ layer at 470 °C
3. Cool down the substrate to 320 °C
4. Supply of indium with 0.4 ML at 0.2 ML/s (without As_4 flux).
5. Supply of an As_4 flux with 3×10^{-5} Torr at 270 °C.
6. Annealing at 370 °C for 5 min under As_4 supply
7. Capping with a 75 nm $In_{0.52}Al_{0.48}As$ layer at 370 °C
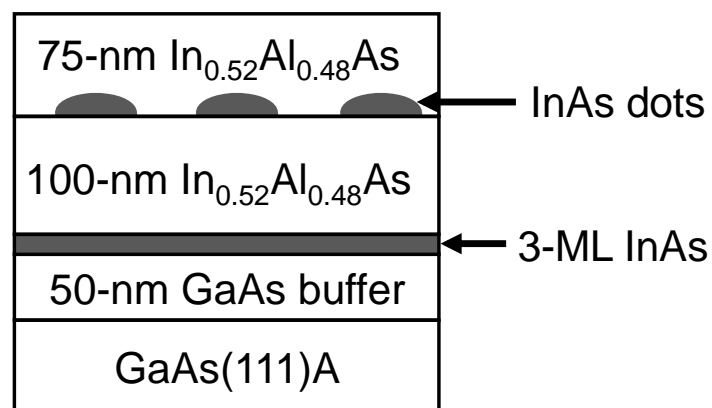8. Annealing at 470 °C for 5 min

Fig. 4.7   Schematic of sample structure.

We observed the RHEED pattern during the growth. Surface morphology of InAs QDs was investigated by AFM. For optical characterization, we measured PL spectra using a cw diode-pumped laser (532 nm) as an excitation source. The PL signals were analyzed by an InGaAs detector or a PbS detector. The spectra were observed as a function of temperature from 9 K to 300 K.

Surface analysis during growth: Figure 4.8 shows RHEED patterns during growth for InAs QDs on $In_{0.52}Al_{0.48}As$/3-ML InAs/GaAs (111)A. After the growth of InAlAs layer, a streak pattern is observed in the orthogonal [1-10] and [11-2] azimuths. This indicates the formation of a flat surface. (2×2) reconstruction was established on (111)A   [72,73]. After the supply of indium without As_4 flux, the streak pattern changes to a halo pattern. This indicates the formation of liquid indium droplets. After the supply of As_4, the halo pattern changes to spotty. This indicates the crystallization of In droplets into InAs QDs.
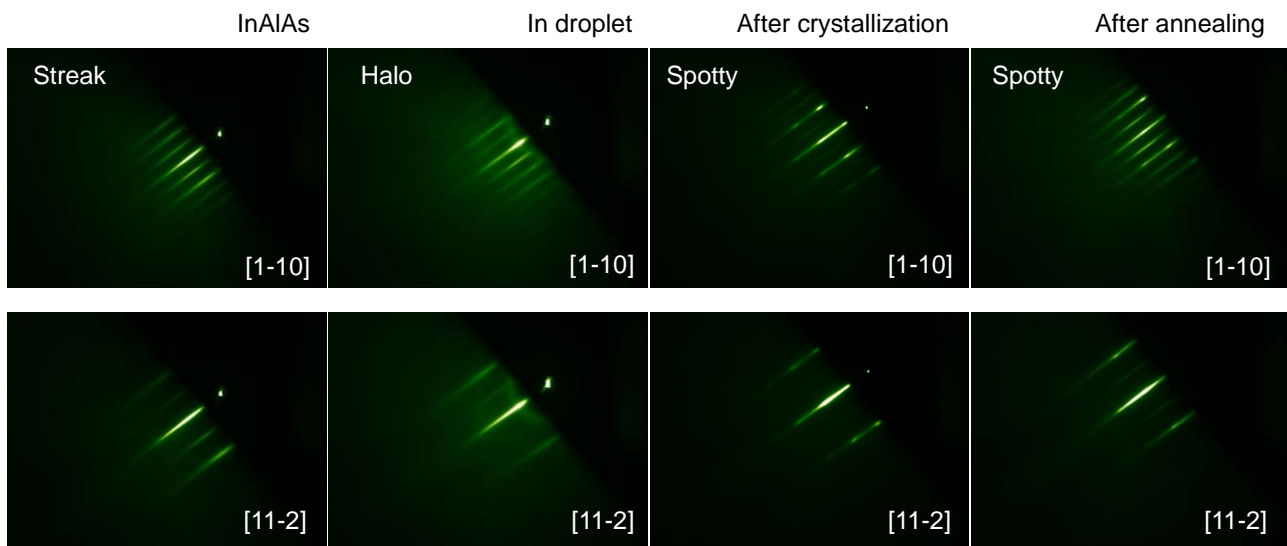

Fig. 4.8   RHEED patterns during growth for InAs QDs on $In_{0.52}Al_{0.48}As$/3-ML InAs/GaAs (111)A.

4.3.2   Morphology analysis

Figure 4.9(a) shows the AFM image of InAs QDs grown on $In_{0.52}Al_{0.48}As$ / 3-ML InAs / GaAs(111)A. Well-defined InAs QDs were formed. The density of QDs is $5 \times 10^9/cm^2$, and average lateral size and height are 41 and 1.6 nm, respectively. The size distribution is shown in Fig. 4.9(b). The distribution of the diameter and height is ±23% and ±28%, respectively. The linear dependence of height on lateral size indicates that the same aspect ratio (height/lateral) in all QDs.

Figure 4.10 shows the cross-sectional profile of relatively small, medium, and large QDs. In all QDs, nearly identical cross-sections are observed along orthogonal in-plane directions [01-1] and [-211]. The presence of shape symmetry in our dots is a direct consequence of the three-fold rotational symmetry of the (111)A surface.

(a)   (b)

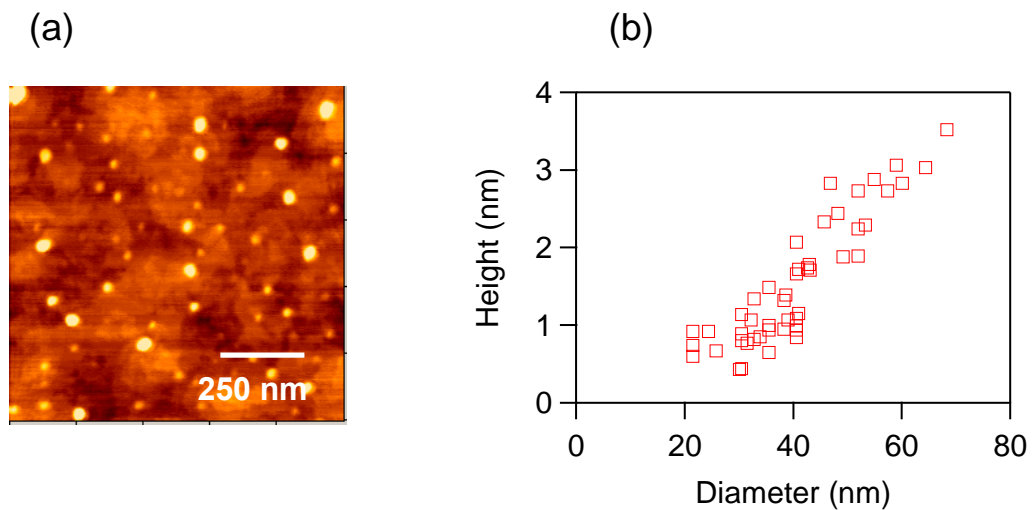**Fig. 4.9   (a) AFM images of InAs QDs grown on $In_{0.52}Al_{0.48}As$ / 3-ML InAs / GaAs(111)A and (b) statistics for QD size distribution.**
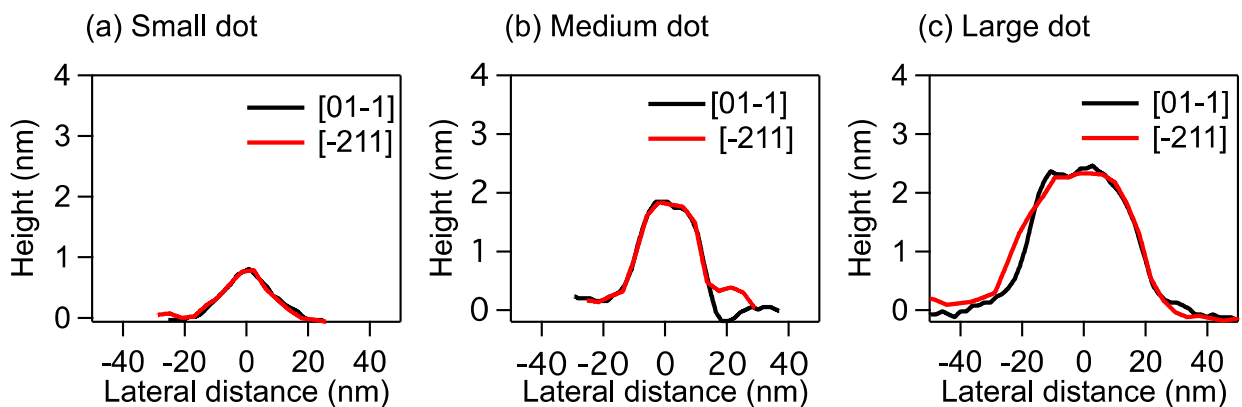

Fig. 4.10   Cross-sectional profile of relatively small, medium, and large QDs, respectively.

4.3.3 Optical properties

Figure 4.11(a) shows the PL spectra of capped InAs QDs. Broad PL spectrum at 9 K (λ= 900 nm ~ 1.6 μm) is observed at around 1.5 μm. Note that abrupt quench in the PL intensity at λ> 1.6 μm reflects the detection sensitivity. This broad emission is consistent with the large size distribution of QDs. The PL spectrum consists of multiple emission peaks. We attribute them to different groups of QDs whose heights vary by a ML step. The observation of the split peaks comes due to the fact that QDs have a flattop shape. The PL signal is clearly visible up to room temperature (Fig. 4.11(b)). The observed room temperature PL emission suggests that the crystal quality of the InAs QD is not degraded by using metamorphic InAlAs that are formed with 3ML-InAs insertion.

Figure 4.12 shows a comparison between the PL spectrum of InAs QDs on InP (111)A and that of InAs QDs on GaAs(111)A. Both QDs are embedded in $In_{0.52}Al_{0.48}As$. For the InAs QDs on GaAs, 3 ML InAs is inserted between GaAs and InAlAs. The PL intensity of QDs on GaAs is slightly weaker than that of QDs on InP. The difference is only a factor of 2. The efficient PL emission of QDs on GaAs suggests the formation of high quality InAs QDs even on GaAs. Note that the energy level of InAs layer is lower than that of InAlAs. Thus, photo-injected carriers are effectively trapped to InAs.

The emission wavelength of InAs QDs on GaAs is longer than that of InAs QDs on InP. It is probably due to the presence of a tensile strain in $In_{0.52}Al_{0.48}As$ barrier on 3 ML InAs / GaAs.
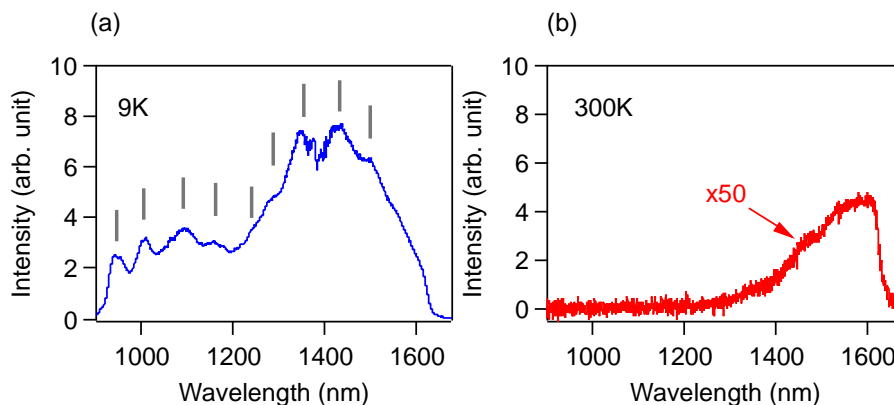

Fig. 4.11   PL spectra of capped InAs QDs measured at (a) 9 K and (b) 300 K.
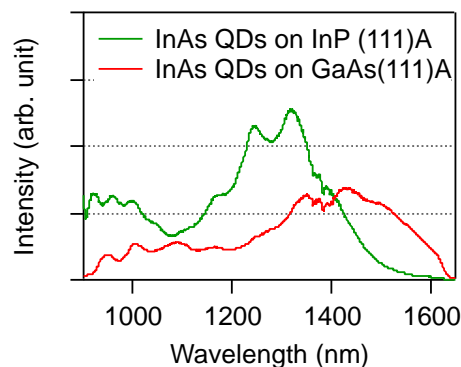
Fig. 4.12   Comparison between the PL spectrum of InAs QDs on InP (111)A and that of InAs QDs on GaAs(111)A. Both QDs are embedded in $In_{0.52}Al_{0.48}As$.

4.3.4   Wavelength control

In this section, we tune the emission wavelength using $In_xAl_{1-x}As$ barrier with different alloy composition. The schematic of sample structure is shown in Fig. 4.13. We carried out the following growth sequence:

0.   Installation of semi-insulating (Fe-doped) GaAs(111)A as a substrate

1.   Growth of a 50 nm GaAs buffer layer at 500 °C

2.   Growth of a 3 ML (1.05 nm) InAs layer at 450 °C

3.   Growth of a 100 nm $In_xAl_{1-x}As$ layer at 470 °C (x = 0.6, and 0.75)

4.   Cool down the substrate to 320 °C

5.   Supply of indium with 0.4 ML at 0.2 ML/s (without As_4 flux)

6.   Supply of an As_4 flux with $3×10^{-5}$ Torr at 270 °C

7.   Annealing at 370 °C for 5 min under As_4 supply

8.   Capping with a 75 nm $In_{0.52}Al_{0.48}As$ layer at 370 °C

9.   Annealing at 470 °C for 5 min

Fig. 4.13   Schematic of sample structure

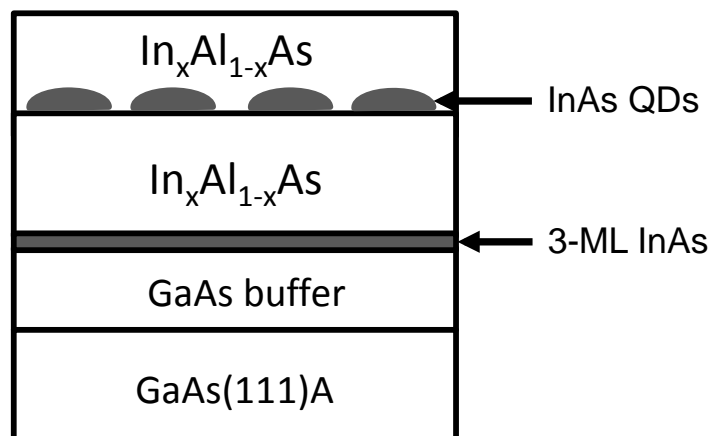Figure 4.13 shows the AFM image of the samples with (a) $In_{0.52}Al_{0.48}As$, (b) $In_{0.6}Al_{0.4}As$, and (c) $In_{0.75}Al_{0.25}As$. Well-fined the QDs were observed with the density of (a) 5×10^9, (b) 4.4×10^9, and (c) 3.7×10^9 cm^{-2}, respectively.

Figure 4.14 shows the normalized PL spectra of InAs QDs on $In_{0.52}Al_{0.48}As$, $In_{0.6}Al_{0.4}As$, and $In_{0.75}Al_{0.25}As$ measured by a PbS detector at 9K. For $In_{0.52}Al_{0.48}As$ barrier sample, central peak from InAs QDs was observed at 1500 nm. For $In_{0.6}Al_{0.4}As$ barrier sample, the peak from InAs QDs was observed at 1600 nm. For $In_{0.75}Al_{0.25}As$ barrier sample, the peak from the InAs QDs was observed at 1800 nm.

(a) InAs QDs on $In_{0.52}Al_{0.48}As$

(b) InAs QDs on $In_{0.6}Al_{0.4}As$

(c) InAs QDs on $In_{0.75}Al_{0.25}As$

250 nm

250 nm

250 nm
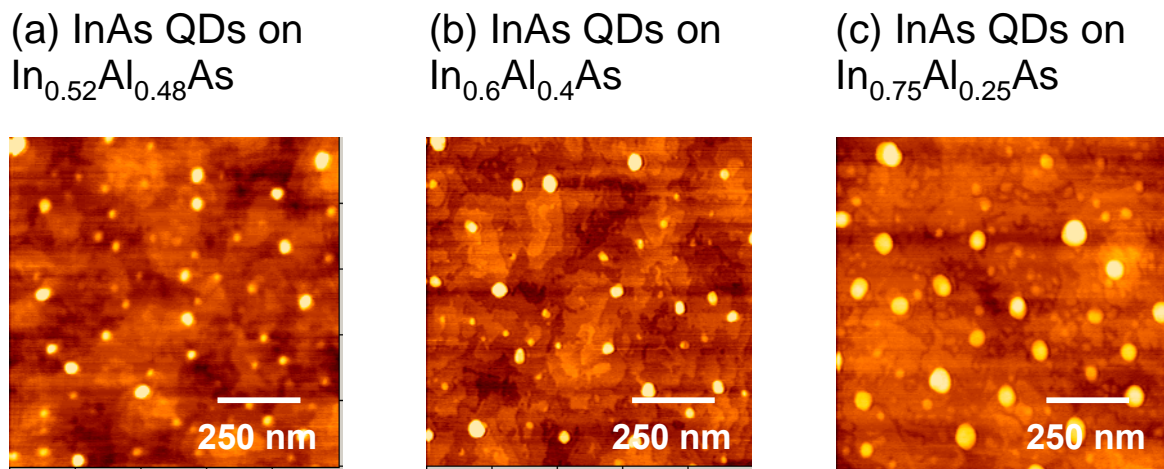
Fig. 4.14   AFM of the samples with (a) $In_{0.52}Al_{0.48}As$, (b) $In_{0.6}Al_{0.4}As$, and (c) $In_{0.75}Al_{0.25}As$.
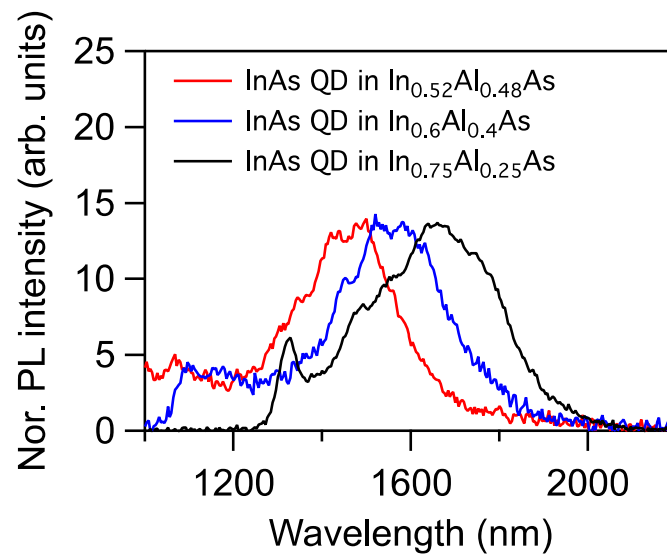
Fig. 4.15   Normalized PL spectra of InAs QDs on $In_{0.52}Al_{0.48}As$, $In_{0.6}Al_{0.4}As$, and $In_{0.75}Al_{0.25}As$ measured by PbS detector at 9K.

4.4 Summary of chapter 4

We demonstrated the droplet epitaxial growth of InAs QDs, which emitted at telecommunication wavelengths on GaAs (111)A. A high quality metamorphic InAlAs layer was formed by inserting 3 ML of InAs between GaAs (111)A and InAlAs.

For the InGaAs quantum wells structures on the metamorphic InAlAs, highly-efficient PL emission was observed. Ultra-thin InAs layer might not be hinder the optical properties. The inserting a thin InAs layer between $In_{0.52}Al_{0.48}As$ and GaAs (111)A enable us to form a high quality metamorphic $In_{0.52}Al_{0.48}As$ on GaAs (111)A.

For InAs QDs grown on the InAlAs surface by droplet epitaxy, they exhibited a laterally symmetrical shape due to the C_{3v} symmetry of (111) surface. The QDs emit at 1.55 μm at low temperature. The PL emission is clearly observed at room temperature, it suggests high crystal quality of our QDs.

Strain-relaxation technology is one of the major issues in epitaxial growth. This simple way to strain-relaxation might be play a role of fabrication of telecommunication devices. We believe that strain relaxation technique in promising to realize GaAs based InAs QDs emitting at telecommunication wavelengths.

CHAPTER 5   Conclusions and future work

In this study, we demonstrated the growth of self-assembled GaAs and InAs QDs via droplet epitaxy. We studied their structural and optical properties toward the QD application to quantum information devices.

In chapter 2, we studied the height-controlled GaAs QDs on AlGaAs/GaAs(100). We found that the QD height was controlled within a wide range by adjusting the supplied amount of gallium in the process of droplet formation. The emission wavelength was red shifted together with increasing QD height. Statistical analysis revealed that the uniformity of GaAs QDs was high in the case of small QDs (the amount of gallium: 1.5 ~ 3 ML), which results in narrow PL spectra of ensemble QDs. In contrast, large size fluctuation was observed in the case of large QDs (the amount of gallium: 5 ~ 10 ML), which results in broad PL spectra of ensemble QDs. We attributed the difference to the mechanism of crystallization process. In the study of optical properties on single QDs, we observed that the PL signal from small QDs was very sharp, and the PL signal was broadening with increasing QD size. The height-controlled GaAs QDs enabled us to investigate spectral broadening caused by quantum-confined Stark effect. Emission line width of a single QD is important for application to quantum communication. I expect that our study will play a role in solving the line broadening for a single QD application.

The engineering of the emission properties of QDs is important issues in not only a single QD application in but also ensemble QDs applications such as QD lasers. For the QD lasers, the ground state level and the energy separation between the ground state and the excited state determine the laser properties, which are associated with emission wavelength and thermal broadening in emission spectra, respectively. The emission wavelength is mainly tuned by QD height. The energy separation can be tuned by lateral size of QDs. Note that the small lateral size results in large energy separation, which suppresses the thermal broadening in emission spectra. Previously, it was difficult to achieve independent control of height and lateral size. In the presence of the height-controlled system, we controlled the QD height with maintaining lateral size. I believe that the technique of height-controlled QDs offers opportunities for fabrication of such QD applications.

In chapter 3, we demonstrated the formation of InAs QDs on InAlAs/InP(111)A by droplet epitaxy for the entangled photon emission at telecommunication wavelength of 1.3 and 1.55 μm. In the previous studies of droplet epitaxy, we have realized highly symmetric GaAs QDs, and demonstrated high quality entangled photon emission. For the next step, it was highly desired to extend the emission wavelength to the telecommunication wavelengths. By applying the droplet epitaxy to the new material system, InAs QDs on InAlAs/InP, we successfully formed highly symmetrical InAs QDs. In the detailed investigation of the growth mechanism, we found that a two-dimensional InAs layer was formed by flowing out of InAs from the QDs, which was not observed in GaAs/AlGaAs QDs system. We also found that the QD morphology can

be controlled by inserting an artificial InAs wetting layer before the QD formation. AFM and cross-sectional TEM images revealed that symmetric QDs with flattop were formed due to C_{3v} symmetry of (111) surface. Highly-yield PL emission was observed from QDs, which covered telecommunication wavelengths. The PL emission was maintained up to room temperature, indicating high QD crystal quality. The emission wavelength could be easily tuned by increasing gallium content in the InAlGaAs barrier, which emits even at a wavelength of 2 μm. In the study of optical properties on single QDs, bright excitonic emission from single QDs was observed. Polarization-resolved PL experiments were performed to examine the FSS distribution. Resolution-limited splitting was confirmed. The random distribution of the polarization axis made it possible to find symmetric QDs over a wide spectral range. I suppose that the present system is highly promising to realize on-demand entangled photon emission at telecommunication wavelengths.

In addition, for the practical applications, the change of the substrate from InP to GaAs is desired because of a lower device cost. In chapter 4, we studied the droplet epitaxial growth of InAs QDs, which emits at telecommunication wavelengths on GaAs(111)A. Insertion of a thin InAs layer between $In_{0.52}Al_{0.48}As$ and GaAs(111)A enabled us to form a high quality metamorphic $In_{0.52}Al_{0.48}As$ on GaAs(111)A. The InAs QDs on the metamorphic InAlAs exhibited a laterally symmetrical shape. The QDs emitted at 1.55 μm at low temperature. The PL emission was also observed at room temperature, which suggests high crystal quality of our QDs. We tuned the emission wavelength of QDs to 2 μm with reducing strain of QDs by increasing indium contents in InAlAs barrier. Thus, we expect that small QDs emit at the wavelength of 1.55 μm with sharp spectral emission (as mentioned in chapter 2). Also, strain-reduced QDs are strongly required for highly symmetrical QDs, since the strain induces asymmetry. The InAs QDs in InAlAs on GaAs system presented here are promising for the emission of the GaAs-based InAs QDs emitting at telecommunication wavelengths.

The strain-relaxed metamorphic layer is promising for epitaxial growth. III-V semiconductor materials are indispensable in modern science. However, the use of epitaxial layers on a substrate is limited due to the different lattice constant between the epitaxial layers and the substrate. We found that the lattice constant of a thin InAs layer was flexible between two epitaxial layers. Thus, the InAs thin layer can be applied to variety substrate such as silicon. The presence of the technique for strain relaxation could play a crucial role in engineering QD structure and further band structure.

Originally, droplet epitaxy was used in lattice-matched system. Though the present study, we have successfully extended the scope of the droplet epitaxy to lattice-mismatched systems. Moreover, we were able to easily tune the QD size and density in the droplet formation process. However, due to the nature of the self-assembled growth, precisely controlling the size and positioning of QDs was not easy. For applying QDs to practical devices, problems remain.

QD have stimulated interest due to their potential application in entangled photon emitters. The entangled photon source is a key aspect of quantum communication. As the modern information society is composed of information processing, information storage and information communication, and next social

will be composed of quantum information processing, quantum information storage, and quantum information communication. I believe that this study will make a significant contribution to realization of this quantum information society.

References

[1] J. Bardeen and W. H. Brattain, "The transistor, a semi-conductor triode," *Phys. Rev.* **74**, 730 (1948).

[2] W. L. Bond, W. P. Mason, H. J. McSkimin, K. M. Olsen, and G. K. Teal, "The elastic constants of germanium single crystal," *Phys. Rev.* **78**, 176 (1950).

[3] R. N. Hall, G. E. Fenner, J. D. Kingsley, T. J. Soltys, and R. O. Carlson, "Coherent Light Emission from Ga-As Junctions," *Phys. Rev. Lett.* **9,** 366 (1962).

[4] Z. I. Alferov, V. M. Andreev, D. Z. Garbuzov, Y. V. Zhilyaev, E. P Morozov, E. L. Portnoi, and V. G. Trofim, "Investigation of the influence of the AlAs-GaAs heterostructure parameters on the laser threshold current and the realization of continuous emission at room temperature," *Sov. Phys. Semicond*. **4**, 1575 (1971).

[5] R. D. Dupuis, P. D. Dapkus, N. Holonyak, E. A. Rezek, and R. Chin, "Room-temperature laser operation of quantum-well $Ga_{(1-x)}Al_xAs$-GaAs laser diodes grown by metalorganic chemical vapor deposition," *Appl. Phys. Lett.* **32**, 295 (1978).

[6] R. D. Dupuis, P. D. Dapkus, N. Holonyak, and R. M. Kolbas, "Continuous room-temperature multiple-quantum-well $Al_xGa_{1-x}As$-GaAs injection lasers grown by metalorganic chemical vapor deposition," *Appl. Phys. Lett.* **35**, 487 (1979).

[7] R. Chin, N. Holonyak, B. A. Vojak, K. Hess, R. D. Dupuis, and P. D. Dapkus, "Temperature dependence of threshold current for quantum-well $Al_xGa_{1-x}As$-GaAs heterostructure laser diodes," *Appl. Phys. Lett.* **36**, 19 (1980).

[8] F. Koyama, S. Kinoshita, and K. Iga, "Room-temperature continuous wave lasing characteristics of a GaAs vertical cavity surface-emitting laser," *Appl. Phys. Lett.* **55**, 221 (1989).

[9] C. J. Chang-Hasnain, M. Orenstein, A. Von Lehmen, L. T. Florez, J. P. Harbison, and N. G. Stoffel, "Transverse mode characteristics of vertical cavity surface-emitting lasers," *Appl. Phys. Lett.* **57,** 218 (1990).

[10] K. Klitzing, G. Dorda, and M. Pepper, "New method for high-accuracy determination of the fine-structure constant based on quantized Hall resistance," *Phys. Rev. Lett.* **45**, 494 (1980).

[11] Y. Arakawa, and H. Sakaki, "Multidimensional quantum well laser and temperature dependence of its threshold current," *Appl. Phys. Lett.*, **40**, 939 (1982).

[12] M. Asada, Y. Miyamoto, and Y. Suematsu, "Gain and the threshold of three-dimensional quantum-box lasers," *IEEE* **QE-22,** 1915 (1986).

[13] L. Goldstein, F. Glas, J. Y. Marzin, M. N. Charasse, and G. Le Roux, "Growth by molecular beam epitaxy and characterization of InAs/GaAs strained-layer superlattices," *Appl. Phys. Lett.* **47**, 1099 (1985).

[14] N. Koguchi, S. Takahashi, and T. Chikyow, "New MBE growth method for InSb quantum well boxes," *J. Cryst. Growth.* **111,** 688 (1991).

[15] T. Fukui, S. Ando, Y. Tokura, and T. Toriyama, "GaAs tetrahedral quantum dot structures fabricated

using selective area metalorganic chemical vapor deposition," *Appl. Phys. Lett.* **58**, 2018 (1991).

[16]   H. F. Wong, D. L. Green, T. Y. Liu, D. G. Lishan, M. Bellis, E. L. Hu, P. M. Petroff, P. O. Holtz, and J. L. Merz, "Investigation of reactive ion etching induced damage in GaAs–AlGaAs quantum well structures," *J. Vac. Sci. Technol. B* **6**, 1906 (1988).

[17]   H. E. G. Arnot, M. Watt, C. M. Sotomayor-Torres, R. Glew, R. Cusco, J. Bates, and S. P. Beaumont, "Photoluminescence of overgrown GaAs-GaAlAs quantum dots," *Superlattices Microst.* **5**, 459 (1989).

[18]   R. Hanson, L. P. Kouwenhoven, J. R. Petta, S. Tarucha, and L. M. K. Vandersypen, "Spins in few-electron quantum dots," *Rev. Mod. Phys.* **79**, 1217 (2007).

[19]   A. Greilich, R. Oulton, E. Zhukov, I. Yugova, D. Yakovlev, M. Bayer, A. Shabaev, A. Efros, I. Merkulov, V. Stavarache, D. Reuter, and A. Wieck, "Optical Control of Spin Coherence in Singly Charged (In,Ga)As/GaAs Quantum Dots," *Phys. Rev. Lett.* **96**, 227401 (2006).

[20]   N. H. Bonadeo, J. Erland, D. Gammon, D. Park, D. S. Katzer, D. G. Steel, "Coherent Optical Control of the Quantum State of a Single Quantum Dot," *Science* **282**, 1473 (1998).

[21]   C. Santori, D. Fattal, M. Pelton, G. S. Solomon, and Y. Yamamoto, "Polarization-correlated photon pairs from a single quantum dot," *Phys. Rev. B* **66**, 045308 (2002).

[22]   O. Benson, C. Santori, M. Pelton, and Y. Yamamoto, "Regulated and entangled photons from a single quantum dot," *Phys. Rev. Lett.* **84**, 2513 (2000).

[23]   R. M. Stevenson, R. J. Young, P. Atkinson, K. Cooper, D. A. Ritchie, and A. J. Shields, "A semiconductor source of triggered entangled photon pairs," *Nature* **439**, 179 (2006).

[24]   N. Akopian, N. Lindner, E. Poem, Y. Berlatzky, J. Avron, D. Gershoni, B. Gerardot, and P. Petroff, "Entangled Photon Pairs from Semiconductor Quantum Dots," *Phys. Rev. Lett.* **96**, 130501 (2006).

[25]   J. Davies, *The Physics of Low-Dimensional Semiconductors*, (Cambridge University Press 1998) p. 4.

[26]   *Single Semiconductor Quantum Dots*, (*ed.* P. Michler, Springer, 2009) pp. 227-266.

[27]   J. Berezovsky, M. H. Mikkelsen, N. G. Stoltz, L. A. Coldren, and D. D. Awschalom, "Picosecond Coherent Optical Manipulation of a Single Electron Spin in a Quantum Dot," *Science* **320**, 349 (2008).

[28]   K. Nishi, H. Saito, S. Sugou, and J.-S. Lee, "A narrow photoluminescence linewidth of 21 meV at 1.35 μm from strain-reduced InAs quantum dots covered by $In_{0.2}Ga_{0.8}As$ grown on GaAs substrates," *Appl. Phys. Lett.* **74**, 1111 (1999).

[29]   M. Jo, T. Mano, and K. Sakoda, "Lasing in ultra-narrow emission from GaAs quantum dots coupled with a two-dimensional layer," *Nanotechnology* **22**, 335201 (2011).

[30]   N. N. Ledentsov, "Quantum dot laser," *Semicond. Sci. Technol.* **26**, 014001 (2010).

[31]   P. M. Varangis, H. Li, G. T. Liu, T. C. Newell, A. Stintz, B. Fuchs, K. J. Malloy, and L. F. Lester, "Low-threshold quantum dot lasers with 201 nm tuning range," *Electronics Letters* **36**, 1544 (2000).

[32]   L. V. Asryan and R. A. Suris, "Inhomogeneous line broadening and the threshold current density of a semiconductor quantum dot laser," *Semicond. Sci. Technol.* **11**, 554 (1996).

[33]   J. Faist, F. Capasso, D. L. Sivco, C. Sirtori, A. L. Hutchinson, and A. Y. Cho, "Quantum cascade laser,"

Science **264**, 553 (1994).

[34] Y. Narukawa, Y. Kawakami, M. Funato, S. Fujita, S. Fujita, and S. Nakamura, "Role of self-formed InGaN quantum dots for exciton localization in the purple laser diode emitting at 420 nm," *Appl. Phys. Lett.* **70**, 981 (1997).

[35] M. Zhang, P. Bhattacharya, and W. Guo, "InGaN/GaN self-organized quantum dot green light emitting diodes with reduced efficiency droop," *Appl. Phys. Lett.* **97**, 011103 (2010).

[36] S. Tanaka, J.-S. Lee, P. Ramvall, and H. Okagawa, "A UV Light-Emitting Diode Incorporating GaN Quantum Dots," *Jpn. J. Appl. Phys.* **42**, 885 (2003).

[37] Z. Yuan, B. E. Kardynal, R. M. Stevenson, A. J. Shields, C. J. Lobo, K. Cooper, N. S. Beattie, D. A. Ritchie, and M. Pepper, "Electrically Driven Single-Photon Source," *Science* **295**, 102 (2001).

[38] B. Lounis and M. Orrit, "Single-photon sources," *Reports on Progress in Physics* **68**, 1129 (2005).

[39] P. Michler, A. Kiraz, C. Becher, W. V. Schoenfeld, P. M. Petroff, L. Zhang, E. Hu, and A. Imamoglu, "A Quantum Dot Single-Photon Turnstile Device," *Science* **290**, 2282 (2000).

[40] A. Muller, W. Fang, J. Lawall, and G. S. Solomon, "Creating Polarization-Entangled Photon Pairs from a Semiconductor Quantum Dot Using the Optical Stark Effect," *Phys. Rev. Lett.* **103**, 217402 (2009).

[41] A. Mohan, M. Felici, P. Gallo, B. Dwir, A. Rudra, J. Faist, and E. Kapon, "Polarization-entangled photons produced with high-symmetry site-controlled quantum dots," *Nature Photon.* **4**, 302 (2010).

[42] R. Hafenbrak, S. M. Ulrich, P. Michler, L. Wang, A. Rastelli, and O. G. Schmidt, "Triggered polarization-entangled photon pairs from a single quantum dot up to 30 K," *New J. Phys.* **9**, 315 (2007).

[43] M. Ghali, K. Ohtani, Y. Ohno, and H. Ohno, "Generation and control of polarization-entangled photons from GaAs island quantum dots by an electric field," *Nature Commun.* **3**, 1 (2012).

[44] G. Pfanner, M. Seliger, and U. Hohenester, "Entangled photon sources based on semiconductor quantum dots: The role of pure dephasing," *Phys. Rev. B* **78**, 195410 (2008).

[45] P. W. Shor and J. Preskill, "Simple proof of security of the BB84 quantum key distribution protocol," *Phys. Rev. Lett.* **85**, 441 (2000).

[46] N. Gisin, G. Ribordy, W. Tittel, and H. Zbinden, "Quantum cryptography," *Rev. Mod. phys.* **74**, 145 (2002).

[47] N. Gisin and R. Thew, "Quantum communication," *Nature Photon.* **1**, 165 (2007).

[48] A. Imamoglu, D. D. Awschalom, G. Burkard, D. P. Di-Vincenzo, D. Loss, M. Sherwin, and A. Samll, "Quantum information processing using quantum dot spins and cavity QED," *Phys. Rev. Lett.* **83**, 4204 (1999).

[49] D. Loss and D. P. DiVincenzo, "Quantum computation with quantum dots," *Phys. Rev. A* **57**, 120 (1998).

[50] R. J. Young, R. M. Stevenson, A. J. Shields, P. Atkinson, K. Cooper, D. A. Ritchie, K. M. Groom, A. I. Tartakovskii, and M. S. Skolnick, "Inversion of exciton level splitting in quantum dots," *Phys. Rev. B* **72**, 113305 (2005).

[51] M. Bayer, G. Ortner, O. Stern, A. Kuther, A. Gorbunov, A. Forchel, P. Hawrylak, S. Fafard, K. Hinzer, T. Reinecke, S. Walck, J. Reithmaier, F. Klopf, and F. Schäfer, "Fine structure of neutral and charged excitons in self-assembled In(Ga)As/(Al)GaAs quantum dots," *Phys. Rev. B* **65**, 195315 (2002).

[52] R. Thompson, R. Stevenson, A. Shields, I. Farrer, C. Lobo, D. Ritchie, M. Leadbeater, and M. Pepper, "Single-photon emission from exciton complexes in individual quantum dots," *Phys. Rev. B* **64**, 201302 (2001).

[53] R. J. Warburton, "Single spins in self-assembled quantum dots," *Nature Mater.* **12**, 483 (2013).

[54] A. J. Shields, "Semiconductor quantum light sources," *Nature Photon.* **1**, 215 (2007).

[55] M. Abbarchi, T. Kuroda, T. Mano, K. Sakoda, C. A. Mastrandrea, A. Vinattieri, M. Gurioli, and T. Tsuchiya, "Energy renormalization of exciton complexes in GaAs quantum dots," *Phys. Rev. B* **82**, 201301 (2010).

[56] R. Hafenbrak, S. M. Ulrich, P. Michler, L. Wang, A. Rastelli, and O. G. Schmidt, "Triggered polarization-entangled photon pairs from a single quantum dot up to 30 K," *New J. Phys.* **9**, 315 (2007).

[57] M. Gong, W. Zhang, G.-C. Guo, and L. He, "Exciton Polarization, Fine-Structure Splitting, and the Asymmetry of Quantum Dots under Uniaxial Stress," *Phys. Rev. Lett.* **106**, 227401 (2011).

[58] M. Abbarchi, C. A. Mastrandrea, T. Kuroda, T. Mano, K. Sakoda, N. Koguchi, S. Sanguinetti, A. Vinattieri, and M. Gurioli, "Exciton fine structure in strain-free GaAs/$Al_{0.3}Ga_{0.7}As$ quantum dots: Extrinsic effects," *Phys. Rev. B* **78**, 125321 (2008).

[59] R. Dingle, W. Wiegmann, and C. Henry, "Quantum States of Confined Carriers in Very Thin $Al_xGa_{1-x}As$-GaAs-$Al_xGa_{1-x}As$ Heterostructures," *Phys. Rev. Lett.* **33**, 827 (1974).

[60] O. I. Mićić, K. M. Jones, A. Cahill, and A. J. Nozik, "Optical, Electronic, and Structural Properties of Uncoupled and Close-Packed Arrays of InP Quantum Dots," *J. Phys. Chem. B* **102**, 9791 (1998).

[61] A. Scherer and H. G. Craighead, "Fabrication of small laterally patterned multiple quantum wells," *Appl. Phys. Lett.* **49**, 1284 (1986).

[62] Y. Sugiyama, Y. Sakuma, S. Muto, and N. Yokoyama, "Novel InGaAs/GaAs quantum dot structures formed in tetrahedral-shaped recesses on (111)B GaAs substrate using metalorganic vapor phase epitaxy," *Appl. Phys. Lett.* **67**, 256 (1995).

[63] H. Yagi, K. Muranushi, N. Nunoya, T. Sano, S. Tamura, and S. Arai, "Low-damage etched/regrown interface of strain-compensated $GaInAsP/InP$ quantum-wire laser fabricated by CH_4/H_2 dry etching and regrowth," *Appl. Phys. Lett.* **81**, 966 (2002).

[64] S. Birudavolu and N. Nuntawong, G. Balakrishnan, Y. C. Xin, S. Huang, S. C. Lee, S. R. J. Brueck, C. P. Hains, and D. L. Huffaker, "Selective area growth of InAs quantum dots formed on a patterned GaAs substrate," *Appl. Phys. Lett.* **85**, 2337 (2004).

[65] B. C. Lee, S. D. Lin, C. P. Lee, H. M. Lee, J. C. Wu, and K. W. Sun, "Selective growth of single InAs quantum dots using strain engineering," *Appl. Phys. Lett.* **80**, 326 (2002).

[66] H. Fourre, F. Diette, A. Cappy, "Selective wet etching of lattice-matched InGaAs/InAlAs on InP and metamorphic InGaAs/InAlAs on GaAs using succinic acid/hydrogen peroxide solution," *J. Vac. Sci. Technol. B* **14**, 3400 (1996).

[67] J. Tatebayashi, Y. Ota, S. Ishida, M. Nishioka, S. Iwamoto, and Y. Arakawa, "Site-controlled formation of InAs/GaAs quantum-dot-in-nanowires for single photon emitters," *Appl. Phys. Lett.* **100**, 263101 (2012).

[68] T. Kaizu, Y. Tamura, M. Igarashi, W. Hu, R. Tsukamoto, I. Yamashita, S. Samukawa, and Y. Okada, "Photoluminescence from GaAs nanodisks fabricated by using combination of neutral beam etching and atomic hydrogen-assisted molecular beam epitaxy regrowth," *Appl. Phys. Lett.* **101**, 113108 (2012).

[69] G. Juska, V. Dimastrodonato, L. O. Mereni, A. Gocalinska, and E. Pelucchi, "Towards quantum-dot arrays of entangled photon emitters," *Nature Photon.* **7**, 27 (2013).

[70] D. Leonard, M. Krishnamurthy, C. M. Reaves, S. P. Denbaars, and P. M. Petroff, "Direct formation of quantum-sized dots from uniform coherent islands of InGaAs on GaAs surfaces," *Appl. Phys. Lett.* **63**, 3203 (1993).

[71] Z. R. Wasilewski, S. Fafard, and J. P. McCaffrey, "Size and shape engineering of vertically stacked self-assembled quantum dots," *J. Cryst. Growth*. **201**, 1131 (1999).

[72] T. Mano, T. Noda, T. Kuroda, and S. Sanguinetti, "Self-assembled GaAs quantum dots coupled with GaAs wetting layer grown on GaAs (311) A by droplet epitaxy," *Phys. Status Solidi C* **8**, 257 (2011).

[73] M. Jo, T. Mano, and K. Sakoda, "Formation of highly anisotropic GaAs quantum dots on GaAs(001) substrates," *J. Phys.: Conf. Ser.* **245**, 012075 (2010).

[74] D. Guimard, S. Tsukamoto, M. Nishioka, and Y. Arakawa, "1.55 μm emission from InAs⁄GaAs quantum dots grown by metal organic chemical vapor deposition via antimony incorporation," *Appl. Phys. Lett.* **89**, 083116 (2006).

[75] M. Jo, T. Mano, Y. Sakuma, and K. Sakoda, "Extremely high-density GaAs quantum dots grown by droplet epitaxy," *Appl. Phys. Lett.* **100**, 212113 (2012).

[76] T. Walther, A. Cullis, D. Norris, and M. Hopkinson, "Nature of the Stranski-Krastanow Transition during Epitaxy of InGaAs on GaAs," *Phys. Rev. Lett.* **86**, 2381 (2001).

[77] F. Y. Chang, C. C. Wu, and H. H. Lin, "Effect of InGaAs capping layer on the properties of InAs/InGaAs quantum dots and lasers," *Appl. Phys. Lett.* **82**, 4477 (2003).

[78] L. Rebohle, F. F. Schrey, S. Hofer, G. Strasser, and K. Unterrainer, "Energy level engineering in InAs quantum dot nanostructures," *Appl. Phys. Lett.* **81**, 2079 (2002).

[79] Y. Nabetani, T. Ishikawa, S. Noda, and A. Sasaki, "Initial growth stage and optical properties of a three-dimensional InAs structure on GaAs," *J. Appl. Phys.* **76**, 347 (1994).

[80] H. Yamaguchi, M. R. Fahy, and B. A. Joyce, "Inhibitions of three dimensional island formation in InAs films grown on GaAs (111)A surface by molecular beam epitaxy," *Appl. Phys. Lett.* **69**, 776 (1996).

[81] Z. M. Wang, K. Holmes, J. L. Shultz, and G. J. Salamo, "Self-assembly of GaAs holed nanostructures by droplet epitaxy," *Phys. Stat. Sol. A* **202**, R85 (2005).

[82] K. Watanabe, N. Koguchi, and Y. Gotoh, "Fabrication of GaAs quantum dots by modified droplet epitaxy," *Jpn. J. Appl. Phys.* **39**, L79 (2000).

[83] S. Huang, Z. Niu, Z. Fang, H. Ni, Z. Gong, and J. Xia, "Complex quantum ring structures formed by droplet epitaxy," *Appl. Phys. Lett.* **89**, 031921 (2006).

[84]   T. Mano and N. Koguchi, "Nanometer-scale GaAs ring structure grown by droplet epitaxy," *J. Cryst. Growth.* **278**, 108 (2005).

[85]   M. Jo, T. Mano, and K. Sakoda, "Morphological control of GaAs quantum dots grown by droplet epitaxy using a thin AlGaAs capping layer," *J. Appl. Phys.* **108**, 083505 (2010).

[86]   C. Somaschini, S. Bietti, N. Koguchi, F. Montalenti, C. Frigeri, and S. Sanguinetti, "Self-assembled GaAs islands on Si by droplet epitaxy," *Appl. Phys. Lett.* **97**, 053101 (2010).

[87]   T. Mano, M. Abbarchi, T. Kuroda, C. A. Mastrandrea, A. Vinattieri, S. Sanguinetti, K. Sakoda, and M. Gurioli, "Ultra-narrow emission from single GaAs self-assembled quantum dots grown by droplet epitaxy," *Nanotechnology* **20**, 395601 (2009).

[88]   T. Mano, T. Kuroda, S. Sanguinetti, T. Ochiai, T. Tateno, J. Kim, T. Noda, M. Kawabe, K. Sakoda, G. Kido, and N. Koguchi, "Self-Assembly of Concentric Quantum Double Rings," *Nano Lett.* **5**, 425 (2005).

[89]   K. A. Sablon, J. H. Lee, Z. M. Wang, J. H. Shultz, and G. J. Salamo, "Configuration control of quantum dot molecules by droplet epitaxy," *Appl. Phys. Lett.* **92**, 203106 (2008).

[90]   T. Mano, T. Kuroda, S. Sanguinetti, T. Ochiai, T. Tateno, J. Kim, T. Noda, M. Kawabe, K. Sakoda, G. Kido, and N. Koguchi, "Self-Assembly of Concentric Quantum Double Rings," *Nano Lett.* **5**, 425 (2005).

[91]   L. Cavigli, M. Abbarchi, S. Bietti, C. Somaschini, S. Sanguinetti, N. Koguchi, A. Vinattieri, and M. Gurioli, "Individual GaAs quantum emitters grown on Ge substrates," *Appl. Phys. Lett.* **98**, 103104 (2011).

[92]   M. Jo, T. Mano, and K. Sakoda, "Morphological control of GaAs quantum dots grown by droplet epitaxyusing a thin AlGaAs capping layer," *J. Appl. Phys.* **108**, 083505 (2010).

[93]   T. Mano, M. Abbarchi, T. Kuroda, B. McSkimming, A. Ohtake, K. Mitsuishi, and K. Sakoda, "Self-Assembly of Symmetric GaAs Quantum Dots on (111)A Substrates: Suppression of Fine-Structure Splitting," *Appl. Phys. Express* **3**, 065203 (2010).

[94]   T. Kuroda, T. Mano, T. Ochiai, S. Sanguinetti, K. Sakoda, G. Kido, and N. Koguchi, "Optical transitions in quantum ring complexes," *Phys. Rev. B* **72**, 205301 (2005).

[95]   T. Miyazawa, K. Takemoto, Y. Sakuma, S. Hirose, T. Usuki, N. Yokoyama, M. Takatsu, and Y. Arakawa, "Single-Photon Generation in the 1.55-μm Optical-Fiber Band from an InAs/InP Quantum Dot," *Jpn. J. Appl. Phys.* **44**, L620 (2005).

[96]   N. I. Cade, H. Gotoh, H. Kamada, H. Nakano, S. Anantathanasarn, and R. Nötzel, "Optical characteristics of single InAs/InGaAsP/InP(100) quantum dots emitting at 1.55 μm," *Appl. Phys. Lett.* **89**, 181113 (2006).

[97]   K. Kawaguchi, M. Ekawa, A. Kuramata, T. Akiyama, H. Ebe, M. Sugawara, and Y. Arakawa, "Fabrication of InAs quantum dots on InP(100) by metalorganic vapor-phase epitaxy for 1.55 μm optical device applications," *Appl. Phys. Lett.* **85**, 4331 (2004).

[98]   C. Paranthoen, N. Bertru, O. Dehaese, A. Le Corre, S. Loualiche, B. Lambert, and G. Patriarche, "Height dispersion control of InAs/InP quantum dots emitting at 1.55 μm," *Appl. Phys. Lett.* **78**, 1751 (2001).

[99]   S. Fafard, Z. Wasilewski, J. McCaffrey, S. Raymond, and S. Charbonneau, "InAs self-assembled

quantum dots on InP by molecular beam epitaxy," *Appl. Phys. Lett.* **68**, 991 (1996).

[100] G. Balakrishnan, S. Huang, T. J. Rotter, A. Stintz, L. R. Dawson, K. J. Malloy, H. Xu, and D. L. Huffaker, "2.0 μm wavelength InAs quantum dashes grown on a GaAs substrate using a metamorphic buffer layer," *Appl. Phys. Lett.* **84**, 2058 (2004).

[101] N. N. Ledentsov, V. A. Shchukin, T. Kettler, K. Posilovic, D. Bimberg, L. Y. Karachinsky, A. Y. Gladyshev, M. V. Maximov, I. I. Novikov, Y. M. Shernyakov, A. E. Zhukov, V. M. Ustinov, and A. R. Kovsh, "MBE-grown metamorphic lasers for applications at telecom wavelengths," *J. Cryst. Growth.* **301**, 914 (2007).

[102] P. W. Fry, I. E. Itskevich, D. J. Mowbray, M. S. Skolnick, J. J. Finley, J. A. Barker, E. P. O'Reilly, L. R. Wilson, I. A. Larkin, P. A. Maksym, M. Al-Khafaji. J. P. R. David, A. G. Cullis, G. Hill, and J. C. Clark, "Inverted electron-hole alignment in InAs-GaAs self-assembled quantum dots," *Phys. Rev. Lett.* **84**, 733 (2000).

[103] G. S. Pearson and D. A. Faux, "Analytical solutions for strain in pyramidal quantum dots," *J. Appl. Phys.* **88**, 730 (2000).

[104] G. W. Orr, L. J. Barbour, and J. L. Atwood, "Controlling Molecular Self-Organization: Formation of Nanometer-Scale Spheres and Tubules," *Science* **285**, 1049 (1999).

[105] W. Sheng and J.-P. Leburton, "Anomalous Quantum-Confined Stark Effects in Stacked InAs/GaAs Self-Assembled Quantum Dots," *Phys. Rev. Lett.* **88**, 167401 (2002).

[106] Y.-H. Kuo, Y. K. Lee, Y. Ge, S. Ren, J. E. Roth, T. I. Kamins, D. A. B. Miller, and J. S. Harris, "Strong quantum-confined Stark effect in germanium quantum-well structures on silicon," *Nature* **437**, 1334 (2005).

[107] Ying-Lin Chou and Shun-Jen Cheng, private communication.

[108] G. Gélinas, A. Lanacer, R. Leonelli, R. A. Masut, and P. J. Poole, "Carrier thermal escape in families of InAs/InP self-assembled quantum dots," *Phys. Rev. B* **81**, 235426 (2010).

[109] D. A. Woolf, D. I. Westwood, and R. H. Williams, "Surface reconstructions of GaAs(111)A and (111)B: A static surface phase study by reflection high-energy electron diffraction," *Appl. Phys. Lett.* **62**, 1370 (1993).

[110] M. R. Fahy, K. Sato, and B. A. Joyce, "Reflection high-energy electron diffraction intensity oscillations during the growth by molecular beam epitaxy of GaAs (111)A," *Appl. Phys. Lett.* **64**, 190 (1994).

[111] N. N. Ledentsov, V. M. Ustinov, V. A. Shchukin, P. S. Kop'ev, Z. I. Alferov, and D. Bimberg, "Quantum dot heterostructures: Fabrication, properties, lasers (Review)," *Semiconductors* **32**, 343 (1998).

[112] M. H. Meynadier, J. L. de Miguel, M. C. Tamargo, and R. E. Nahory, "Optical investigations of the band structure of strained InAs/AlInAs quantum wells," *Appl. Phys. Lett.* **52**, 302 (1988).

[113] M. S. Hybertsen, "Band offset transitivity at the InGaAs/InAlAs/InP(001) heterointerfaces," *Appl. Phys. Lett.* **58**, 1759 (1991).

[114] N. A. Jahan, C. Hermannstädter, J. H. Huh, H. Sasakura, T. J. Rotter, P. Ahirwar, G. Balakrishnan, K. Akahane, M. SaSaki, H. Kumano, and I. Suemune, "Temperature dependent carrier dynamics in telecommunication band InAs quantum dots and dashes grown on InP substrates," *J. Appl. Phys.* **113**,

033506 (2013).

[115] S. Cortez, O. Krebs, S. Laurent, M. Senes, X. Marie, P. Voisin, R. Ferreira, G. Bastard, J.-M. Gérard, and T. Amand, "Optically Driven Spin Memory in n-Doped InAs-GaAs Quantum Dots," *Phys. Rev. Lett.* **89**, 207401 (2002).

[116] E. Le Ru, J. Fack, and R. Murray, "Temperature and excitation density dependence of the photoluminescence from annealed InAs/GaAs quantum dots," *Phys. Rev. B* **67**, 245318 (2003).

[117] A. S. Bracker, E. A. Stanaff, D. Gammon, M. E. Ware, J. G. Tischler, and D. Park, "Binding energies of positive and negative trions: From quantum wells to quantum dots," *Phys. Rev. B* **72**, 035332 (2005).

[118] Yo-Nian Wu and Shun-Jen Cheng, private communication.

[119] V. Mlinar and A. Zunger, "Effect of atomic-scale randomness on the optical polarization of semiconductor quantum dots," *Phys. Rev. B* **79**, 115416 (2009).

[120] N. Chauvin, B. Salem, G. Bremond, G. Guillot, C. Bru-Chevallier, and M. Gendry, "Size and shape effects on excitons and biexcitons in single InAs/InP quantum dots," *J. Appl. Phys.* **100**, 073702 (2006).

[121] N. Kamaraju, S. Kumar, and A. K. Sood, "Large nonlinear absorption and refraction coefficients of carbon nanotubes estimated from femtosecond z-scan measurements," *Appl. Phys. Lett.* **91**, 251103 (2007).

[122] A. Ohtake, M. Ozeki, and J. Nakamura, "Strain relaxation in InAs/GaAs (111) A heteroepitaxy," *Phys. Rev. Lett.* **84**, 4665 (2000).

Acknowledgement